E.A.Gorbachev, E.S.Kozlyakova, L.A.Trusov, A.E.Sleptsova, M.A.Zykin, P.E.Kazin
Russ. Chem. Rev., 2021, **90** (10) 1287 – 1329

https://doi.org/10.1070/RCR4989

Design of modern magnetic materials with giant coercivity

Evgeny A. Gorbachev,[a] Ekaterina S. Kozlyakova,[a] Lev A. Trusov,[a*] Anastasia E. Sleptsova,[a] Mikhail A. Zykin,[b] Pavel E. Kazin [a*]

[a] Department of Chemistry, Lomonosov Moscow State University, Leninskie Gory, stroenie 3, 119991 Moscow, Russian Federation,
[b] Kurnakov Institute of General and Inorganic Chemistry, Russian Academy of Sciences, Leninsky prosp., 119991 Moscow, Russian Federation

The review is devoted to compounds and materials demonstrating extremely high magnetic hardness. The recent advances in the synthesis of modern materials for permanent magnets are considered, and a range of exotic compounds interesting for fundamental research is described. The key details of chemical composition, crystal structure and magnetic microstructure responsible for the appearance of high magnetic anisotropy and giant coercivity are analyzed. The challenges of developing the title materials are noted and strategies for their solution are discussed.
The bibliography includes 389 references.

Contents

1. Introduction 1287
2. Brief theoretical introduction to the magnetism of materials 1288
3. Materials based on rare earth elements 1292
   3.1. Magnetic materials based on Nd – Fe – B phases 1292
   3.2. Magnetic materials based on Sm – Co phases 1296
   3.3. Magnetic materials based on Sm – Fe – N phases 1298
   3.4. Problems and prospects 1300
4. Ordered alloys with tetragonal $L1_0$ structure 1301
5. High-coercivity alloys based on manganese 1304
6. Hard magnetic ferrites 1305
   6.1. Lutetium ferrite 1306
   6.2. Cobalt ferrite 1307
   6.3. ε-Iron oxide 1309
   6.4. Substituted M-type hexaferrites 1312
7. Other non-metal compounds 1316
8. Low-dimensional magnets 1316
   8.1. Single-ion and single-molecule magnets 1317
   8.2. Single-chain magnets 1319
   8.3. Layered magnets 1321
9. Conclusion 1322
10. List of acronyms and designations 1322

1. Introduction

Among diverse materials that actively interact with the magnetic field, an important place is occupied by materials for permanent magnets, which are able to generate their own magnetic field. Permanent magnets have been known to people since ancient times. For example, owing to the natural magnetization of iron ore, people invented compass orientation, which was the first technology using magnetism. However, magnets became really prevalent in everyday life and in industry only in the 20th century. Their uses range from the manufacture of souvenir magnets, magnetic locks, information storage devices, loudspeakers and electric motors and generators to magnetic resonance imaging devices, magnetically levitated trains and elementary particle accelerators.[1–3]

A fundamental feature of compounds and materials that can be used to manufacture permanent magnets is magnetic anisotropy: the presence of special axes along which the magnetization vector of the material is spontaneously aligned. The greater the material anisotropy, the more efficient the resistance of magnets against magnetization reversal under the action of external magnetic fields, *i.e.*, they have high coercivity. If magnetization of a material can be reversed in a field exceeding 40 kA m^{-1} (500 Oe), which is ~1000 times higher than the Earth's magnetic field, this is a hard magnetic (or magnetically hard) material. The first magnets, manufactured from high-carbon steel, could be magnetically reversed in ~8 kA m^{-1} (100 Oe) fields. In the 1930s–1940s, hard magnetic behaviour was found for iron alloys with aluminium, nickel, cobalt and copper.† The alloys had a coercivity of 30 – 160 kA m^{-1} (0.4 – 2.0 kOe) and were characterized by high Curie temperatures and high remanent magnetization. Hard magnetic ferrites (hexaferrites) $MFe_{12}O_{19}$ (M = Pb, Ba, Sr) discovered in the 1950s had a ~3 times lower saturation magnetization than alnico alloys. However, ferrites can be used to manufacture ceramic magnets with a coercivity of up to 320 kA m^{-1} (4 kOe). In addition, ferrites are rather cheap and withstand harsh media and elevated temperatures; therefore, they were the most popular materials for the manufacture of permanent magnets for several decades.[1,3–5] The development of hard magnetic Sm – Co and Nd – Fe – B alloys, containing rare earth elements, in the 1970s – 1990s revolutionized the production of materials for permanent magnets. These alloys have an extremely high magnetic anisotropy, very high magnetization and coercivity ranging from 800 to 2400 kA m^{-1} (10 – 30 kOe); hence, they possess record-high values for the maximum magnetic energy product, which determines the performance of a

† The international name of these alloys, alnico, is the acronym of chemical elements Al, Ni, Co that form the alloy.

Received 4 August 2020
© 2021 Uspekhi Khimii, ZIOC RAS, Russian Academy of Sciences and IOP Publishing Limited

permanent magnet, that is, the magnetic flux generated by a magnet for the conversion of magnetic energy to other kinds of energy. However, the application of rare and expensive elements substantially retards the growth of production of hard magnetic alloys, which has currently resulted in a shortage of high-energy permanent magnets. This brings about a challenge of developing hard magnetic materials containing no rare earth elements.[6–9]

A real breakthrough in the understanding of the magnetism of materials with extremely high magnetic hardness took place in the last 20 years. When efficient methods for the synthesis of these materials appeared, it became possible to considerably improve the properties of almost all known classes of such materials. Furthermore, several new promising hard magnetic compounds were found. In this regard, coercivities above 1600 kA m^{-1} (20 kOe) are more and more often called giant coercivity in scientific literature. The modern market of permanent magnets is dominated by neodymium and ferrite magnets; however, a wide selection of other hard magnetic materials with diverse properties for special and niche applications is available to scientists and engineers.

Today, there are virtually no scientific publications describing the variety of magnetic materials characterized by giant coercivity ranging from intermetallics and ferrites to low-dimensional magnets. We made an attempt to fill this gap by integrating the current views on the magnetic properties of these materials and depicting the strategies towards their production. The review does not consider other properties of the title materials (mechanical, electrical, magneto-optical, magnetocaloric, and so on) that are important for particular applications.

E.A.Gorbachev. PhD Student of the Department of Materials Science, Moscow State University.
E-mail: ev.a.gorbachev@gmail.com
Current research interests: solid state chemistry, synthesis and functional properties of oxide magnetic materials.
E.S.Kozlyakova. PhD in Physics and Mathematics, Researcher at the Department of Physics, Moscow State University.
E-mail: evenuel1@gmail.com
Current research interests: physics of condensed matter, magnetic properties of inorganic compounds and materials, superconductivity, low-dimensional magnetism.
L.A.Trusov. PhD in Chemistry, Junior Researcher at the Department of Chemistry, Moscow State University.
E-mail: trusov@inorg.chem.msu.ru
Current research interests: inorganic chemistry, solid state chemistry, magnetic materials, nanomaterials, magnetic fluids
A.E.Sleptsova. PhD Student at the Department of Materials Science, Moscow State University.
E-mail: sleptsovaanastasia@gmail.com
Current research interests: solid state chemistry, synthesis and functional properties of oxide magnetic materials.
M.A.Zykin. PhD in Chemistry, Researcher at the IGIC RAS.
E-mail: mzykin@gmail.com
Current research interests: solid state chemistry, synthesis and magnetic properties of inorganic single-ion magnets.
P.E.Kazin. Doctor of Sciences, Professor at the Department of Chemistry, Moscow State University.
E-mail: kazin@inorg.chem.msu.ru
Current research interests: solid state chemistry, inorganic chemistry, synthesis and functional properties of oxide inorganic compounds and materials.

Translation: Z.P.Svitanko

2. Brief theoretical introduction to the magnetism of materials ‡

The key characteristic of hard magnetic materials is the magnetic hysteresis loop, which reflects the dependence of magnetization or magnetic induction (B) of a ferromagnet (M) on the external magnetic field strength (H). The hysteresis loop parameters that reflect the main magnetic properties of a material are as follows (Fig. 1):

— intrinsic coercivity (H_c) is the magnetic field strength at which the sample magnetization becomes zero after magnetization to saturation followed by application of a magnetic field with the opposite sign;

— saturation magnetization (M_s) is the sample magnetization at which the dependence $M(H)$ reaches a plateau;

— remanent magnetization (M_r) is the intrinsic magnetization of a substance without an external magnetic field after magnetization to saturation.

If the hysteresis loop is plotted in the $B(H)$ coordinates, the above values are replaced by their analogues: H_c^B is the induction coercivity, B_r is the residual induction. While discussing the properties of materials in this review, we use the intrinsic coercivity.

The key characteristics of the performance of a permanent magnet is the maximum energy product $(BH)_{max}$, which indicates the maximum energy that can be stored by a magnet, or the work that can be performed by a magnet while moving in a magnetic field. The maximum energy product $(BH)_{max}$. is calculated as the maximum absolute magnitude of the product of magnetic induction by the magnetic field strength that belong to the second quadrant of the hysteresis loop (see Fig. 1 *b*). For attaining the high value of $(BH)_{max}$, both the coercivity and remanent magnetization of a magnet must be high.[10]

At the atomic level, the primary role is played by the magnetic moment generated by an atom or an ion. The magnetic moment of an ion is determined by the number of unpaired electrons in its inner shells (spin magnetic moment, S), orbital movement of electrons (orbital magnetic moment, L) and their mutual influence (spin–orbit coupling). Nuclei of many elements also possess magnetic moments, which are, however, three orders of magnitude lower than the electron magnetic moments. Therefore, in the calculation of the total magnetic moment of an ion, the nuclear contribution is usually neglected, as it affects only

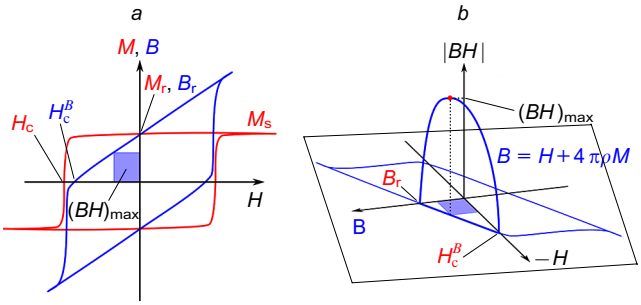


Figure 1. Magnetic hysteresis loop and its main characteristics (*a*) and illustration to the calculation of the maximum energy product (*b*).[10] H_c is the intrinsic coercivity, ρ is the density of the material; for other designations, see the text.

‡ The values in this review are given in S.I. and C.G.S. (in parentheses) units.

the hyperfine structure of the energy levels of the atom. High effective magnetic moments (μ_{eff}) in the solid state are inherent in open (unfilled) shell ions, including ions of 3d elements: Fe^{3+} (5.8 μ_B), Fe^{2+} (5.4 μ_B), Mn^{3+} (4.8 μ_B), Cr^{2+} (4.9 μ_B), Co^{2+} (4.9 μ_B), Cr^{3+} (3.8 μ_B) and V^{2+} (3.8 μ_B) and ions of 4f elements: Dy^{3+} (10.5 μ_B), Ho^{3+} (10.5 μ_B), Tb^{3+} (9.7 μ_B), Er^{3+} (9.5 μ_B), Gd^{3+} (7.9 μ_B) and Eu^{2+} (7.9 μ_B).[11] Usually, exactly these elements are used to attain high magnetization. Most often, ions of 4d- and 5d-elements have low or zero effective magnetic moments due to the formation of a low-spin state, and they are rarely considered for this purpose.

Apart from the spin–orbit coupling, the final magnetic moment of the material is considerably affected by the crystal field — the electric field generated by neighbouring ions in the crystal lattice. Depending on the chemical composition and the geometric positions of the neighbouring ions, some electronic states of the magnetic centre are energetically more favourable than other ones, mainly due to the electrostatic repulsion effects. This leads to splitting of the primary energy structure of the electron levels and to occupancy redistribution. The crystal field effect is most pronounced in 3d elements; therefore, the experimentally determined magnetic moments mentioned above often do not contain an orbital contribution. For example, the calculation with allowance for the orbital contribution for Mn^{3+} ($S = 2$, $L = 2$) gives the total moment $J = 0$, while many Mn^{3+} compounds have $\mu_{eff} \approx 4.8$ μ_B. The crystal lattice has a much weaker effect on 4f elements, since the f shell is much better shielded from the external action.[12] The situation for 4d and 5d elements is more complicated, since the crystal field and spin–orbit coupling effects for them are comparable.

The coercivity is largely determined by the magnetic anisotropy, that is, the dependence of the ground state energy of the magnetic subsystem on the direction of magnetization. The magnetic anisotropy is quantitatively measured using values such as magnetic induction $B_a = (2\mu_0 E_a)^{1/2}$ or field strength H_a, although the main value is the anisotropy energy E_a defined as the difference between the system energies in the case of magnetization along the easy axis (axes or plane) and along the hardest axis of magnetization.

The magnetic anisotropy with respect to the structural axes of the crystal is called the magnetocrystalline anisotropy. The final value of E_a can be considerably affected by the shape anisotropy, mechanical stress and magnetostriction effects and dipole–dipole and exchange anisotropy in composites; however, for most of materials, the theoretical limit of coercivity is determined by the magnetocrystalline anisotropy. Therefore, many authors, use H_a to imply particularly the magnetocrystalline anisotropy field. One more designation for this type of anisotropy is the set of constants K_1, K_2, *etc.*, measured in the units of energy and representing terms of a series expansion of the energy E_a in the powers of the direction cosines of the spontaneous magnetization vector in relation to the crystallographic axes. The magnetocrystalline anisotropy of most known materials is in the range from 10^2 to 10^7 J m^{-3} ($10^3 - 10^8$ erg cm^{-3}).

The main causes for the presence of magnetocrystalline anisotropy are the spin–orbit coupling in combination with low crystal field symmetry on a magnetic ion (single-ion anisotropy), exchange anisotropy, dipole–dipole interaction between magnetic centres and some other factors. This issue is addressed in more detail in textbooks,[11, 13, 14] books [15, 16] and reviews.[8, 17] Although this subject is seemingly thoroughly elaborated, the causes behind the appearance of magnetocrystalline anisotropy in a particular material are far from being always clear. Both magnetic and magnetocrystalline anisotropy are considered in the relevant parts of the review devoted to particular magnetic materials.

In most ferromagnetic materials, coercivity is lower by a large factor than the magnetic anisotropy field and the remanent magnetization is much lower than the saturation magnetization. Among other factors, this is caused by the decrease in the magnetostatic energy as a result of crystal splitting into regions which are magnetized uniformly, but in different directions, and, therefore, they counterbalance one another. These regions form magnetic domains.[18–20] There should be a site between the domains where the magnetization vector gradually rotates (it is called the domain wall). In a ferromagnet, the rotation is hampered by exchange interaction, which tends to align all magnetic moments along the same direction. Other factors that hamper the rotation of the magnetization vector are magnetocrystalline anisotropy, magnetoelastic processes and an external magnetic field, due to which the nucleation of domain walls results in energy increase.[21] As a result, in real systems, the domain pattern can have a fairly complicated shape and considerably depends on external conditions, chemical composition, microstructure, the presence of impurities or structural defects, and even on the local shape and temperature of the magnet.[22]

The possibility of spontaneous formation of domains reduces both the really attainable coercivity and the remanent magnetization of the material. In an external magnetic field, more favourable domains are those the magnetization of which coincides with the field; therefore, domain walls may begin to move, rearrange, and even be 'squeezed out' of the magnet. However, as soon as the field decreases, domains appear once again. This mechanism is most characteristic of soft magnetic materials with low magnetic anisotropy, since in a material possessing relatively high magnetocrystalline anisotropy, the restoration of the primary domain structure is hampered. Furthermore, the motion of domain walls can be suppressed if the walls are fixed by means of magnetoelastic energy, particularly, by introducing admixtures or structure defects into the material (pinning of domain walls).[23] Mechanical stresses that arise at such defects generate energy barriers for domain wall motion. The domain walls that arise once again after magnetization cannot overcome some of the barriers any longer; as a result, magnetization reversal requires much stronger magnetic field; simultaneously the remanent magnetization and coercivity increase.[24]

In order to further increase the coercivity, it is possible to take a material that consists of separate single-domain particles aligned along the easy axis of magnetization and along the magnetic field. In this case, during magnetization reversal, the field has to overcome not the domain walls, but directly the magnetic anisotropy, which may have high energy. The behaviour of single-domain particles with the only axis of easy magnetization in a magnetic field is described by the Stoner–Wohlfarth model [25]

$$E = V[K\sin^2(\theta - \varphi) - \mu_0 H_{ext} M_s \cos\varphi] \quad (1)$$

where V is the volume of the particle, K is the magnetic anisotropy constant, θ is the angle between the directions of the field and the easy axis of magnetization, φ is the angle between the directions of particle magnetization and the external field, $\mu_0 = 1.257 \times 10^{-6}$ H A^{-2} is the magnetic constant, H_{ext} is the external magnetic field.

According to the Stoner–Wohlfarth model, the anisotropy field of a single-domain particle is given by

$$H_a = \frac{2K}{\mu_0 M_s} \quad (2)$$

and this value is often used as the theoretical limit for the material coercivity. Typical hysteresis loops for a single-domain particles according to this model are presented in Fig. 2 *a*. However, real experimental data are rarely adequately described by this model, since it takes into account only some types of magnetic anisotropy (for example, uniaxial) and does not take into account factors such as the effect of temperature and interaction between particles and non-uniformity of magnetization on defects or on the particle surface.

There are various extensions to the Stoner–Wohlfarth model (see, for example, Ref. 26) and theoretical studies that model misorientation of particles,[27,28] exchange or dipole[29] interactions between them, exchange anisotropy of particles,[30] temperature effect,[31] size effects [including the superparamagnetic limit d_{sp} (see Ref. 2 *b*) and blocking temperature] and studies describing the behaviour of an ensemble of interacting or separate nanoparticles taking into account surface defects[32] or an admixture layer.[33–35] When the particle size is smaller than the superparamagnetic limit and the temperature is relatively high (above the blocking temperature), the energy of thermal vibrations becomes higher than the energy of magnetic anisotropy, and, therefore, these particles have a zero coercivity.[36,37] These models are considered in more detail in a review of Zhao *et al.*[38]

One of the main causes for the fact that the coercivity corresponding to the Stoner–Wohlfarth model is never achieved in practice is underestimation of the role of surface defects and the so-called self-pinning effect on the surface defects.[39] It is noteworthy that the defects and impurities of the matrix in which single-domain particles are embedded may lead to both a decrease[35] and an increase in the coercivity.[24,33] If the defects and admixtures are exchange-coupled to the insulating medium and to the rest of the material and exhibit a strong magnetic anisotropy, then in some cases, they can markedly increase the coercivity[33] or magnetization[40] of the final material. This can be utilized to construct high-coercivity materials, for example, by doping different faces of particles with various elements, *i.e.*, by generating artificial particle–surface exchange anisotropy or by counterbalancing the existing anisotropy if it has an adverse effect on H_c. The exchange coupling between the particles of the main phase and the strong particle misorientation are undesirable; the effect of these factors on H_c is much more pronounced than magnetostatic effects.[28]

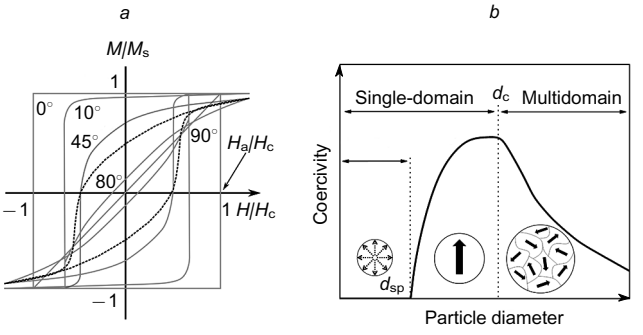


Figure 2. Hysteresis loops of single-domain particles predicted by the Stoner–Wohlfarth model for various angles between the field and easy magnetization axis (continuous lines) and for an assembly of disoriented particles (dashed line) (*a*), and dependences of the coercivity and magnetic microstructure on the particle diameter (*b*). d_c is the single-domain limit.

While summarizing the results of the above studies, one can draw the following conclusion: giant coercivity can be attained by fabricating a material from oriented single-domain particles with coinciding easy axes of magnetization.[41] In this case, the particle surface or the admixed phase separating the particles should block the exchange and dipole interaction, prevent particles from growing together to give multidomain structures, and enhance, to the extent possible, the magnetization and coercivity *via* an additional contribution to the anisotropy or exchange processes. Uniaxial anisotropy is preferred for single-domain particles of the main phase, because in the case of easy plane anisotropy or in the presence of several easy axes of magnetization, there are much more options for the change in the direction of magnetization, with magnetization reversal occuring in several stages.

The magnetization reversal and, consequently, the hysteresis of a permanent magnet are determined by nucleation and motion of domain walls and by either coherent or incoherent rotation of the magnetization vector of a separate domain. The final coercivity is dictated by the most efficient of these processes. Unfortunately, the complexity and diversity of magnetization reversal mechanisms and the microstructural factors affecting them in real systems often preclude development of a model that would take into account all of them; therefore, existing models reflect only some special cases. For example, the following expression is often used to calculate the coercivity of single-domain particles with allowance for microstructural parameters:[16]

$$\mu_0 H_c = \frac{2K_1}{M_s}\alpha - N_{eff} M_s \quad (3)$$

In this equation, $2K_1/\mu_0 M_s$ corresponds to the coercivity of a single-domain particle according to the Stoner–Wohlfarth model; the coefficient $\alpha \leqslant 1$ mainly describes decrease in the energy necessary for domain wall nucleation due to lattice defects or disorder on grain surfaces; N_{eff} reflects the effective demagnetization factor due to internal magnetic fields at the grain edges and corners. In some cases, the predominant mechanism of magnetization reversal in a particular material can be identified by comparing the results of calculations and experimental estimation of α and N_{eff}.

The demagnetizing field, which is generated due to magnetostatic processes, is an important characteristic determining the magnetic properties for both a separate single-domain particle and the whole magnet. It not only gives rise to magnetic domains, but also accounts for decreasing coercivity in single-domain particles depending on the shape of the magnet (or particles that constitute the magnet) and can make a contribution to the magnetic

anisotropy, thus giving rise to so-called shape anisotropy. If the shape is not spherical, the demagnetizing field is not identical in any direction, *i.e.*, it has one or several local energy minima — additional easy magnetization axes. Indeed, in the case of thin films in a zero external magnetic field, owing to the magnetostatic energy difference

$$\Delta E = \frac{1}{2}\mu_0 M^2 \cos^2\Theta \quad (4)$$

(Θ is the angle between the normal to the film surface and direction of magnetization M), the position of the magnetic moment in the film plane becomes energetically favourable. In the general form, the demagnetizing field (H_d) is found from the following expression:

$$H_d(r) = \int \frac{(r - r')\nabla M(r')dr'}{|r - r'|^3} \quad (5)$$

where r and r' are the radius vectors of the two points between which the quantity is calculated. However, it is rarely possible to obtain an analytical expression for H_d in a real magnet (particle) of a complex shape. The mathematics and physics of magnetostatic fields are quite complicated, and analytical solutions are known only for a few special geometries. Extrapolation to more complex cases brings about additional approximations.[42] Most of the proposed procedures take H_d as the demagnetization factor N, which shows how much the field inside the sample differs from the applied magnetic field H_a

$$H_{eff} = H_a - N\langle M\rangle \quad (6)$$

where $\langle M\rangle$ is the averaged sample magnetization.[43] For some sample shapes, it was possible to determine N and to get the real hysteresis loop. However, in most cases, it is difficult to make such corrections.

The lowest demagnetizing field and a strong shape anisotropy, which lead to the maximum energy product $(BH)_{max}$, correspond to thin particles or magnets extended along the magnetic field[44] or to more exotic shapes (*e.g.*, horseshoe shape).[45] In some magnets, the shape anisotropy is the predominant mechanism for coercivity. For example, in alnico magnets consisting of oblong ferromagnetic FeCo particles in weakly magnetic AlNi matrix, the greatest contribution to the coercivity is made by shape anisotropy.[16] However, this factor operates best of all in the case of soft magnetic materials (particularly, for cobalt and alnico, $L1_0$-FeNi and α''-$Fe_{16}N_2$) with a medium coercivity; this makes it possible to obtain $(BH)_{max}$ of not more than 10% of the theoretical limit. Meanwhile, a benefit of magnetically hard materials is exactly that they can be used to fabricate high-coercivity magnets of almost any shape, since the demagnetization factor in them is opposed by a colossal magnetocrystalline anisotropy.[8] In addition, oblong-shaped hard magnetic particles often prove to be multidomain, which cancels all benefits of low demagnetization factor. Therefore, maintenance of the single-domain character of hard magnetic particles is a stricter criterion for obtaining a high-energy magnet than the particle shape.

One more approach suitable for producing a high energy product, while sacrificing the coercivity, is to fabricate two-phase nanocomposites in which a soft magnetic phase with high magnetization is exchange-coupled to a hard magnetic phase with high coercivity. However, two conditions are to be observed:

— hard magnetic phase must be oriented;

— the particle size of the soft magnetic phase must be sufficiently small (comparable with the size of the domain wall of the hard magnetic phase; as a rule, no more than 10 nm) to ensure complete 'fixing' of the magnetic moments in them due to the effect of the strong magnetocrystalline anisotropy of the hard magnetic phase.

The magnetization and magnetic anisotropy values of such magnets are intermediate between these characteristics of both phases, which provides for the manufacture of magnets with unique energy products. In addition, parameters of these magnets can be additionally modified by using shape anisotropy, for example, by fabricating rod-like soft magnetic particles in a hard magnetic matrix.[8]

Thus, from the theoretical standpoint, the following conditions must be met to attain the highest possible coercivity or energy product of a magnet:

— the chemical compound forming the magnet must possess high uniaxial magnetocrystalline anisotropy (condition for H_c) and high magnetization [additional condition for $(BH)_{max}$];

— single-domain particles in which the energy of the magnetic anisotropy is higher than the thermal energy by a large factor (to prevent the particle transition to the superparamagnetic state) must be the major structural unit of the magnet; if such particles cannot be obtained, efficient pinning of domain walls in multidomain grains is required;

— single-domain particles must be textured, *i.e.*, they must be aligned in such a way that their easy magnetization axes must coincide with the direction of the external field;

— particles must be packed as closely as possible (in the absence of macroscopic soft magnetic, para- and diamagnetic impurities);

— the particles must be separated by partitions (which should be as thin as possible), which prevent the exchange coupling of particles or act as efficient centres of pinning suppressing the domain wall motion;

— the particle surface and the separating phase must have an intrinsic anisotropy, which increases the coercivity;

— in order to attain a higher magnetization, impurities, if present, must be soft magnetic, while the particle size of the intergrain phases must be comparable with the thickness of domain walls of the hard magnetic phase — these are so-called exchange-coupled composites (in an ideal case, the impurity particles correspond to the minimum demagnetization factor and represent, for example, nanorods); however, it must be borne in mind that this results in decreasing coercivity, although $(BH)_{max}$ may increase;

— the shape of single-domain particles must correspond to the lowest demagnetization factor (this may be, for example, a thin rod with magnetization in the longitudinal direction); however, it is much more important to observe the single-domain character of grains than the particle shape;

— the shape of the ready magnet must correspond to the minimum demagnetization factor, *i.e.*, a magnet is to be shaped like a rod or to have an unusual shape (for example, a horseshoe); this condition applies to soft magnetic materials.

Depending on the application area, a magnet must satisfy other requirements. For electric vehicle engines, it is necessary that the magnet should retain its properties at temperatures of 160–200 °C. For aerospace applications in

power generators, bearings and engines, stability at least at 500–600 °C is required; therefore, for these applications, the material forming the magnet should have a high Curie temperature. In addition, the magnet material should be chemically and thermally stable over a broad range of temperatures and in different media, should have high strength, toughness or plasticity; this material should also be composed of widely occurring chemical elements and methods for the synthesis and fabrication of this material should be relatively simple for scaling-up for industrial production.

3. Materials based on rare earth elements

Compounds of rare earth elements § show the highest values of the anisotropy field. However, this does not mean that a magnet made of these compounds would have record-high magnetic characteristics. The development of synthetic approaches made it possible to bring the properties of some magnets based on rare earth elements to the theoretically limiting values.

3.1. Magnetic materials based on Nd–Fe–B phases

Permanent magnets based on alloys of the Nd–Fe–B system have the highest energy products among all known materials. In the industrial magnets with the optimal composition based on the $Nd_2Fe_{14}B$ hard magnetic phase, $(BH)_{max}$ reaches ~ 400 kJ m^{-3} (~ 50 MG Oe), which is close to the theoretical limit $\mu_0 M_r^2/4 = 516$ kJ m^{-3} (64.8 MG Oe),[46] calculated with the assumption of 100% volume fraction of the $Nd_2Fe_{14}B$ phase with the highest magnetization. The saturation induction can reach almost 1.6 T (16 kOe), the saturation magnetization is 168 A m^2 kg^{-1} (168 emu g^{-1}), with the remanent magnetization being, in some cases, higher than 97% of the saturation, which is responsible for the high energy product. Despite the high anisotropy field $H_a \approx 5888–6605$ kA m^{-1} ($\sim 74–83$ kOe)[32,47] of the main $Nd_2Fe_{14}B$ hard magnetic phase, the coercivity varies from 63 7 kA m^{-1} (8 kOe) to 1592 kA m^{-1} (20 kOe) and is, on average, 955 kA m^{-1} (12 kOe).[16] By various modifications, the coercivity can be brought to 2865 kA m^{-1} (36 kOe). The $(BH)_{max}$ value also can be higher than 400 kJ m^{-3} (50 MG Oe), but in this case, the coercivity does not exceed 955 kA m^{-1} (12 kOe).[47,48] The main drawback of neodymium magnets is still their low Curie temperature ($T_C = 310–315$ °C), resulting in a sharp decrease in the coercivity already at 150 °C. The T_C value can be increased by replacing neodymium by other elements. In some cases, this modification may, at the same time, increase the coercivity or magnetization.

In the magnets based on lanthanide alloys with 3d metals, that is, Nd–Fe–B, Sm–Co and Sm–Fe–N systems (see below), the most pronounced contribution to the magnetocrystalline anisotropy is made by the lanthanide atoms. In the lanthanide ions with a non-zero orbital magnetic moment, strong spin–orbit coupling is present, giving rise to single-ion anisotropy.[12,17] Exchange interaction couples the magnetic moments of the lanthanide and transition metal. The additional non-metal elements (boron, nitrogen) give rise to a strong anisotropic crystal field and, hence, induce the anisotropy of lanthanide, which is transmitted to the transition metal sublattice.[12] Finally, anisotropy of the lanthanide ion affected by both exchange and crystal fields controls the direction of the easy axis of magnetization of the whole compound, which may account for the appearance of uniaxial anisotropy. The major contribution to the anisotropy can be estimated as $A_{20}B_{ex}^2$, where A_{20} is the coefficient of the crystal field splitting at the lanthanide ion, B_{ex} is the 3d–4f exchange field on this ion. The coefficient A_{20} is temperature independent, whereas B_{ex} considerably depends on temperature, which may account for the characteristic decrease in the coercivity on heating as T_C is approached. The form and the nature of this dependence have not yet been clarified.[49,50]

The first magnetocrystalline anisotropy constant of $Nd_2Fe_{14}B$ (K_1) is rather high, being 4.9×10^6 J m^{-3} (4.9×10^7 erg cm^{-3});[7] however, this is not the absolute record.[16] Nevertheless, in combination with high magnetization, this value is sufficient for the fabrication of magnets with the record-high energy product. The similarity of the f-electron configurations of Nd^{3+} and Dy^{3+}, Tb^{3+}, Pr^{3+} (Fig. 3) can explain why the strong uniaxial anisotropy in the Nd_2Fe_{14} type phases is retained when neodymium is replaced by these elements.[12] The 3d transition metal is responsible for greater final magnetization: in $Nd_2Fe_{14}B$, the contribution of iron is 31 μ_B, while neodymium brings only 6 μ_B per formula unit.[51]

The magnetic structure of $Nd_2Fe_{14}B$ is fairly complex and has not yet been studied in detail. The crystal structure of this phase has two crystallographically different neodymium positions: 4f and 4g. At room temperature, the magnetic moments in the 4g positions point along the [001] direction of the crystal and have a strong magnetocrystalline anisotropy; therefore, it is believed that they are responsible for the direction of the easy magnetization axis. Meanwhile, there are indications that the magnetic moments in the 4f positions are not collinear to other ones, being mainly directed along [110] (Fig. 4), and behave as a softer magnetic phase in comparison with Nd_{4g}, which perturbs the total magnetocrystalline anisotropy.[51,52] A spin reorientation transition was detected experimentally at $T_s \approx 130$ K.[53] As a result, the total magnetization vector deviates below T_s from the $\langle 001 \rangle$ axis towards $\langle 110 \rangle$, and the whole structure is no longer collinear. Using neutron diffraction, it was found that the reorientation transition is preceded by lowering of symmetry from tetragonal (space group $P4_2/mnm$) to orthorhombic (space group Cm).[54]

Iron atoms occupy six different positions in the crystal lattice ($16k_1$, $16k_2$, $8j_1$, $8j_2$, 4e, 4c), and their magnetic moments are ferromagnetically coupled with the magnetic moments of neodymium, as was detected in both neutron

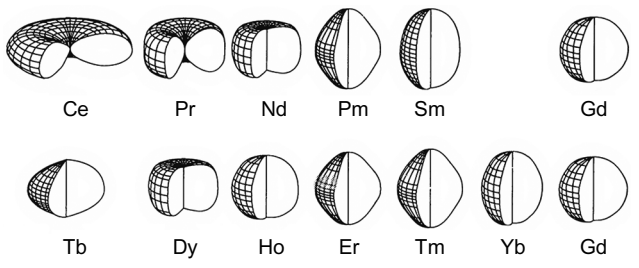


Figure 3. Geometry of 4f electron shells of lanthanide ions.[58] Published with permission from Springer.

§ The rare earth elements, including yttrium, are designated in this review by Ln, although yttrium does not belong to the lanthanide group.

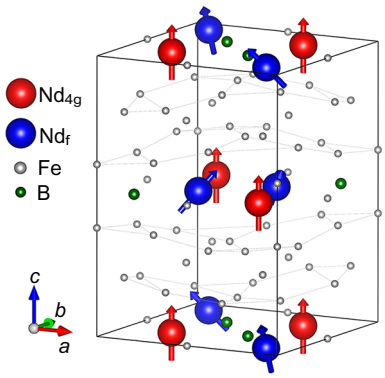


Figure 4. Crystal structure and magnetic subsystem of $Nd_2Fe_{14}B$. The arrows mark the directions of the magnetic moments of ions. The figure was created by the authors using published data.[32, 51, 52]

and muon experiments.[55–57] At the same time, an *ab initio* calculation for ions located on the particle surface demonstrated that the magnetic moments of neodymium are directed oppositely to the magnetic moments in the bulk,[32] and the exchange anisotropy which arises because of this on the particle surface can make an additional contribution to coercivity.[30] The Curie temperature of the lanthanide-containing magnets is largely determined by the exchange interaction in the transition metal sublattice (d–d exchange). In the case of $Nd_2Fe_{14}B$, it can be increased by replacement of the iron atoms by cobalt or another element. The interaction between the lanthanide and transition metal sublattices (d–f exchange) also makes some changes, but since the amount of the transition metal is much higher than the amount of lanthanide, the exchange interaction between lanthanide ions (f–f exchange) is usually negligibly low.[12]

The industrial production of the highest-energy magnets of the Nd–Fe–B system is performed by sintering of magnetically oriented powders of the approximate composition $Nd_2Fe_{14}B$ (or $Nd_{11.8}Fe_{82.3}B_{5.9}$) with a slight excess of neodymium.[16, 59] The primary stage of the process is casting of thin strips of the melt with the approximate composition $Nd_{14}Fe_{80}B_6$. The alloys thus formed are annealed under hydrogen for cracking and then ground in a jet mill (grinding takes place when particles collide in a stream of high-pressure gas or vapour) to form a powder with a particle size of ~1–5 μm.[46] The powder is pressed in a magnetic field, so that particles are aligned along the easy magnetization axis, sintered at temperatures of ~1000–1100 °C (Ref. 60) and quenched to room (or higher) temperature. This may be followed by several post-annealing stages.

The process is carried out under inert atmosphere or in vacuum, as all lanthanides have high affinity for oxygen and air (especially at high humidity and/or elevated temperature). The oxidation can take place at any stage of manufacturing of the magnet, and it can be affected by not only gas-phase oxygen, but even by the material of the crucible.[61] As the lanthanide is gradually oxidized, the alloy composition and magnetic properties change. The oxygen affinity of various rare earth elements is highly variable: light lanthanides are usually less stable than heavy lanthanides or yttrium, but the latter are also oxidized in air. The oxidation is facilitated by open porosity and microcracks; therefore, this effect is most pronounced for films or powders. The finished massive products are also susceptible to slow oxidation; therefore, at the final stage, the products are usually coated by nickel, copper, polymers or other insulating materials.

An excess of neodymium, incongruent melting, air-sensitivity and metastability of the $Nd_2Fe_{14}B$ phase give rise to impurity inclusions: metallic neodymium (fcc-Nd and dhcp-Nd), oxides (fcc-NdO, hcp-Nd_2O_3 and $NdO_{2-\delta}$ with a fluorite structure), $NdFe_4B_4$ and so on. These inclusions are usually located at a triple grain boundary or between the crystallites of the main $Nd_2Fe_{14}B$ phase (Fig. 5). These inclusions are most often amorphous, but in some studies,[62, 63] both amorphous and crystalline inclusions were found. Since the relative amount of impurity phases is relatively low or they are amorphous, they cannot be identified by X-ray diffraction. The phase composition of neodymium magnets is usually investigated by surface techniques such as transmission (TEM) or scanning (SEM) electron microscopy. Due to the small surface area that can be examined by electron microscopes, specific sample preparation and low phase contrast of most impurity compounds, the real phase composition of the magnet can substantially differ from the nominal composition.[62] Therefore, studies of the phase composition and its effect on the final properties of neodymium magnets are still in progress. The key result of the studies that have been already

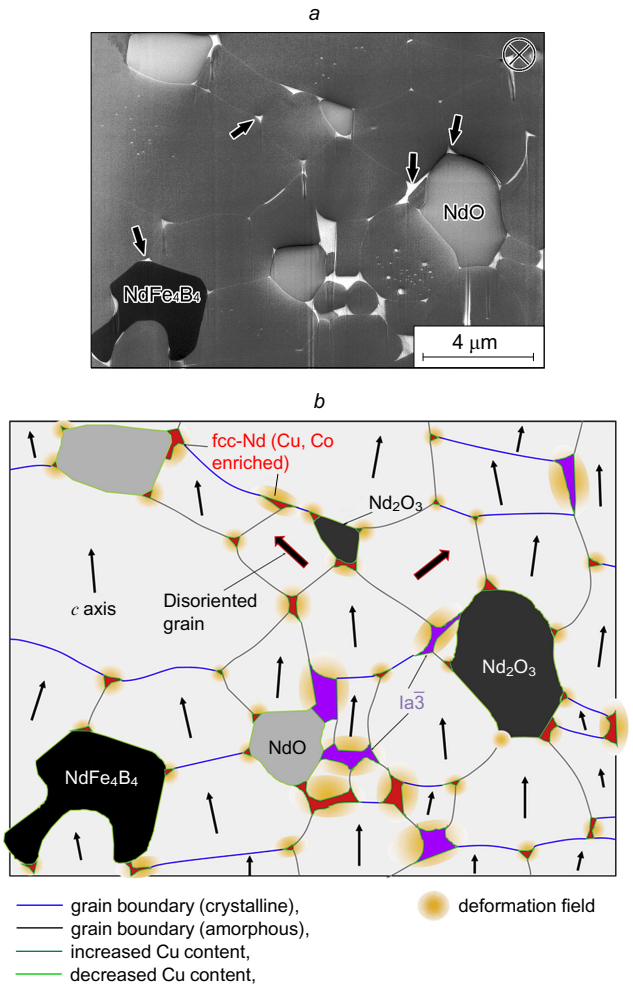


Figure 5. Secondary electron SEM image of Nd–Fe–B ceramics after the sintering and post-annealing (*a*) and schematic view of the ceramic microstructure (*b*).[62] *a*: the dark-gray areas correspond to the crystalline grains of the $Nd_2Fe_{14}B$ phase; light areas are neodymium-rich phases and grain boundaries. *b*: $Ia\bar{3}$ is the neodymium-rich phase of the approximate composition $Nd_{92.6}Fe_{2.5}Co_{0.7}Cu_{4.2}$. Thin arrows show the direction and the modulus of grain magnetization. Published with permission from Elsevier.

completed can be formulated as follows: the coercivity can be increased if a proper microstructure is attained using impurity phases.

The industrial rare earth metal magnets based on Nd–Fe–B and Sm–Co phases consist of multidomain particles, and nucleation of magnetic domains at grain boundaries is considered to be the main mechanism determining the coercivity of the material.[64] It was suggested that neodymium ions located on the surface of (001) crystallites can serve as nucleation centres for domain walls.[32] Therefore, for increasing the coercivity, it is necessary to form a 'pinning' layer, which would prevent the nucleation and motion of domain walls owing to stronger magnetocrystalline anisotropy, exchange mismatch or insulating properties. This problem is successfully solved for neodymium-rich non-ferromagnetic phases. For this purpose, excess neodymium is added to the initial batch, and the sintered piece is post-annealed at temperatures of ~400–900 °C. During post-annealing, clearly defined grain boundaries consisting of neodymium-rich alloys are formed. This considerably affects the exchange and magnetostatic processes at grain boundaries and suppresses the nucleation and motion of domain walls.[16, 63] Neodymium-enriched alloys are not only located at grain boundaries, but also fill gaps at the boundary between the main $Nd_2Fe_{14}B$ phase and grains of impurity phases.

Impurity phases play an important role in the formation of microstructure of magnets based on Nd–Fe–B alloys. However, for attaining high $(BH)_{max}$, remanent magnetization M_r should be high. This requires minimization of the content of non-ferromagnetic impurity phases, while the ferromagnetic impurity phases should be either isolated from the main phase or have nanometre size; in this case, it is possible to enhance their anisotropy *via* exchange coupling with the main phase.[65] Since the intergrain layer of industrial magnets usually contains ~10 at.% impurity phases, which often make no contribution to magnetization, the theoretical upper limit for $(BH)_{max}(\text{theor.}) = \mu_0(0.9M_s)^2/4 = 412$ kJ m^{-3} (52 MG Oe).[46] Nevertheless, this bar was raised to 474 kJ m^{-3} (59.6 MG Oe) by attaining high density of the material and minimizing the percentage of impurity phases to <2%.[48]

High magnetic fields up to 11 140 kA m^{-1} (140 kOe) are applied in primary sintering and post-annealing processes to increase the coercivity.[66] This not only allows the particles of the main phase to be aligned along their easy magnetization axis, but also leads to a better match between the lattices of main and impurity phases at the grain boundaries during hardening. In some cases, the increase in the coercivity after post-annealing in the magnetic field reaches 25%. However, this effect is not observed for all compositions and, moreover, different cooling conditions after post-annealing are required for different compositions (in a field or without a field; fast or slow cooling).[66] The cooling rate affects $(BH)_{max}$ in all stages of the manufacture of neodymium magnets.

Since grain boundaries are formed as a result of partial melting of neodymium metal phases during post-annealing, the process temperature can be reduced by forming eutectics with other metals. The binary M–Nd or ternary M–Fe–Nd phases are formed by metals such as Al, Cu[60] and Ga.[67, 68] Other metals like Ti, Zr, V, Mo, Nb and W form M–B or M–Fe–B alloys. It is also possible to add lanthanide-containing systems such as Pr–Cu,[69] Dy–Ni,[70] Dy–Cu,[71] Dy/Tb–F (see ¶),[72] Tb–Co,[73] Dy–Co–Cu–H,[74] Dy–Fe–Cu, Dy–Fe, Dy–H, Pr–Dy–Al/Cu–H [75] and their various combinations containing up to six (or more) metals and other elements, which are used in various stages of magnet manufacture. As a result, a layer enriched with these elements appears between $Nd_2Fe_{14}B$ grains and isolates the grains from one another. It is believed that this prevents the exchange coupling between them, generates exchange and magnetocrystalline anisotropy on the particle surface and thus suppresses the propagation of domain walls and increases the coercivity.[60] This approach can also enhance the corrosion resistance of the material (due to higher chemical stability of impurity phases). However, the mechanisms of H_c increase in these materials can be different and, in many cases, has not yet been completely clarified. Therefore, in some publications, it is stated that the best properties are attained when the annealing is carried out either slightly above or slightly below the eutectic temperature of the alloys.[69] The oxidation with oxygen to give neodymium oxides and other phases also has an effect, not always adverse, on the microstructure.[70]

One more possible mechanism (if metals are added during the primary sintering) is selective replacement of the soft magnetic 4f positions of neodymium; this is also expected to increase coercivity by removal of the perturbing magnetic moments of neodymium.[51] However, such a deliberate substitution of particular positions is not always possible; in reality, substitution of both 4f and 4g neodymium positions takes place more often. When Nd is replaced by Dy, Tb or Pr,[76] or Fe is replaced by Co,[8] Ni, Cr, Cu, Ga or Al, the magnetic properties can considerably change. Usually, the substitution is aimed at modifying particular characteristics, but this is certainly accompanied by some changes in physical properties of the material: saturation magnetization, Curie temperature (Co, Ga), reorientation transition temperature (Pr), magnetocrystalline anisotropy (Dy, Tb), *etc*. If crystallites of soft magnetic phases such as Nd–(Fe,Co/Ni/Cr) or Laves phases like $Nd(Fe,Co/Ni/Cr)_2$ are formed during the synthesis, this significantly decreases the final coercivity of the material.[16] Boron is sometimes replaced by carbon,[77] although this does not noticeably improve magnetic properties.[6]

Currently, the replacement of neodymium by dysprosium is, perhaps, used most often to modify $Nd_2Fe_{14}B$. Previously, Dy was added only during preparation of the melt, which resulted in partial replacement of 'light' neodymium by 'heavy' dysprosium to give $(Nd_{1-x}Dy_x)_2Fe_{14}B$. An increase in the dysprosium content increases the anisotropy field of the compound and the highest attainable coercivity (Fig. 6). However, the key incentive is to increase the H_c stability to heating, which is too low for many applications in the magnets based on the $Nd_2Fe_{14}B$ phase alone. However, since the magnetic moment of dysprosium is higher than that for neodymium and 'heavy' dysprosium is prone to antiferromagnetic coupling with iron,[16, 46] the saturation magnetization appreciably decreases.[78, 79] To avoid the decrease in M_s and retain high $(BH)_{max}$ value, it was proposed to add dysprosium at the post-annealing stage.[72] Since the coercivity of multidomain $Nd_2Fe_{14}B$ particles is determined by how easily domains are formed at grain boundaries, it can be increased by locally increasing

¶ Hereinafter, a slash (/) between the elements means 'or'.

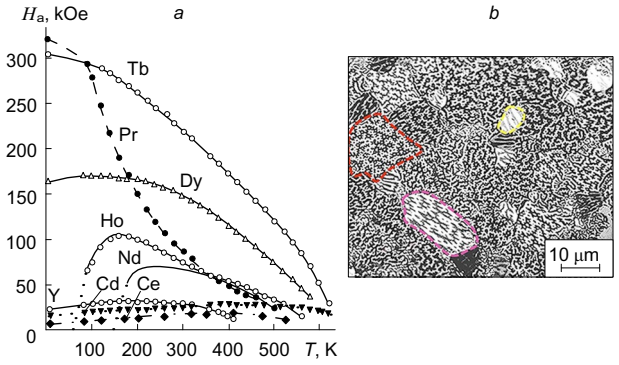


Figure 6. Temperature dependences of the anisotropy field of $Ln_2Fe_{14}B$ single crystals (*a*)[46,81] and Kerr microscopy image of the magnetic domains (some grain boundaries are marked in red) and microstructure of a ceramic sample produced from the $Nd_{30.3}Pr_{0.1}Fe_{64.12}Co_{4.1}Ga_{0.46}B_{0.92}$ powder (*b*).[71] The grain boundaries of the magnet are modified with the Dy–Cu alloy. Published with permission from Elsevier and AIP Publishing.

the anisotropy field H_a. Such a structure is called core/shell by some authors and it is used to improve H_c not only for magnets based on the $Nd_2Fe_{14}B$ phase, but also for many other systems.[75] For attaining a coercivity of $\sim$2387 kA m^{-1} ($\sim$30 kOe), both processes are used, that is, replacement of Nd by Dy in the main phase and enrichment of grain boundaries (see Fig. 6).[71,78] As a result, the coercivity of these magnets can reach 3183 kA m^{-1} (40 kOe) upon 40% substitution, although $(BH)_{max}$ greatly decreases because of the ferrimagnetic nature of the magnetic subsystem. The values H_c = 477–637 kA m^{-1} (6–8 kOe) and (BH)max = 150 kJ m^{-3} (19 MG Oe) inherent in the $(Nd_{0.7}Dy_{0.3})$–Fe–B magnets at 200 °C are still rather high and, hence, these magnets can be used in electric generators.[80]

To our knowledge, the highest coercivity reported in the literature for Nd–Fe–B alloys referred to materials based on terbium-modified phase with the $Nd_2Fe_{14}B$ structural type. The replacement of Nd by Tb, like the replacement by Dy, gives rise to antiferromagnetic exchange interaction with iron, which decreases the saturation magnetization and, hence, also the energy product. Better characteristics are found for materials in which the grain boundaries are coated by TbH_3 nanoparticles. The samples are annealed for complete removal of hydrogen. The coercivity can be as high as 3748 kA m^{-1} (47.1 kOe), with $(BH)_{max}$ remaining relatively high, being 308 kJ m^{-3} (38.5 MG Oe). When larger, micrometre-scale, particles of terbium hydrides and fluorides are used, the results are markedly more modest, presumably, due to the formation of impurity fluoride phases or partial residual solubility of hydrogen in the magnet.[82]

The attempts to replace expensive dysprosium by cheaper elements such as cerium or yttrium brought some success, but did not yet provide sufficiently high performance parameters that would stimulate the industry to completely abandon the dysprosium-substituted neodymium magnets. The Y^{3+} ion has no magnetic moment, but it still can generate an anisotropy field that is much less temperature-dependent than the fields of Dy–$Nd_2Fe_{14}B$ phases. Recently, composites with simultaneous replacement of Nd by Y and formation of a core/shell microstructure were obtained. At high temperatures, these materials showed even better characteristics than Dy–$Nd_2Fe_{14}B$ with low substitution.[83] The cheapest rare earth element, cerium, has absolutely different chemical properties. Unlike neodymium, it tends to exist in +4 oxidation state. In compounds like $Ce_2Fe_{14}B$, the oxidation state of cerium is variable, fluctuating between +3 (S = 1/2) and +4 (S = 0) (on average, +3.44) at a frequency of $\sim$10–13 Hz. Therefore, the magnetization of $(Nd_{1-x}Ce_x)_2Fe_{14}B$ sharply decreases. Additional replacement of iron by cobalt to the composition $(Nd_{0.8}Ce_{0.2})_{2.4}(Fe_{12}Co_2)B$ slightly increases $(BH)_{max}$, while T_C can be brought to 422 °C; however, this would be accompanied by a considerable decrease in the coercivity. These magnetic materials could be useful for high-temperature applications in those cases where low cost is more important than excellent characteristics.[84]

Other types of material with unprecedented magnetic characteristics were obtained owing to the development of new synthetic approaches. The coercivity of particles is known to increase as the single-domain limit is approached. However, the standard industrial treatment of the Nd–Fe–B melt in a jet mill can give particles not less than 1 μm in size. Other procedures (in particular, hot working of alloys) made it possible to obtain 300 nm wide and 50–80 nm thick platelet-shaped grains, while avoiding the adverse effect of oxygen. By isolating the grains from one another, *e.g.*, by enriching the grain boundaries with neodymium and copper under the expansion constraint, it is possible to reach a coercivity of 159 kA m^{-1} (20 kOe), a saturation induction (B_s) of 1.36 T (13.6 kOe) and $(BH)_{max}$ = 358 kJ m^{-3} (45 MG Oe) at room temperature and $(BH)_{max} \approx$ 191 kJ m^{-3} (24 MG Oe) at 200 °C; this is higher than this parameter for Dy-containing magnets.[80]

A set of single-domain particles magnetically oriented along the easy magnetization axis is considered to be an ideal microstructure for attaining high coercivity in single-phase materials. The coercivity of these magnets is theoretically restricted according to the Stoner–Wohlfarth model and cannot exceed the anisotropy field $H_a \approx 2K_1/\mu_0 M_s$.[27,85] For $Nd_2Fe_{14}B$, the anisotropy field amounts to 5570–6366 kA m^{-1} (70–80 kOe), which is several times higher than the coercivity of magnets based on this compound. The multiphase nature of the material and the multidomain nature of the grains are the main causes for the fact that the theoretically possible coercivity of neodymium and samarium magnets is never achieved in practice. Over the last 30 years, new procedures for manufacturing of finely dispersed particles of rare earth metal magnets have been developed; however, the appearance of these particles brought about new problems that are to be overcome, before it is possible to develop magnets with unprecedented characteristics. The key problem is lanthanide oxidation, which becomes more intense due to the increase in the surface area. One more problem is the appearance of soft magnetic impurity phases such as α-Fe in the Nd–Fe–B system. It was noted above that the presence of these phases considerably decreases the coercivity of neodymium magnets, and this cancels the benefit from attainment of the nanoscale size of particles.

Particles with a grain size of 10 to 500 nm can be obtained by high-energy ball milling,[86] melt spinning, mechanical doping, hydrogenation–disproportionation–desorption–recombination (HDDR) process,[16] chemical synthesis with microwave annealing and other methods.[87] Using HDDR process, it is possible to obtain ultradispersed

$Nd_2Fe_{14}B$ grains; however, their coercivity does not exceed 1353 kA m^{-1} (17 kOe) since the intergrain phase is ferromagnetic.[46] Recently, it was proposed to form a nano-grain structure composed of 100–200-nm $Nd_2Fe_{14}B$ grains in the matrix of an impurity phase by means of laser 3D printing. The coercivity of these magnets did not exceed 1353 kA m^{-1} (17 kOe).[88] Single-domain particles are often separated and isolated using the same procedures as used for multidomain grains. For example, by enrichment of grain boundaries with neodymium, it is possible to reach a coercivity of 2188 kA m^{-1} (27.5 kOe).[85]

3.2. Magnetic materials based on Sm–Co phases

Magnets based on alloys of the Nd–Fe–B system have remarkably high $(BH)_{max}$ values, while samarium $SmCo_5$ magnets have a record-high anisotropy field: H_a is 32 MA m^{-1} (400 kOe) at room temperature [16,89] and increases to 48–56 MA m^{-1} (600–700 kOe) at temperatures close to absolute zero. The coercivity of the industrial sintered $SmCo_5$ magnets at room temperature is, on average, not higher than 1592 kA m^{-1} (20 kOe).† In some cases, the H_c value can be increased up to 3183 kA m^{-1} (40 kOe) and even to 5173–5968 kA m^{-1} (65–75 kOe) through modification with other elements, but, as a rule, only in laboratory. For example, at 4.2 K, the coercivity of substituted $SmCo_2Cu_3$ magnets can reach 24 MA m^{-1} (300 kOe);[90] however, they become paramagnetic at temperatures slightly above the room temperature.[91]

For practical applications, it is important that the Curie temperature of $SmCo_5$ (720–747 °C) is much higher than that of the $Nd_2Fe_{14}B$ phase; therefore, the coercivity remains relatively high, ranging from 398 to 557 kA m^{-1} (5–7 kOe), even at 300 °C.

In combination with relatively low saturation induction and saturation magnetization [$B_s \approx 1.14$ T (11.4 kG) and $M_s = 107.3$ A m^2 kg^{-1} (107.3 emu g^{-1})], the energy product of magnets based on $SmCo_5$ alloys is twice lower than that of neodymium magnets and, at room temperature, it is on average 120–200 kJ m^{-3} (15–25 MG Oe),[89,92] which is close to the theoretical limit $(BH)_{max}$(theor.) ≈ 219–260 kJ m^{-3} (27.5–32.7 MG Oe).[79] The $PrCo_5$ alloys with a relatively high Curie temperature of ~600–650 °C (the T_C value is highly variable in different published sources), $B_s = 1.23$ T (12.3 kG) and $(BH)_{max}$(theor.) ≈ 320 kJ m^{-3} (40.2 MG Oe) are considered to be promising; however, synthetic difficulties associated with attainment of reasonable coercivity and energy product do not yet allow them to replace samarium magnets.[93–96]

The attempts to increase magnetization resulted in the synthesis of a number of compounds Ln_2Co_{17} with a higher cobalt content, which were described in more detail in a review.[79] Among Ln_2Co_{17}, high saturation magnetization is inherent in Lu_2Co_{17}, Pr_2Co_{17}, Nd_2Co_{17}, Yb_2Co_{17} and Sm_2Co_{17} [$B_s = 1.25–1.4$ Tl (12.5–14 kG), $M_s \approx 115$ A m^2 kg^{-1} (115 emu g^{-1})]; however, only Sm, Er and Tm compounds have a uniaxial anisotropy. Furthermore, the T_C value of Sm_2Co_{17} is among the highest ones (~920 °C). These two factors in combination with the relatively high saturation magnetization and $(BH)_{max}$(theor.) ≈ 312 kJ m^{-3} (39.2 MG Oe) account for the popularity of samarium compounds among Ln_2Co_{17}. Nevertheless, the anisotropy field of Sm_2Co_{17} is 4775–5570 kA m^{-1} (60–70 kOe),[97] which is several times lower than that of $SmCo_5$. The values $(BH)_{max} \approx 160–250$ kJ m^{-3} (20–31 MG Oe)[79] attained practically for magnets based on the Sm_2Co_{17} phase are still much lower than those of magnets based on Nd–Fe–B alloys. Since a high-coercivity state could not be attained for magnets based on pure Sm_2Co_{17} phase, cobalt was replaced by iron or manganese to increase the coercivity. Higher coercivity and $(BH)_{max}$ of up to 264 kJ m^{-3} (33 MG Oe) and above were attained by using additives and by replacement of Co by Fe, Cu and Zr. It is noteworthy that increase in the iron content is important for increasing the energy product; however, this often leads to a considerable decrease in the coercivity.

Owing to the high Curie temperature, the magnetic properties of the Sm–Co alloys are much more resistant to heating. Thus intermetallics $Sm(Co,Cu,Fe,Zr)_z$, where $z = 7–8$, which show one of the highest $(BH)_{max}$ values among all samarium compounds, may demonstrate energy products > 100 kJ m^{-3} (12.6 MG Oe) even at 400 °C.[16] The coercivity of these magnets is also higher than those of pure $SmCo_5$ or Sm_2Co_{17} and reaches 2785 kA m^{-1} (35 kOe) at room temperature.[98,99] These materials are biphasic and consist of the main Sm_2Co_{17} phase and $SmCo_5$ phases located at grain boundaries. When cobalt is replaced by Cu, Ti or Zr, the Curie temperature and anisotropy at the grain boundaries increase, which leads to pinning (delay of the domain wall displacement) and thus delays the displacement of domain walls at temperatures ⩾400 °C.[12] Recent publications demonstrate [100,101] that even for iron-rich phases [*e.g.*, $Sm(Co_{0.68}Fe_{0.22}Cu_{0.07}Zr_{0.03})_{7.5}$], the coercivity can be increased from 1943 kA m^{-1} (24.42 kOe) to 2737 kA m^{-1} (34.39 kOe) by decreasing the number of grains at the boundaries and changing the nature of microstructure defects generating non-uniform pinning centres.

Like in alloys of the Nd–Fe–B system, in the Sm–Co magnets, the rare earth element is responsible for the high magnetocrystalline anisotropy along the *c* axis [$K_1 = 17 \times 10^6$ J m^{-3} (17×10^7 erg cm^{-3}) for $SmCo_5$ (Ref. 102) and 3.3×10^6 J m^{-3} (3.3×10^7 erg cm^{-3}) for Sm_2Co_{17} (Ref. 103)].[104] However, there are considerable differences between the behaviours of Sm^{3+} and Nd^{3+}. The spin–orbit coupling results in a different, more oblong shape of the f electron shell of samarium (see Fig. 3); as a result, many samarium compounds possess record-high anisotropy fields. In addition, the Sm^{3+} ground state has the $4f^5$ configuration ($L = 5$, $S = 5/2$) and the term $^6H_{5/2}$. However, the energy of the multiplet state with $J = 7/2$ and $^6H_{7/2}$ is close to the ground state term; hence, mixing of states can take place in a sufficiently strong exchange field or at high temperature.[105] This mainly affects only contributions to high (sixth) order anisotropy, which is often ignored in calculations. However, this contribution can be significant at high temperature.[12]

The increase in the magnetocrystalline anisotropy energy in the samarium sublattice caused by addition of diamagnetic atoms (*e.g.*, boron) results in even higher fields of anisotropy compared to $SmCo_5$.[106,107] The anisotropy field of $SmCo_5$ at 4.2 K is 95.5 MA m^{-1} (1200 kOe),[108] while that of $Sm_2Co_7B_3$ is 103.5 MA m^{-1} (1300 kOe). However, the presence of additional chemical elements decreases the magnetization and weakens the exchange interaction in the transition metal sublattice; therefore, the Curie temperature of these magnets decreases, being 243, 173 and 129 °C for $SmCo_4B$, $Sm_3Co_{11}B_4$ and $Sm_2Co_7B_3$,

† See https://www.strongsmagnet.com/products-tid-4.html (access date 19 July, 2021).

respectively.[109] At room temperature, the anisotropy field of $Sm_2Co_7B_3$ decreases to 10.7 MA m^{-1} (135 kOe).[110] The small number of publications devoted to these compounds with high magnetic characteristics is apparently attributable to the complexity of their synthesis and low thermal stability of magnetic properties.

The $SmCo_5$ structure refers to the $CaCu_5$ type, and the Sm_2Co_{17} oxide may have either Th_2Zn_{17} or Th_2Ni_{17} type structure. The Sm_2Co_{17} structure is related to $SmCo_5$ *via* replacement of one-third of samarium positions by pairs of cobalt atoms (usually called cobalt dumbbells). If the dumbbell distribution in the samarium positions is ordered, this gives the structures indicated above. If the dumbbells are randomly distributed, structure of a third, $TbCu_7$, type is formed. The structural diversity of Sm_2Co_{17} accounts for the difficulties faced by attempts to control the magnetic properties of compounds, since the final phase composition appreciably depends on the method of preparation.[111] The abnormal temperature behaviour of the coercivity of samarium magnets is attributable to the phase and structural transformations of the main and intergrain phases, particularly, to the presence of a high-temperature maximum of H_c, which considerably depends on heat treatment parameters (Fig. 7).[112, 113] In Sm–Co phases, magnetic moments are ferromagnetically coupled (Fig. 8), with the magnetism of the transition metal being often itinerant, whereas the magnetic moment of samarium is considered to be localized.[57]

The production process for industrial magnets based on Sm–Co alloys is similar to that used for Nd–Fe–B-based magnets and includes the following stages:

— formation of the alloy,
— preparation of the powder,
— powder compression in a magnetic field,
— sintering,
— tempering and quenching,
— post-annealing.

However, since samarium is prone to vaporization due to high vapour pressure, not all of the procedures are admissible for the preparation of the primary melt, and additional excess of samarium is needed to make up for its loss.[92] Heat treatment parameters (temperature ranges, cooling rate) are also different. The final microstructure of the industrial $SmCo_5$ magnets is composed of multidomain grains of 5–10 μm size aligned along the easy magnetization axis, and the nucleation of domain walls is the key mechanism responsible for coercivity.[16] Pinning is considered to be the main mechanism determining H_c in Sm_2Co_{17}, unlike that in $SmCo_5$, although some studies published in 2020 indicate that both mechanisms are implemented in Sm_2Co_{17} (see, *e.g.*, Ref. 99).

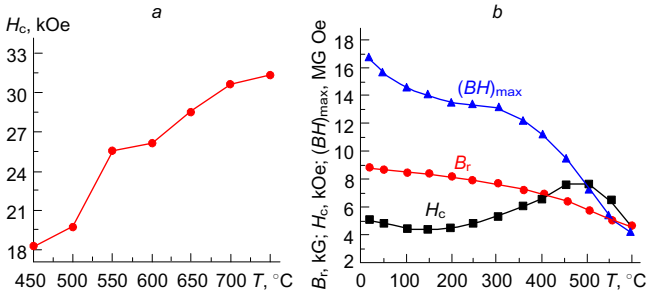


Figure 7. Dependence of the coercivity on the temperature of a 30-minute post-annealing of amorphous alloys of the $SmCo_5$ nominal composition for the production of magnets by crystallization of the amorphous phase (*a*)[112] and temperature dependences of the magnetic characteristics of $Sm(Co-Fe-Cu-Zr)_{7.69}$ alloys sintered at high temperatures (*b*).[113] Published with permission from Elsevier and AIP Publishing.

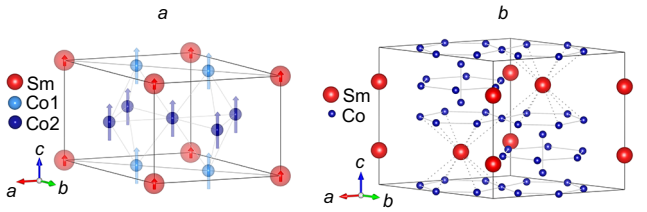


Figure 8. Crystal structures of $SmCo_5$ (*a*) and Sm_2Co_{17} (space group $P6_3/mmc$) (*b*). The arrows mark the directions of the magnetic moments of ions. The figure was created by the authors using published data.[106, 107, 111]

The $SmCo_5$ phase is metastable and melts incongruently. The slow rate of cooling from 1150 to 850 °C after annealing, which is important for attaining high coercivity, should be, conversely, replaced by quenching at lower temperature in order to avoid eutectoid decomposition into Sm_2Co_{17} and Sm_2Co_7.[114] The low cooling rate in the initial stage and the choice of the optimal post-annealing temperature are necessary for the formation of a defect-free stoichiometric structure of the main $SmCo_5$ phase and samarium-rich grain boundaries;[115] this contributes to increasing coercivity. The multiphase nature, defectiveness and difficulty of attaining stoichiometry due to uncontrolled vaporization of samarium are considered to be the main causes for low coercivity, which does not exceed 20% of H_a.[116]

The Sm_2Co_{17} phase melts congruently, but can be obtained by stabilization of the peritectic reaction

$$L + Co \rightleftarrows Sm_2Co_{17} \quad (7)$$

(L is the melt the exact composition of which is determined by the phase diagram), for example, by adding a small amount of iron.[105] When there is excess cobalt, the eutectic reaction

$$L \rightleftarrows Co + Sm_2Co_{17} \quad (8)$$

takes place and may result in the formation of cobalt inclusions as the impurity phase in the Sm_2Co_{17} matrix. The resulting exchange-coupled composite or multilayer exchange-coupled films based on Sm–Co alloys often demonstrate even better magnetic properties than the pure phase.[117] For instance, $(BH)_{max}$ for $SmCo_5/Fe/SmCo_5$ three-layer films can reach 400 kJ m^{-3} (50 MG Oe).[118] The theoretical limit of $(BH)_{max}$ for these exchange-coupled magnets is estimated as 700–800 kJ m^{-3} (88–100 MG Oe).[119]

Reasonably good characteristics were also found for other phases of the Sm–Co and Sm–Fe systems. The unstable Sm_5Co_{19} phase is stabilized as nanoparticles and has a coercivity of up to 3183 kA m^{-1} (40 kOe).[120] The metastable $SmFe_{12}$ phase with the $ThMn_{12}$ type structure can be stabilized by replacing Fe with Ti, Al, C, W, Si, Mo or Nb. As a result, the best characteristics were found for the $SmFe_{11}Ti$ phase possessing an anisotropy field of 15.8 MA m^{-1} (198 kOe) and a Curie temperature of

314 °C, but a relatively low saturation induction of 1.27 T (12.7 kG). The related compound $Sm(Fe_{0.8}Co_{0.2})_{12}$ has even higher magnetic properties: $B_r = 1.78$ T (17.8 kG), $H_a = 9.5$ MA m^{-1} (120 kOe) and $T_C = 586$ °C, while $(BH)_{max}$ for films reaches 630 kJ m^{-3} (79 MG Oe).[8,121] There are quite a few other intermetallic compounds, which are not considered in this review, as their characteristics are not superior to those of $SmCo_5$.

The methods for the fabrication of high-coercivity magnets from single-domain $SmCo_5$ particles, like those for magnets based on the Nd–Fe–B system, have not yet been developed.[103] According to theoretical calculations, the single-domain limit of $SmCo_5$ is 740–870 nm for spherical particles,[122] although estimates from 200 to 1800 nm are also encountered. The superparamagnetic limit is only 2–3 nm. However, the single-domain limit has not yet been determined experimentally. The nearly square hysteresis inherent in single-domain particles was attained for 180-nanomentre $SmCo_5$ nanoparticles stabilized by nitrogen-doped graphite, which were synthesized in reverse micelles. The coercivity equal to 1989 kA m^{-1} (25 kOe) at room temperature and 4058 kA m^{-1} (51 kOe) at 150 K was fairly far from theoretical values.[122] The single-domain limit of particles obtained by co-precipitation followed by the reduction-diffusion with calcium was estimated as 823 nm.[102] However, as a proof, the authors used not a very weighty argument, that is, the fact that the maximum coercivity, which is not higher than 2.6 MA m^{-1} (33.1 kOe), is attained exactly for this size. The causes for relatively low coercivity in all of these cases are similar to those for phases of the Nd–Fe–B system: lanthanide oxidation and formation of impurity phases.

Nevertheless, other researchers (see, *e.g.*, Ref. 123) succeeded in obtaining a material based on 200–400 nm $SmCo_5$ nanoparticles that had the highest coercivity ever attained for magnetic nanoparticles — 5.3–5.7 MA m^{-1} (66–72 kOe) at room temperature. However, this is still 4–5 times smaller than the anisotropy field. This result was obtained by aligning the nanoparticles in a 637 kA m^{-1} (8 kOe) magnetic field during curing of epoxy resin.[123] The authors presented evidence indicating that their particles are still multi-domain, with the size of single-domain regions being ~80 nm. The nucleation of domain walls in the particles smaller than the theoretical single-domain limit can be due to a local decrease in the magnetocrystalline anisotropy in the oxidized surface layer of nanoparticles.

Theoretically, anisotropic rod-like particles should show better results than spherical particles owing to the shape anisotropy and the possibility of their rather precise alignment along the easy magnetization axis. The high-energy milling or thermal reduction with calcium may be used to prepare anisotropic particles from samarium and cobalt oxides; however, the samples are usually highly contaminated by the oxidation products; grains often form sintered agglomerates, which are very difficult to appropriately orient.[92,124] An approach to the synthesis of separate single-crystalline anisotropic rod-like or flat hexagonal $SmCo_5$ and Sm_2Co_{17} particles was developed only several years ago.

One of the ways to solve this problem for $SmCo_5$ is to select precursors for calcium reduction: samarium oxalate decahydrate $Sm_2(C_2O_4)_3 \cdot 10\,H_2O$ and cobalt hydroxide $Co(OH)_2$ usually form flat crystals, while cobalt oxalate $CoC_2O_4 \cdot 2\,H_2O$ and samarium hydroxide $Sm(OH)_3$ give rod-like crystals. By varying the quantitative ratio of precursors and by adding calcium oxalate to stabilize the particle size, one can obtain either flat hexagonal or rod-like single-crystalline $SmCo_5$ particles.[125,126] The saturation magnetization of some anisotropic particles almost reaches a theoretical maximum,[125] but the coercivity, nevertheless, does not exceed 1592–3183 kA m^{-1} (20–40 kOe).[126] The rod-like Sm_2Co_{17} nanoparticles are obtained by similar methods, but using other starting reactants.[127]

One more promising method for the preparation of anisotropic $SmCo_5$ particles is hot pressing. Recently, anisotropic $SmCo_5$ magnets with a coercivity of 2037 kA m^{-1} (25.6 kOe), a remanent magnetization of 92% relative to the saturation magnetization, and $(BH)_{max} = 110$ kJ m^{-3} (13.8 MG Oe) were obtained by this method with additional alignment of $SmCo_5$ particles by adding Sm_2Co_7 nanophase inclusions, which served as nucleation centres for new grains. An important feature of these magnets is that their parameters change at high temperature: at 300 °C, the coercivity was above 756 kA m^{-1} (9.5 kOe) and $(BH)_{max} = 80$ kJ m^{-3} (10 MG Oe), which is markedly higher than these values for commercial sintered magnets.[128] Many phases of the Sm–Co system (Sm_2Co_{17}, $SmCo_5$, Sm_2Co_7, $SmCo_3$ and $SmCo_2$) can be obtained by electrochemical method in the $LiCl–KCl–SmCl_3–CoCl_2$ chloride melt,[129] which opens up new opportunities for the formation of materials with maximized magnetic parameters.

Selective dissolution was proposed for solving the problem of decreasing magnetization of nanoparticles under the action of impurity phases on the surface. A necessary stage of virtually all procedures used to prepare nanoparticles of the Sm–Co phases from oxides is reduction with calcium [130] or hydrogen;[131] therefore, a calcium and lanthanide hydride and oxide layer is formed on the particle surface.[132] The impurity phases are partially removed by soaking in acid solutions and deionized water; sometimes, sugars are used, but this often does not solve the problem, but instead gives rise to new impurities. A solution of NH_4Cl in methanol was proposed to soak the rod-like Sm_2Co_{17} particles; calcium chloride thus formed is soluble in methanol (3.54 g per 100 g of methanol). The same technique can also be used to increase the magnetization of $Nd_2Fe_{14}B$ and $SmCo_5$ nanoparticles.[133] Although a record-high coercivity has not yet been attained in this way, [the maximum for Sm_2Co_{17} was 637 kA m^{-1} (8 kOe) and that for $SmCo_5$ was 2427 kA m^{-1} (30.5 kOe)], the remanent magnetization have already reached the magnetization of the microdispersed bulk phase obtained by standard methods.[133,134]

This review covers only the most widely used and highest-performance materials and methods for their manufacture. More detailed descriptions of the current state of studies of the magnetic properties and production methods of other rare earth metal compounds can be found in relevant issues of the annual *Handbook of Magnetic Materials*.[6,46]

3.3. Magnetic materials based on Sm–Fe–N phases

Some authors (see, *e.g.*, Refs 135, 136) noted a high potential of compounds $Sm_2Fe_{17}N_x$ ($x = 0.5–6$) with similar Th_2Zn_{17} (space group $R\bar{3}m$) or $TbCu_7$ (space group $P6/mmm$) type structures (Fig. 9). The crystal structure being formed and the properties of magnets based on Sm–Fe–N phases depend appreciably on the method of synthesis; therefore, comparison of the magnetic properties of these phases using data of different publications gives

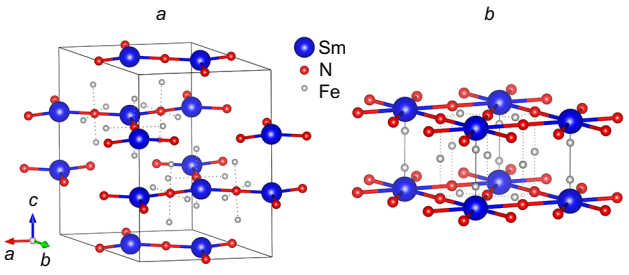


Figure 9. Crystal polymorphs of $Sm_2Fe_{17}N_x$ ($x = 0.5-6$), space groups $R\bar{3}m$ (*a*) and $P6/mmm$ (*b*). The figure was created by the authors using published data.[143, 145, 147]

contradictory results. Nevertheless, most authors agree that compounds with compositions around $Sm_2Fe_{17}N_3$ have the highest coercivity,[137] while the rhombohedral phase with the Th_2Zn_{17} type structure is the most stable. However, some publications state otherwise.[138] Compounds with the $TbCu_7$ structure usually show higher saturated magnetization, because they have higher density.[139] In both $Sm_2Fe_{17}N_3$ structures, three nitrogen atoms surround one samarium atom, thus creating a strong crystal field, which is responsible for the giant magnetocrystalline anisotropy of this compound.

Irrespective of the type of structure, $Sm_2Fe_{17}N_3$ has a uniaxial anisotropy (unlike the parent alloy Sm_2Fe_{17}, which has an easy plane anisotropy) and high saturation magnetization [$B_r \approx 1.5$ T (15 kG) for the phase with space group $R\bar{3}m$], which is comparable with this value for $Nd_2Fe_{14}B$ [~ 1.6 T (16 kG)] and is higher than that for compounds in the Sm–Co system. High anisotropy constants $K_1 = 6.6 \times 10^6$ J m^{-3} (6.6×10^7 erg cm^{-3}) and $K_2 = 3.3 \times 10^6$ MJ m^{-3} (3.3×10^7 erg cm^{-3}) provide for the giant anisotropy field

$$H_a = \frac{2K_1 + 4K_2}{\mu_0 M_s} \quad (9)$$

which is 17.5–20.7 MA m^{-1} (220–260 kOe), according to various estimates. This is markedly higher than that of $Nd_2Fe_{14}B$. Even with allowance for the fact that the coercivity of $Sm_2Fe_{17}N_3$ is controlled by nucleation of domain walls, and the anisotropy field is thus restricted to

$$H_a = \frac{2K_1}{\mu_0 M_s} \approx 8753 \text{ kA m}^{-1} \text{ (110 kOe)} \quad (10)$$

this is still higher than that for $Nd_2Fe_{14}B$.[8] The Curie temperature of $Sm_2Fe_{17}N_3$ is 150 °C higher than that of pristine $Nd_2Fe_{14}B$, which opens up the possibility of using $Sm_2Fe_{17}N_3$ in electric generators.[140, 141] The theoretical limit of the energy product for $Sm_2Fe_{17}N_3$ is estimated to be ~ 475 kJ m^{-3} (59.7 MG Oe).[8] According to calculations based on experimental data for powders, at high temperatures, *e.g.*, in vehicle engines, magnets based on the $Sm_2Fe_{17}N_3$ phase should show even higher energy products than magnets of the Dy-doped Nd–Fe–B system.[141] One more advantage of materials of the Sm–Fe–N system over Nd–Fe–B magnets is high electrical resistance. Composites based on soft magnetic ferrites and $Sm_2Fe_{17}N_3$ have coercivity of ~ 756 kA m^{-1} (9.5 kOe) and specific resistance of up to 4000 μΩ cm, whereas the specific resistance of $Sm_2Fe_{17}N_3$ is 400 μΩ cm, and that of $Nd_2Fe_{14}B$ is only 100 μΩ cm. This opens up the possibility of using $Sm_2Fe_{17}N_3$ composites in high-frequency devices, *e.g.*, magnets for electric vehicles. The use of magnets based on Nd–Fe–B alloys in these devices leads to considerable energy loss due to eddy currents.[142]

Compounds $Sm_2Fe_{17}N_x$ were discovered back in 1990s;[143] however, due to the complexity of synthesis, they still could not become an alternative to neodymium magnets. The Sm_2Fe_{17} alloys cannot be obtained by sintering with partial melting, which is usual for industrial neodymium magnets; because of specific features of the phase diagram, it co-exists with the α-Fe and $SmFe_3$ phases. The subsequent nitriding of the Sm_2Fe_{17} alloy powder with nitrogen-containing gas mixture ($NH_3 + H_2$,[144] $N_2 + H_2$, NH_3) or with N_2,[145] which is a usual stage of production of Sm–Fe–N magnets, can hardly give homogeneous $Sm_2Fe_{17}N_x$ powders due to limiting diffusion and relatively large grain size of the initial alloy. Furthermore, $Sm_2Fe_{17}N_3$ irreversibly decomposes to samarium and iron nitrides and α-Fe at 450–620 °C, *i.e.*, below the melting point (720 °C).[141, 145] Other procedures such as pressing in a magnetic field [146] are also hampered, as the alloy is readily oxidized even with trace amounts of oxygen to give a film of iron and samarium oxides.[147] This can account for a considerable decrease in the coercivity of magnets based on $Sm_2Fe_{17}N_3$ phases, which starts below the decomposition temperature (200 °C): the reaction of iron oxides with the main phase leads to reduction to α-Fe and formation of samarium oxide (Fig. 10).[140, 141, 148, 149, 152]

Soft magnetic α-Fe becomes the nucleation centre for domain walls and cannot stop their propagation during magnetization reversal, which reduces the coercivity of the finished material, while the presence of impurity nitrides and $SmFe_3$ decreases the final saturation magnetization. Thus, a solution may lie in removing the impurity soft magnetic phases, reducing soft magnetic inclusions down to sizes suitable for magnetic-exchange composites and obtaining single-domain particles of the $Sm_2Fe_{17}N_3$ phase, the size of which does not exceed 0.3–0.35 μm according to theoretical estimates, but practically can reach several micrometres.[150] According to a patent,[151] spherical $Sm_2Fe_{17}N_3$ particles have a higher coercivity than elongated ones.

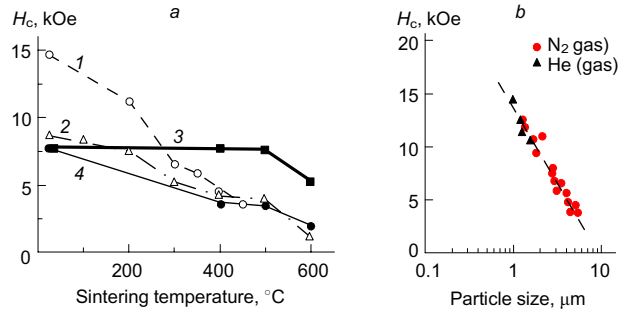


Figure 10. Effect of the surface oxide film on the coercivity of $Sm_2Fe_{17}N_3$ (*a*)[152] and dependence of the coercivity of $Sm_2Fe_{17}N_3$ powders on the particle size after milling in an inert atmosphere, illustrating the tendency towards the single-domain limit (*b*).[141] *a*: coercivity as a function of the powder sintering temperature and procedure: (*1*) hot pressing in the absence of oxygen, (*2*) hot pressing in the presence of oxygen, (*3*) arc plasma sintering, (*4*) spark plasma sintering. Published with permission from AIP Publishing and Elsevier.

Development of new synthetic approaches could help to overcome the above obstacles to wide use of $Sm_2Fe_{17}N_3$-based magnets. The advancement of low thermal load sintering techniques, such as hot pressing and pressing under load, spark plasma sintering or arc plasma sintering, reduction diffusion, *etc.*, opened up the possibility of producing dense bulk $Sm_2Fe_{17}N_3$ magnets at temperatures below their decomposition temperature.[141, 147, 153, 154] For example, using spark plasma sintering at 400 °C, magnetic ribbons (with $TbCu_7$ type structure) with a coercivity of 1345 kA m^{-1} (16.9 kOe) and $(BH)_{max}$ of up to 112 kJ m^{-3} (14 MG Oe) were obtained. The reduction diffusion process,[151] consisting in the annealing of finely dispersed powders of samarium and/or iron oxides in a reducing medium,[155] gave powders of Sm–Fe–N phases with $(BH)_{max}$ up to 292 kJ m^{-3} (36.7 MG Oe).[156] Modification of the reduction diffusion procedure in the stage of precursor preparation resulted in the synthesis of $Sm_2Fe_{17}N_3$ powder composed of submicrometre particles (0.616 ± 0.347 μm) containing no oxide impurities with a coercivity of 1170 kA m^{-1} (14.7 kOe) (see Fig. 10).[157] Modification of the washing step provided the highest coercivity for anisotropic $Sm_2Fe_{17}N$ powders amounting to 2236 kA m^{-1} (28.1 kOe).[136] The highest coercivity [up to 2467 kA m^{-1} (31 kOe)] was found for isotropic powders obtained by fusion under mechanical load.[158] However, even these procedures did not solve the problem of decreasing coercivity and $(BH)_{max}$ due to the formation of oxide phases and their interaction with $Sm_2Fe_{17}N$ during the production of magnets from high-coercivity powders.

The highest risk of formation of the surface oxide film arises in the milling stage (this refers to the standard manufacturing of lanthanide magnets: powder milling → magnet pressing → sintering), because the freshly formed surfaces are chemically reactive due to strong reducing ability of samarium. The oxidation with oxygen may occur *via* the action of surfaces of the milling medium caused by the initial presence of oxides (like in the reduction diffusion process) or the action of atmosphere in which the synthesis takes place. The sintering stage is also problematic, because temperature rise promotes the surface oxidation. In addition, it is necessary to prevent the oxidation during transportation of the material between stages. Under laboratory conditions (in the nitrogen atmosphere of a glove box and using a spiral jet mill), it was possible to manufacture $Sm_2Fe_{17}N_3$ magnets with the coercivity $H_c \approx 557-637$ kA m^{-1} (7–8 kOe) and $(BH)_{max}$ of up to 160 kJ m^{-3} (20.1 MG Oe).[152] The authors attributed this result to the fact that the sintered magnets they obtained had relatively low density, which resulted in low remanent magnetization. By 2020, the $(BH)_{max}$ value of 191 kJ m^{-3} (24 MG Oe) was attained under laboratory conditions owing to the development of oxygen-free sintering procedures.[141] The commercially available NITROQUENCH-P magnets of the Sm–Fe–N system have $(BH)_{max}$ of only 112 kJ m^{-3} (14 MG Oe).‡

The replacement of samarium, iron or nitrogen by other elements provides, in some cases, higher $(BH)_{max}$ values. When samarium is replaced by more naturally abundant yttrium to form $(Sm_{1-y}Y_y)_2Fe_{17}N_x$ ($y = 0-1$), the best characteristics are attained for magnets with $y = 0.4$ obtained by alloy nitriding and annealing at 1000 °C: $B_r = 1.23$ T (12.3 kG), $H_c = 445$ kA m^{-1} (5.6 kOe) and $(BH)_{max} = 197.6$ kJ m^{-3} (24.8 MG Oe). The optimal characteristics were attributed to exchange interactions between the two phases coexisting in this magnet — the standard rhombohedral phase of the Th_2Zn_{12} type and hexagonal phase of the Th_2Ni_{17} type.[159] A simultaneous substitution in the alloy $(Sm_{0.7}Zr_{0.3})_x(Fe_{0.9}Co_{0.1})_{100-x}$ ($x = 9.1-13.4$) leads to stabilization of the metastable phase (with the $TbCu_7$ type structure) in quenching and annealing processes, while the subsequent nitriding affords a powder with a coercivity of up to 859 kA m^{-1} (10.8 kOe).[160]

Modifying additives can also be useful. Currently, the most efficient among them is zinc, which makes it possible to increase coercivity to 2.7 MA m^{-1} (34 kOe). This may be due to the formation of the magnetically insulating γ-FeZn film for soft magnetic phases such as α-Fe or α-FeZn[161] and increased resistance of the initial powder against oxidation.[162] When the temperature increases to 200 °C, the coercivity is still relatively high — 1098 kA m^{-1} (13.8 kOe).[163] The combined milling of powders of the Sm–Fe–N phase with carbon and low-melting zinc followed by annealing can increase the density of the finished magnets, which is important for their industrial applications.[164]

Relying on the phase diagram of the Sm–Fe–Cu system, Lu *et al.*[147] synthesized the Sm_2Fe_{17} alloy (with the Th_2Zn_{17} type structure) with paramagnetic SmCu and $SmCu_2$ inclusions without α-Fe and $SmFe_3$ impurity phases. Nitriding of the alloy furnished a material with a coercivity of 1106 kA m^{-1} (13.9 kOe) and $(BH)_{max} \approx 248$ kJ m^{-3} (31 MG Oe). The addition of 3–9 at.% titanium led to a decrease in the average size of Sm_2Fe_{17} particles that are formed in the reductiion diffusion process down to 0.6 μm,[165] but insertion of titanium into the main phase decreased the coercivity.

The magnetization [and, correspondingly, $(BH)_{max}$] of exchange-coupled MnBi–$Sm_2Fe_{17}N_x$ composites, obtained by grinding of high-purity MnBi ribbons and $Sm_2Fe_{17}N_x$ particles, increased by 37% in comparison with pure MnBi; the final values were 144 kJ m^{-3} (18 MG Oe) at 300 K and ~80 kJ m^{-3} (10 MG Oe) at 380 K.[166]

3.4. Problems and prospects

The main problem of the development of the industry of rare earth metal magnets is shortage of raw materials for producing rare earth elements, which would probably only aggravated with time. Rare earth elements occur in very little amounts both in the Earth and in the outer space. This is due to the fact that the synthesis and release of nuclei heavier than the rubidium nucleus are possible only under very drastic conditions. Some of the elements are formed *via* s-process of neutron capture during the lifetime of low-mass stars and are released after star explosion. The other elements are products of the neutron capture r-process upon fusion of neutron stars.[167] The average contents (C) of neodymium, dysprosium, samarium, cobalt and iron in the Earth's crust and the putative abundances (F) of these metals in the Universe are given below.§

Element	Nd	Dy	Sm	Co	Fe
C (mass %)	0.0033	0.00062	0.0006	0.003	6.3
F (mass %)	10^{-6}	2×10^{-7}	5×10^{-7}	0.0003	0.11

‡ See http://www.daido-electronics.co.jp/english/product/nitroquench_p/index.html (access date 19 July, 2021).

§ See Element Data www.wolfram.com (access date 19 July, 2021); https://periodictable.com/Properties/A/UniverseAbundance.html (access date 19 July, 2021).

The use of rare and expensive metals (Dy, Nd, Sm, Co) considerably keeps down the production of the high energy magnets, which results in their shortage.

It is considered that magnets based on Sm–Co alloys are markedly more expensive than Nd–Fe–B-based magnets, because the cost of samarium should be significantly higher due to its low abundance in nature. However, despite the fact that neodymium is more abundant than samarium, the latter is currently several times less expensive, because it is formed as a by-product of the production of neodymium. Nevertheless, due to the relatively high cost of cobalt and the longer production process, magnets based on Sm–Co phases are 15% more expensive than Dy–$Nd_2Fe_{14}B$ magnets.[168] By 2018–2020, the price of neodymium stabilized at \$60–70 per kg, the price of dysprosium remained \$310 per kg, and the price of samarium reduced to \$14 US per kg. Among 3d transition metals, cobalt, which is actively used to produce lithium ion batteries, remains expensive, varying from \$40 to \$110 US per kg, with the average value being \$70 US.¶ In view of the foregoing, it is evident that the search for magnetic materials without rare earth elements is highly necessary as long as it is planned to increase the production output of devices based on these materials.

The problem of raw material shortage can be neutralized by recycling of magnets or by nuclear synthesis of the required elements, *e.g.*, in accelerators or nuclear reactors. As a method for processing of $SmCo_5$, Sm_2(Co, FeCu, Zr) or $Nd_2Fe_{14}B$ magnets, it was proposed, in particular, to use pumping-in of hydrogen gas. The mechanical stress caused by the volume expansion of hydrogenated phases results in cracking and desctruction of the material.[168] The reduction diffusion process can also be promising. Using this method, Nd–Fe–B alloys were converted to a recycled sintered magnetic material with a coercivity of 1162 kA m^{-1} (14.6 kOe) and $(BH)_{max}$ = 276 kJ m^{-3} (34.7 MG Oe).[169] Dissolution of the polymer matrix in ionic liquids was proposed for the recycling of magnetic plastics based on compounds of the Nd–Fe–B system.[170, 171] However, the recycling processes are far from being perfect and are accompanied by the loss of at best 30 mass % of neodymium and other rare earth metals, which, moreover, can be additionally oxidized during the subsequent manufacture of magnets from the recovered material. The methods used for recycling of magnetic materials were considered in detail.[172]

4. Ordered alloys with tetragonal $L1_0$ structure

The bimetallic phases with ordered $L1_0$ type structure, which include in particular FePt, FePd, CoPt, MnAl and MnGa alloys, form a class of intermetallics with high magnetocrystalline anisotropy.[173–175] This Section addresses the first three of the listed alloys, while manganese-based materials are discussed in a separate part.

The characteristic constants K_1 for FePt, FePd and CoPt are of the order of 10^6–10^7 J m^{-3} (10^7–10^8 erg cm^{-3}) (Table 1). Generally, in the set of magnetic characteristics [M_s, H_a and $(BH)_{max}$], these alloys are similar to rare earth metal magnetic compounds, but they are distinguished by high chemical stability. The major drawback of platinum- and palladium-containing alloys is the high cost of the raw materials, which rules out extensive use of large-size products, except, perhaps, for some specific applications, *e.g.*, the design of microelectromechanical systems or dentistry.[176] However, high magnetization and coercivity values of the nanoparticles and thin films made of these alloys make them promising, in particular, for high-density magnetic information recording.

Table 1. Magnetic properties of compounds with the $L1_0$ structure.[173, 175]

Alloy	K_1, 10^6 J m^{-3}	M_s, kA m^{-1}	H_a, kA m^{-1}	T_C, K	$(BH)_{max}$(theor.), kJ m^{-3}
FePd	1.8	1100	2626	760	382
FePt	6.6	1140	9230	750	406
CoPt	4.9	800	9788	840	199
MnAl	1.7	560	5490	650	95
MnGa	2.6	845	5093	650	224

The properties and preparation methods of the above-listed compounds with the $L1_0$ structure are fairly similar; therefore, we will consider them in detail in relation to the most studied Fe–Pt system. This system comprises three binary compounds with broad homogeneity regions — Fe_3Pt, FePt and $FePt_3$;[176] of these, hard magnetic properties are inherent only in FePt. Alloys with roughly the same composition can form two types of crystal structure — disordered face-centred cubic structure (A1–NaCl type, space group $Fm\bar{3}m$) and ordered tetragonal superstructure of $L1_0$ type — $CuAu^I$, space group $P4/mmm$ (Fig. 11). Transition from the disordered solid solution to the ordered one takes place at a temperature of <1300 °C for FePt and <845 °C for CoPt. During the subsequent cooling, an ordered structure can arise in $Fe_{1-x}Pt_x$ in the $0.35 < x < 0.55$ range. A decrease in the symmetry gives rise to clear-cut easy magnetization axis and high magnetocrystalline anisotropy, which is attributed to strong spin–orbit coupling of 5d electrons. Thus, pronounced hard magnetic properties are found only for compounds with ordered $L1_0$ structure. The highest degree of ordering and, correspondingly, more advantageous magnetic characteristics can be attained for the stoichiometric composition FePt.[176]

A challenge in the production of hard magnetic FePt particles is to ensure a high content of the ordered phase. The traditional metallurgical synthesis is based on the heat treatment of the disordered precursor below the transition temperature, which brings about problems of uncontrolled particle growth and sintering. When samples are obtained by quenching of the melt followed by heat treatment, large-

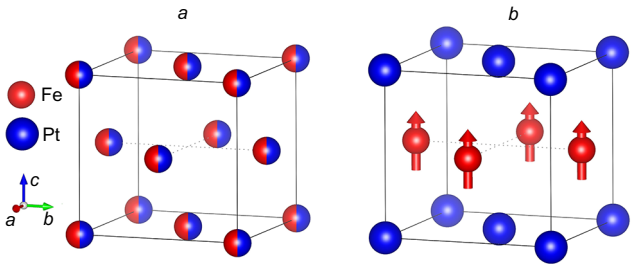


Figure 11. Schematic image of the unit cells of disordered (*a*) and ordered FePt alloys (*b*). The arrows mark the directions of the magnetic moments of ions. The figure was created by the authors using data of Ref. 176.

¶ See https://www.bgr.bund.de/DERA/DE/Publikationen/Newsletter/Preismonitor_aktuell/aktuell_node.html (access date 19 July, 2021).

grain microstructure is formed, and the coercivity in this case does not exceed 400 kA m^{-1} (5 kOe).[177] The H_c value can be increased [up to ~800 kA m^{-1} (10 kOe)] if the samples are preliminarily subjected to mechanical deformation.[178,179] Currently, chemical methods for FePt synthesis are being vigorously developed.[174,180] This gives monodisperse nanoparticles with high magnetic characteristics, which can be converted to self-assembling nanostructures and nanocomposites. Higher coercivity can be inherent in FePt thin films (10–100 nm) synthesized by direct deposition or heat treatment of the successively deposited iron and platinum layers.[181–183] This may give crystallographically oriented films possessing perpendicular magnetic anisotropy. The most spectacular examples of production of high-coercivity materials based on compounds with the $L1_0$ structure are considered below.

In the key publication devoted to the synthesis of monodisperse FePt particles, Sun[184] proposed a solution method based on thermal decomposition of iron pentacarbonyl and reduction of platinum acetylacetonate with hexadecane-1,2-diol. Both chemical reactions proceeded simultaneously in the presence of oleic acid and oleylamine at 297 °C. Dioctyl ether was used as the reaction medium. This yielded monodisperse FePt particles with sizes from 3 to 10 nm. Various modifications of this procedure are presented in a Sun's review.[174] However, the resulting particles had a FCC structure and did not possess high magnetocrystalline anisotropy. To convert this structure to $L1_0$, heat treatment at a temperature >500 °C was required, and this led to sintering and hampered the formation of monodisperse hard magnetic particles. Indeed, heat treatment of 4 nm particles at 600 °C gave ferromagnetic films with a coercivity not higher than 143 kA m^{-1} (1.8 kOe). The use of salt matrices to prevent sintering during heat treatment was proposed for solving this problem.[185,186] For this purpose, FCC FePt nanoparticles, obtained as described by Sun,[184] were mixed with NaCl and then heat-treated in a reducing atmosphere (95% Ar + 5% H_2) at 600–700 °C. Then the salt matrix was removed by being dissolved in water. As a result, FePt was almost completely converted from the disordered state to the ordered $L1_0$ phase. Non-sintered monodisperse particles with sizes from 2 to 15 nm were obtained (Fig. 12). It was noted[185,186] that the particle size and shape did not change, which makes this approach applicable for obtaining $L1_0$-FePt nanoparticles of various shapes (*e.g.*, nanorods) from the FCC phase. At room temperature, the maximum coercivity of 2390 kA m^{-1} (30 kOe) was established for particles with a diameter of 8 nm (see Fig. 12). In the case of particles <4 nm in diameter, no transition to the ordered phase was found, while 15 nm particles proved to consist of several grains. The coercivity maximum was attributed to the fact that particle growth is accompanied by increasing degree of ordering, and in the case of large particles, H_c decreases because of their polycrystallinity. The Curie temperature depends on both the particle size and the degree of ordering. For the obtained particles, they were 650 and 760 K for particles of 4 and 15 nm size, respectively.

The synthesis of textured FePt films with crystallogaphically oriented grains is of considerable interest. Ide *et al.*[187] obtained 12–25 nm-thick films by electron-beam evaporation. For this purpose, iron (1–3 Å) and platinum (3–6 Å) layers were first deposited on the MgO(100) substrate at 750 °C. Then the FePt base layer with a thickness of 7–92 nm was formed by simultaneous deposition of iron and platinum at 600 °C. After the deposition, the films were annealed at 600 °C for 10 min. During epitaxial growth, FePt(001) fina particles appeared in the films. Therefore, they had a strong magnetic anisotropy with an easy magnetization axis perpendicular to the surface. Films with a thickness of 22 nm had a coercivity of 3820 kA m^{-1} (48 kOe) upon magnetization in this direction. Conversely, films with a thickness of 46 nm proved to be magnetically soft. It was shown by electron microscopy that hard magnetic films consisted of separate particles of ~100 nm in diameter, whereas the soft magnetic films were continuous. Thus, it can be concluded that the hard magnetic state is determined by the presence of oriented single-domain FePt particles. Similar results were obtained by Shima *et al.*,[188] who produced 10 nm-thick island films with a particle diameter of 50 nm (Fig. 13) and a coercivity of 3180 kA m^{-1} (40 kOe). An increase in the thickness induced particle coalescence and decrease in the coercivity.

Okamoto *et al.*[189] found that the coercivity of FePt(001) films increased with decreasing temperature to reach 5570 kA m^{-1} (70 kOe) at 10 K. Takahashi *et al.*[181] obtained non-oriented polycrystalline FePt films with a thickness of 10–100 nm on the surface of amorphous SiO_2. Their coercivity [1830 kA m^{-1} (23 kOe) for film

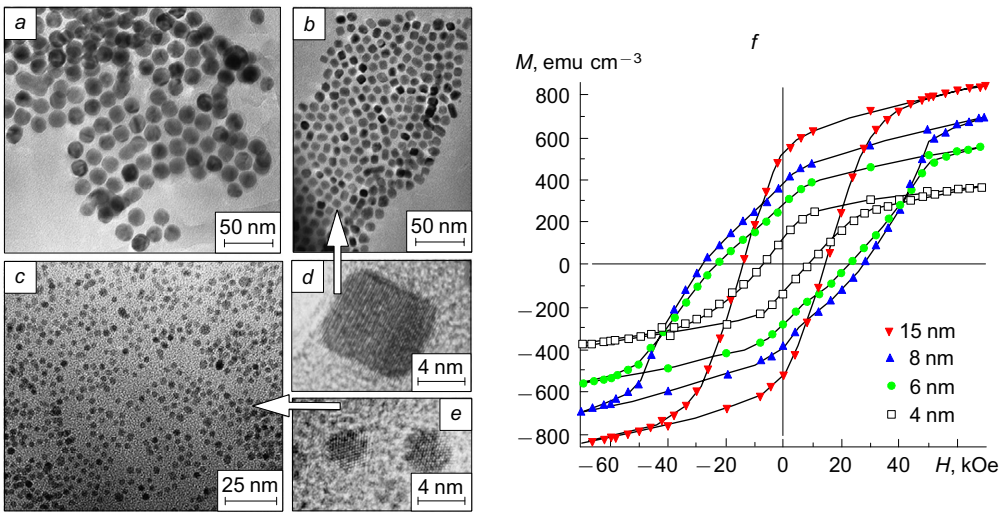


Figure 12. TEM images of FePt particles of different sizes in the NaCl matrix (*a*–*e*)[185] and magnetic hysteresis loops measured at 300 K (*f*).[186] Average particle size, nm: 15 (*a*), 8 (*b*), 4 (*c*); NaCl : FePt molar ratio: 100 : 1 (*a*), 40 : 1 (*b*), 40 : 1 (*c*). Figs *d* and *e* show high-resolution photomicrographs of the particles depicted in Figs *b* and *c*, respectively. Published with permission from IOP Publishing and Wiley.

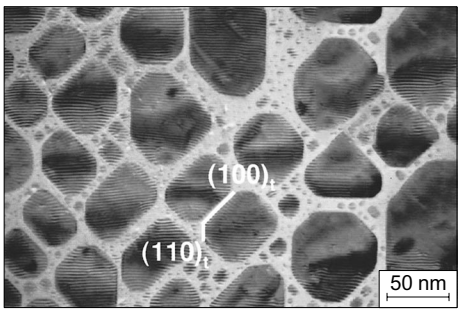


Figure 13. TEM image of the FePt island film.[188] Published with permission from AIP Publishing.

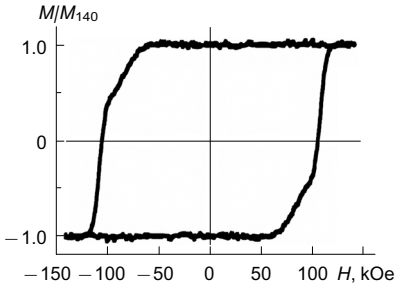


Figure 14. Magnetic hysteresis loop of the FePt epitaxial film 4.5 K.[190] M_{140} is magnetization under 140 kOe external field applied to the sample. Published with permission from AIP Publishing.

thickness of 10 nm] was lower than that of the oriented films, and did not abruptly drop after the substrate was completely coated. The authors attributed this difference to the fact that oriented films were single-crystalline, while disordered films consisted of non-oriented grains. In the former case, the main mechanism of magnetization reversal is the displacement of domain walls, while in the latter case, it is the intense pinning at grain boundaries. Generally, the coercivity decreases with increasing film thickness, because the grain size simultaneously increases and, correspondingly, grain boundaries diminish. The high coercivity of thin oriented films is attributed to their island microstructure and single-domain behaviour during magnetization reversal.

The anisotropy field for $L1_0$-FePt is $\sim$9230 kA m^{-1} (116 kOe); therefore, theoretically, the maximum coercivity for crystallographically ordered particles of this compound should be equal to this value, while that for disordered particles should be half this value. These H_c can be attained only in the ideal case where magnetization reversal of an ensemble of single-domain particles of the optimal size occurs by the coherent spin rotation mechanism. Shima *et al.*[190] made an attempt to form a microstructure as close as possible to the ideal one. They obtained a series of samples of oriented island films on the MgO(100) surface with different FePt particle size by deposition at 780 °C. The authors noted that an increase in the sputtering temperature above the temperatures used in previous studies resulted in the formation of virtually defect-free $L1_0$ phase. As the nominal film thickness increased, the island diameter increased from 5 to 200 nm. The islands of 30 nm in diameter had the highest coercivity of 5570 kA m^{-1} (70 kOe) upon magnetization along the easy axis. Then they started to coalesce, and at a diameter of 70 nm, percolation of the film microstructure and, as expected, a sharp decrease in H_c took place. The obtained coercivity was almost twice higher than the known values, but lower than the theoretically possible value. One possible reason for the decrease in coercivity is high demagnetizing field of FePt lamellae. The maximum $(BH)_{max}$ value was 398 kJ m^{-3} (50 MG Oe), which is close to the theoretical limit. On cooling the best sample, the coercivity increased to 8356 kA m^{-1} (105 kOe) at 4.5 K (Fig. 14). The authors attributed this to the suppression of thermal fluctuations of spins and increase in K_1.

Further optimization of the magnetic properties of FePt films was carried out by Son *et al.*,[191] who varied the conditions of film deposition (magnetron sputtering) and heat treatment. It was noted that the traditionally used MgO(100) substrates are characterized by $\sim$8% mismatch of crystal lattice parameters; therefore, it was proposed to deposit FePt on $(LaAlO_3)_{0.3}-(Sr_2AlTaO_6)_{0.7}$(100) substrates for which the mismatch was only 0.5%. The use of such substrates resulted in the formation of the ordered $L1_0$-FePt phase directly during deposition, which indicates that no subsequent film annealing is required, as in the case of MgO substrates. Some of the samples had the highest saturation magnetizations attained for FePt [1377 kA m^{-1} (1377 emu cm^{-3})], high coercivity [5173 kA m^{-1} (65 kOe)] and simultaneously high squareness ratio of the hysteresis loop. The highest $(BH)_{max}$ was 630 kJ m^{-3} (79 MG Oe), which is the absolute record and is 30% higher than the values known for supermagnets based on alloys of the Nd–Fe–B system. The authors attributed these magnetic characteristics to the high degree of ordering of the $L1_0$-FePt phase, achieved owing to the appropriate choice of the deposition temperature (800 °C). It was also shown that deposition of a 3 nm-thick gold layer on the FePt film leads to a considerable increase in the magnetization. This may be due to the fact that the formation of FeAu on the surface of FePt grains promotes additional ordering of the $L1_0$ phase;[192] furthermore, the FeAu alloy itself has a higher magnetization. The use of magnetron sputtering makes it possible to scale-up the production of FePt nanoparticles, which can be separated from the substrate physically or chemically and used to manufacture high-energy magnets, necessary, for example, for miniature electric motors or electric generators. Chemically stable FePt nanoparticles could also find use in medicine (as contrast agents for magnetic resonance imaging and hyperthermia and for targeted drug delivery).

The same trends and approaches as for FePt alloys also hold for CoPt alloys, but the practically observed H_c values are much lower. This is due to the difficulty of preparing homogeneous solid solutions containing cobalt and platinum in 1 : 1 ratio.[193] Large deviations from the required composition lead to stabilization of CoPt in the FCC state and also give rise to impurities of other phases (*e.g.*, Co_3Pt) possessing markedly lower magnetocrystalline anisotropy. The coercivity of films and nanoparticles usually does not exceed 800–1200 kA m^{-1} (10–15 kOe) at room temperature.[183,193–196] However, in principle, it is possible to obtain films with a high-quality structure. For example, Rakshit *et al.*[197] used pulsed laser deposition to grow epitaxial films of $L1_0$-CoPt with a coercivity of 2387 kA m^{-1} (30 kOe). The authors used the $SrTiO_3$(001) substrate, since MgO substrates normally used for FePt deposition have a crystal lattice mismatch of 9.6% relative to the CoPt lattice. The deposition was conducted at 800 °C and was followed by annealing for 25 min. Like in the case of FePt, high coercivity is determined by film morphology, formed by oriented single-domain islands.

5. High-coercivity alloys based on manganese

An example of ferromagnetic alloy with the $L1_0$ structure is τ-MnAl.[198] This compound is markedly cheaper than FePt and, theoretically, it can have an anisotropy field of ~5490 kA m^{-1} (~70 kOe). However, in practice, the attained H_c values were not higher than 400 kA m^{-1} (5 kOe).[199–201] The key problem is the metastability of the τ-MnAl phase and related difficulties of the synthesis and control of the microstructure. The stability of this phase can be enhanced by doping with carbon, but this would decrease the field of anisotropy. Nevertheless, τ-MnAl could become a fairly promising alloy for the manufacture of high-coercivity magnets, if the problems of its synthesis are solved, for example, by finding other stabilizing elements.

The $L1_0$-MnGa alloy also has a high uniaxial magnetic anisotropy; the theoretically limiting parameters characterizing its magnetic properties are as follows: H_c = 5090 kA m^{-1} (64 kOe), M_s = 845 kA m^{-1} (845 emu cm^{-3}) and $K_1 = 2.6 \times 10^6$ J m^{-3} (2.6×10^7 erg cm^{-3}). Zhu *et al.*[175] grew the epitaxial $L1_0$-$Mn_{1.5}Ga$ films on GaAs(001) substrate by molecular beam epitaxy at temperatures of 100–300 °C. The dependences of the magnetic properties on the deposition temperature (T_s) are depicted in Fig. 15. It can be seen that the samples have high magnetic anisotropy and square hysteresis loops when the field is applied perpendicular to the film surface. The coercivity is maximum when the deposition temperature is 100 °C and amounts to 3406 kA m^{-1} (42.8 kOe). When this temperature increases, the coercivity decreases and the saturation magnetization increases. The lower magnetization was explained by the fact that the spins of excess manganese atoms located in the gallium positions are antiparallel to other spins. It was also noted that the obtained films were continuous; therefore, the mechanism of giant coercivity should differ from the mechanism observed in the island FePt films, in which isolated nanosized grains behave as single-domain particles in the magnetization reversal. The continuous structure of the film can be important for the manufacture of magnetic electrodes. The $(BH)_{max}$ value reaches 21 kJ m^{-3} (2.6 MG Oe) for deposition temperature of 300 °C.

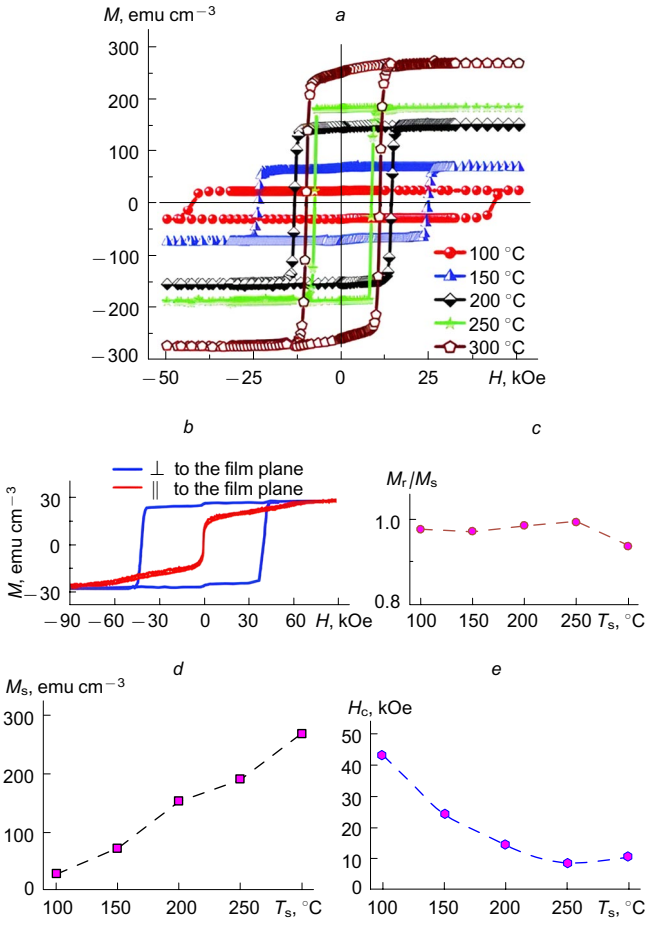


Figure 15. Field dependences of magnetization for the $L1_0$-$Mn_{1.5}Ga$ films at various temperatures (*a*) and various directions of magnetization (*b*) and dependences of M_s and coercivity H_c on the deposition temperature (*c*–*e*).[175] M_r/M_s is the ratio of the remanent magnetization to the saturation magnetization; the temperature of measurements is 300 K. Published with permission from Wiley.

As the manganese content increases, $Mn_{1-x}Ga_x$ alloys can crystallize as the tetragonal $D0_{22}$-Mn_3Ga phase (space group *I*4/*mmm*, Al_3Ti structural type), which also has a high magnetocrystalline anisotropy. Nummy *et al.*[202] obtained 20 nm-thick $Mn_{2.7}Ga$ films on two different substrates, Si and GaAs, using molecular beam epitaxy. In the former case, the film consisted of non-oriented grains of 50–100 nm in diameter and had coercivity of 1990 kA m^{-1} (25 kOe). The high coercivity was due to the single-domain behaviour of grains of the $D0_{22}$-Mn_3Ga phase. Similar results were obtained[203, 204] for the films produced by magnetron sputtering on Si–SiO_2 substrates. An epitaxial film with a coercivity of 286 kA m^{-1} (3.6 kOe) was formed on the GaAs substrate.

It was noted[205] that the manufacture of magnets requires the high-coercivity $D0_{22}$-Mn_3Ga phase as a bulk material. The authors obtained the $Mn_{65}Ga_{20}Cu_{15}$ alloy by fast quenching of the melt. After annealing at 300 °C for 10 h, the sample acquired a coercivity of 1894 kA m^{-1} (23.8 kOe), with the saturation magnetization being 3.5 A m^2 kg^{-1} (3.5 emu g^{-1}). High coercivity is a consequence of the small size of $D0_{22}$-Mn_3Ga grains (40–60 nm), which are formed in the material on heat treatment.

The low-temperature MnBi phase has a NiAs type crystal structure (Fig. 16). This layered structure in combination with the strong spin–orbit coupling of bismuth 5d electrons provides for high anisotropy field of this compound and $K_1 \approx 1.5 \times 10^6$ J m^{-3} (1.5×10^7 erg cm^{-3}) at room temperature.[206] The saturation magnetization is ~80 A m^2 kg^{-1} (~80 emu g^{-1}) and $(BH)_{max}$(theor.) is 143 kJ m^{-3} (18 MG Oe). An interesting feature of the MnBi alloy is the fact that its coercivity increases with temperature rise. At 10 K, MnBi is spontaneously magne-

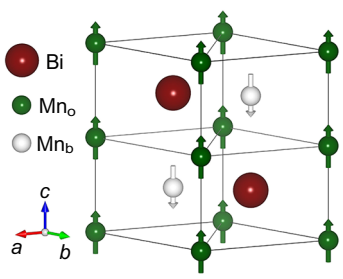


Figure 16. Crystal structure of the low-temperature MnBi phase. In the ideal case, the manganese ions are located only in the octahedral sites (Mn_o), but they can also enter bipyramidal voids (Mn_b). The arrows indicate the direction of the magnetic moments of ions. The figure was created by the authors using data of Ref. 198.

tized along the crystal structure layers, which are easy magnetization planes. However, above 90 K, the magnetization vector is directed along the *c* axis[207] and the magnetocrystalline anisotropy becomes uniaxial. The constant K_1 increases with temperature rise and passes through a maximum of 2.2×10^6 J m^{-3} (2.2×10^7 erg cm^{-3}) at 220 °C. At 355 °C, peritectic decomposition takes place to give the high-temperature $Mn_{1.08}Bi$ phase and Bi.[208] The problems of synthesis of MnBi-based materials with a controlled microstructure are associated, apart from decomposition, with low melting point of bismuth and high volatility of both manganese and bismuth.

Most methods used to synthesize the low-temperature MnBi phase are based on fast quenching of a melt followed by annealing at temperatures below 340 °C. Nearly single-phase samples were obtained and studied for the first time by Guo *et al.*[209] For this purpose, a MnBi melt was rapidly quenched and annealed at 300 °C to form the low-temperature phase. At room temperature, the anisotropy field is 3980 kA m^{-1} (50 kOe), while at 530 K, it passes through a maximum of 7160 kA m^{-1} (90 kOe). The coercivity is 160 kA m^{-1} (2 kOe) at room temperature and 1430 kA m^{-1} (18 kOe) at 500 K. The H_c values are adequately described by the model of domain wall pinning, that is, the MnBi particles are not single-domain.

Yang *et al.*[210] reported grinding of MnBi ribbons and magnetic field alignment of the resulting particles in epoxy resin. The saturation magnetization of the starting material was 75 A m^2 kg^{-1} (75 emu g^{-1}) and the grain size was 20–30 nm. This is smaller than the single-domain limit, which is 250 nm; therefore, the main mechanism of magnetization reversal is the coherent spin rotation. As a consequence, the coercivity was 875 kA m^{-1} (11 kOe) at room temperature and reached 1989 kA m^{-1} (25 kOe) at 540 K; $(BH)_{max}$ = 56.5 kJ m^{-3} (7.1 MG Oe) at room temperature.

Since MnBi undergoes peritectic decomposition, the manufacture of magnets by powder sintering is complicated. It was proposed[211] to produce a bulk anisotropic MnBi magnet by low-energy milling in a ball mill followed by hot pressing in a magnetic field. The authors noted that milling gave anisotropic powder particles, which were easily aligned in a magnetic field. The following magnetic characteristics were found for the oriented powder at room temperature: H_c = 955 kA m^{-1} (12 kOe), $M_s = M_r$ = 58.5 A m^2 kg^{-1} (58.5 emu g^{-1}) and $(BH)_{max}$ = 71.6 kJ m^{-3} (9 MG Oe), which is the record-high value for this compound. After hot pressing at 320 °C, the density of the anisotropic magnet was 98% of the crystallographic density, H_c = 517 kA m^{-1} (6.5 kOe), M_r = 45.5 A m^2 kg^{-1} (45.5 emu g^{-1}), M_s = 50 A m^2 kg^{-1} (50 emu g^{-1}), $(BH)_{max}$ = 46.2 kJ m^{-3} (5.8 MG Oe) at room temperature. As the magnet was heated to 530 K, the coercivity increased to 2250 kA m^{-1} (28.3 kOe) and $(BH)_{max}$ decreased to 28.6 kJ m^{-3} (3.6 MG Oe) because of a decrease in the magnetization (Fig. 17). The influence of the milling intensity and duration was studied in detail.[212] The optimization of conditions and magnetic alignment gave powders with a coercivity of 1290 kA m^{-1} (16.2 kOe) at room temperature. Rama Rao *et al.*[213] proposed cryomilling for efficient disintegration of the low-temperature MnBi phase. It was shown that cooling down to 90 K during milling helps to avoid partial decomposition of this phase and increases the phase fragility, which shortens the milling time. Non-oriented magnetic powders with a grain size of 35 nm had H_c = 1647 kA m^{-1} (20.7 kOe), M_s = 29 A m^2 kg^{-1}

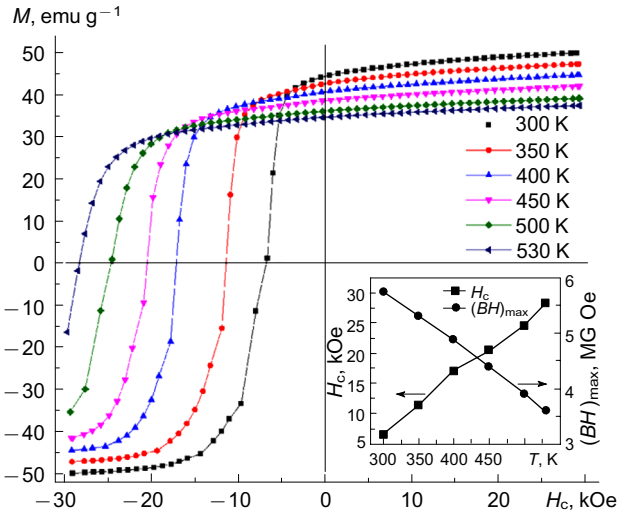


Figure 17. Demagnetization curves for pressed MnBi magnets at various temperatures. The inset shows the temperature dependences of H_c and $(BH)_{max}$.[211] Published with permission from IOP Publishing.

(29 emu g^{-1}) and M_r = 18 A m^2 kg^{-1} (18 emu g^{-1}). Powder compaction by hot pressing to a density of 97% produced an isotropic magnet with a coercivity of 1027 kA m^{-1} (12.9 kOe) at room temperature and 2387 kA m^{-1} (30 kOe) at 450 K.

Zhou *et al.*[214] prepared MnBi films by pulsed laser deposition. First, bismuth and manganese layers were applied on a glass substrate, then the samples were annealed at 300–600 °C, and after that, a protective gold layer was deposited on the film surface. By optimizing these processes, the authors were able to fabricate crystallographically textured MnBi films with 40–50 nm grains. When a magnetic field was applied perpendicular to the film surface, the coercivities were 1194 kA m^{-1} (15 kOe) and 1870 kA m^{-1} (23.5 kOe) at 300 and 373 K, respectively. The magnetic properties of MnBi can also be modified by doping. For example, oriented MnBi films doped with praseodymium were obtained.[215] The addition of praseodymium resulted in a decrease in the magnetization, but caused an increase in the coercivity, which was 1830 kA m^{-1} (23 kOe) at room temperature when the lanthanide content was 9 at.%.

Thus, the low-temperature MnBi phase is promising for the manufacture of permanent magnets containing no rare earth or noble metals. The coercivity values inherent in MnBi at room temperature are moderate; however, H_c considerably increases with temperature rise, which is necessary for some high-temperature applications. It should also be noted that the limiting theoretical characteristics of the low-temperature MnBi phase have not yet been attained.

6. Hard magnetic ferrites

Metal compounds that exhibit exceptionally high hard magnetic characteristics were considered above. Ferrites, ferrimagnetic compounds based on iron(III) oxide, are one more class of important industrial magnetic materials, which surpass rare earth metal-based magnets in the production output, and have moderate magnetizations. However, among ferrites, there are also compounds with high

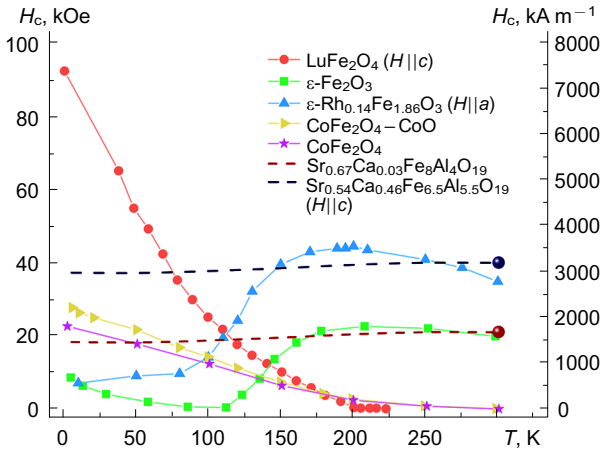


Figure 18. Temperature dependences of H_c for $LuFe_2O_4$ (single crystal), ε-Fe_2O_3 (powder), oriented ε-$Rh_{0.14}Fe_{1.86}O_3$ particles, $CoFe_2O_4$ – CoO (powder), $CoFe_2O_4$ (powder), $Sr_{0.67}Ca_{0.33}Fe_8Al_4O_{19}$ (powder) and $Sr_{0.54}Ca_{0.46}Fe_{6.5}Al_{5.5}O_{19}$. The dashed lines correspond to the prediction based on $H_c(T)$ dependences for $SrFe_{12}O_{19}$; the dark-red and dark-blue points are experimental results. The figure was created by the authors using published data.[218–223]

magnetocrystalline anisotropy, which accounts for giant coercivity values over a broad temperature range (Fig. 18). In addition, the interest in hard magnetic ferrites is caused by specific absorption of radiation of millimetre wavelength range due to the ferromagnetic resonance phenomenon.[216] The frequency of natural (*i.e.*, without applied external magnetic field) ferromagnetic resonance (f_r), like the coercivity, is determined by the anisotropy field

$$f_r = \frac{\gamma}{2\pi} H_a = \gamma \frac{2K_1}{\mu_0 M_s} \qquad (11)$$

where γ is the gyromagnetic ratio

$$\gamma = \frac{g}{\mu_B h} \qquad (12)$$

g is the g-factor of the paramagnetic ion, h is the Planck constant.[217] For ferrites, $g \approx 2$ (because the orbital moment of 3d ions in solids is frozen) and $\gamma \approx 28$ GHz T^{-1} (2.8 MHz G^{-1}), with H_a being 80–8000 kA m^{-1} (1–100 kOe). Therefore, the natural ferromagnetic resonance frequencies are in the range of 1–250 GHz. The currently known hard magnetic ferrites with giant coercivity — lutetium and cobalt ferrites, ε-Fe_2O_3 and aluminum-doped M-type hexaferrites — are considered below.

6.1. Lutetium ferrite

The ferrite $LuFe_2O_4$ belongs to the type of mixed oxides $LnFe_2O_4$ (Ln = Ho, Er, Tm, Yb, Lu, Y) and has a hexagonal crystal structure (space group $R\bar{3}m$, unit cell parameters: $a = 3.429$, $c = 25.25$ Å).[224] In the $LuFe_2O_4$ structure, the iron atoms occur at the centres of trigonal bipyramids that share edges and are thus connected into double layers of iron atoms, with a layer of Lu^{3+} ions being located between them (Fig. 19). In each double layer, one sublayer is enriched with Fe^{2+} ions and the other one is enriched with Fe^{3+} (Ref. 225). Lutetium ions are diamagnetic and are not involved in the formation of magnetic properties of the material. The iron cations are in the +2.5 oxidation state, and below the Néel temperature (~220–230 K), their magnetic moments are ferromagnetically ordered along the c axis (see Fig. 19 *b*).[224] The presence of Fe^{2+} in the structure gives rise to a high orbital magnetic moment (~0.8 μ_B per formula unit), which is responsible for the high uniaxial magnetocrystalline anisotropy of the material.[225] Due to the significant magnetocrystalline anisotropy, very high coercivities were detected for $LuFe_2O_4$ single crystals: 7162 kA m^{-1} (90 kOe)[218] and 8754 kA m^{-1} (110 kOe)[224] at 4 K. This material starts to exhibit giant $H_c > 1592$ kA m^{-1} (20 kOe) even at 110 K (see Fig. 18).[218] The collective freezing of ferrimagnetic domains with high uniaxial magnetocrystalline anisotropy at temperature < 80 K was indicated as the second cause for this high coercivity of the $LuFe_2O_4$ single crystal.[218] Apart from very high hard magnetic properties, the saturation magnetization of $LuFe_2O_4$ is also significant: 2.8 μ_B per formula unit at low temperature,[218,224] which corresponds to ~45 A m^2 kg^{-1} (45 emu g^{-1}).

The relevant publications are most often devoted to lutetium ferrite as a single crystal[218,224,226–228] or ceramics.[229,230] Owing to remarkable ferroelectric properties of $LuFe_2O_4$, the number of publications dealing with thin films based on this compound has increased in recent years.[231–233] However, no data on the synthesis of single-domain particles of lutetium ferrite were reported. Polycrystalline samples are prepared by solid-phase sintering of Lu_2O_3 and Fe_2O_3 powders at 1200 °C in a reducing medium, for example, in a $CO_2 + H_2$ mixture,[226] or in an inert atmosphere,[230] or in a moderate vacuum (~1 Pa).[229] Qin *et al.*[229] demonstrated the possibility of obtaining $LuFe_2O_4$ ceramics by spark plasma sintering. The single crystalline $LuFe_2O_4$ samples are obtained, most often, by zone melting. First, polycrystalline lutetium ferrite is prepared as a bar by the procedure described above. Then gradual local melting and crystallization of the material in the reducing $CO + CO_2$ atmosphere is performed along the sample. It was noted[226,227] that the oxygen stoichiometry, average oxidation state of iron and, hence, the magnetic properties of lutetium ferrite considerably depend on the medium in which the crystal is grown; therefore, parameters of the gas mixture should be thoroughly optimized.

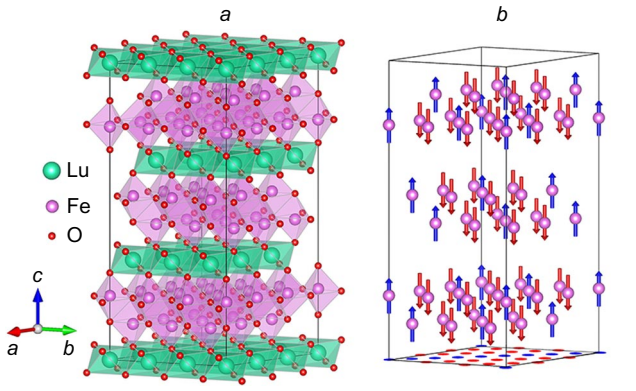


Figure 19. Crystal (*a*) and magnetic (*b*) structures of the ferrite $LuFe_2O_4$. The arrows mark the directions of the magnetic moments of ions. The figure was created by the authors using published data.[224,225]

6.2. Cobalt ferrite

The ferrite $CoFe_2O_4$ has an inverse spinel structure (space group $Fd\bar{3}m$, lattice parameter $a = 8.38$ Å).[3] In the first approximation, the Fe^{3+} ions in $CoFe_2O_4$ occupy all tetrahedral and half of octahedral sites and Co^{2+} ions occupy half of octahedral sites (Fig. 20).[3,234] However, cobalt atoms are often distributed over both sublattices.[222,235,236] This compound is a ferrimagnet with Néel temperature of ~800 K.[3] The magnetic moment of the iron ion in the tetrahedral sublattice is antiparallel to the magnetic moments of ions in the octahedral sites (see Fig. 20) and to the overall magnetic moment of the unit cell. At 0 K, the effective magnetic moment on the iron atom is 5 μ_B, while that on the cobalt atom is 2–3 μ_B; hence, the moment is ~3 μ_B per $CoFe_2O_4$ formula unit.[3] Among hard magnetic ferrites, cobalt ferrite has a maximum saturation magnetization: approximately 80 A m^2 kg^{-1} (80 emu g^{-1}) at room temperature.[3] The coercivity of single-domain particles of this material at room temperature can exceed 716 kA m^{-1} (9 kOe),[237] while that of thin films is 875 kA m^{-1} (11 kOe).[238] However, most often, $CoFe_2O_4$ powders have more moderate H_c values, below 430 kA m^{-1} (5.4 kOe), depending on the particle morphology and cobalt to iron ratio.[221,222,239–247] It was shown experimentally[241,248,249] that the critical diameter of the magnetic domain for $CoFe_2O_4$ is ~40 nm, whereas according to theoretical calculations it should be ~100 nm.[250] The superparamagnetic limit of cobalt ferrite is attained when the crystallite size is ~10 nm.[222,241,250–252] One feature of this material is that the coercivity of its nanoparticles substantially increases on cooling and, in the temperature range of 2–50 K, it can reach very high values: above 1592 kA m^{-1} (>20 kOe).[222,240,242,244] This is caused by the increase in the effective magnetic anisotropy constant (K_{eff}) of the material.[222,241,242,253,254]

In this case, by effective magnetic anisotropy constant is meant the additive contribution of the volume anisotropy (K_v) and particle surface anisotropy (K_s). In the case of spherical particles with the diameter d

$$K_{eff} = K_v + \frac{6K_s}{d} \quad (13)$$

The K_s value can be either above or below zero. The surface anisotropy, which makes a considerable contribution to the magnetic properties of nanoparticles and thin films, arises because of the fact that surface atoms are surrounded by less neighbours, located at different distances from one another, than bulk atoms, thus giving rise to a local disruption of symmetry of the magnetic structure and, hence, changing the magnetic properties.[37]

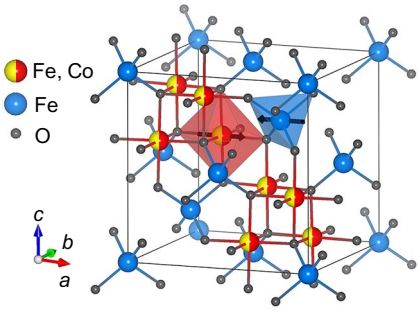


Figure 20. Crystal structure of ferrite $CoFe_2O_4$. The figure was created by the authors using data of Ref. 3.

Cobalt ferrite has a cubic magnetocrystalline anisotropy with easy magnetization directions parallel to ⟨100⟩ crystallographic axes. At room temperature, its magnetocrystalline anisotropy constant is of the order of magnitude of 10^5 J m^{-3} (10^6 erg cm^{-3}).[3] The magnetocrystalline anisotropy of $CoFe_2O_4$ is caused by strong spin–orbit coupling, resulting from the non-zero orbital moment of the Co^{2+} ion in the octahedral sublattice.[253,254] However, in the case of particles with sizes of a few nanometres, the hard magnetic properties of cobalt ferrite in the low-temperature region are determined, to a higher extent, by the surface magnetic anisotropy. It was shown[251] that cobalt ferrite particles of 5–13 nm in size with the same volume and chemical composition, but different morphology (spherical and cubic) have substantially different coercivities. This can be attributed to the fact that metal ions located on the surface of spherical particles have fewer neighbours and have lower coordination symmetry than the ions located in the particle bulk,[251] which is favourable for the appearance of surface anisotropy. Also, it was ascertained that the surface anisotropy constant is approximately 1.5 times higher for the spherical particles of maghemite (γ-Fe_2O_3) than for cubic particles.[255]

Due to the cubic magnetocrystalline anisotropy of cobalt ferrite, the ratio of the remanent magnetization to the saturation magnetization (M_r/M_s) is higher for single-domain particles than for particles with uniaxial magnetocrystalline anisotropy and can reach 0.8.[242,256] However, at temperatures close to room temperature, the M_r/M_s ratio is usually <0.5 and increases with cooling to reach the maximum value at a temperature <10 K.[222,241,242]

The magnetic properties of cobalt ferrite are affected by factors determined by the nature of the material (Co/Fe ratio and particle morphology) and temperature. It was shown experimentally[3,222,235,241] that the optimal content of cobalt in $Co_xFe_{3-x}O_4$ is $x \approx 0.6$. In this case, the maximum constants of magnetic anisotropy at various temperatures and various particle sizes were as follows: $\sim 2 \times 10^5$ J m^{-3} (2×10^6 erg cm^{-3}) at 300 K and $\sim 12 \times 10^5$ J m^{-3} (12×10^6 erg cm^{-3}) at 5 K ($d = 20$ nm);[241] and $\sim 13 \times 10^5$ J m^{-3} (13×10^6 erg cm^{-3}) at 2 K ($d = 13$ nm) (Fig. 21).[222] The maximum magnetocrystalline anisotropy constant of cobalt ferrite at $x \approx 0.6$ was confirmed by theoretical calculations.[253] The coercivity of cobalt ferrite depends on the cobalt content and passes through a maximum also at $x \approx 0.6$ (see Fig. 21).[222]

A study of the effect of the cobalt ferrite particle size on the magnetic characteristics demonstrated that the effective magnetic anisotropy constant and coercivity depend non-monotonically on the size of crystallites (see Fig. 21). According to Dehsari and Asadi,[222] the maximum values of H_c = 1750 kA m^{-1} (22 kOe) and K_{eff} at 2 K are attained when the particle size is ~12 nm, whereas López-Ortega *et al.*[241] reported the maximum magnetic hardness for the sample with 20 nm crystallites [$H_c \approx 1353$ kA m^{-1} (17 kOe) at 5 K]. In view of the fact that the coercivity of $CoFe_2O_4$ is sensitive to both the particle volume and shape, which are difficult to change independently, it is difficult to study the effect of particle shape on the coercivity of cobalt ferrite. Theoretically, due to the high magnetization of the material, an enhanced magnetic hardness should be expected for rod-like particles, with the rod being directed along the ⟨100⟩ axis. Together with the shape factor, an important role is also played by features of the particle

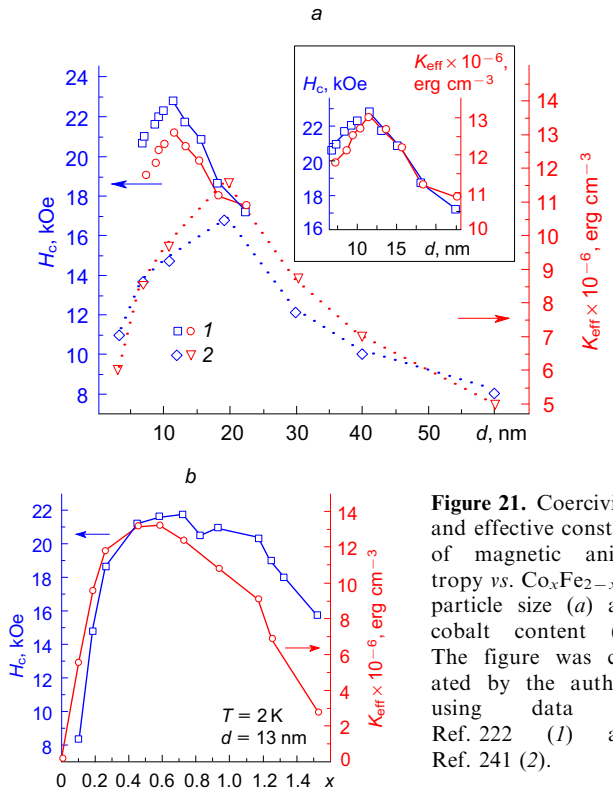


Figure 21. Coercivity and effective constant of magnetic anisotropy *vs.* $Co_xFe_{2-x}O_4$ particle size (*a*) and cobalt content (*b*). The figure was created by the authors using data of Ref. 222 (*1*) and Ref. 241 (*2*).

surface (see above: difference between the magnetic properties of spherical and cubic $CoFe_2O_4$ particles).

The temperature dependence of the magnetic properties of cobalt ferrite has been investigated.[222, 241, 242] It was shown that lowering the temperature from 300 K to 2–5 K brings about a monotonic increase in the coercivity and the magnetic anisotropy, with giant values [> 1592 kA m^{-1} (20 kOe)] being attained only for particles of ~14 nm size. By now, the highest cobalt ferrite coercivity of 1910 kA m^{-1} (24 kOe) was attained at the following parameters: x = 0.6, particle size of 13 nm, temperature of 2 K.[242]

There are three key approaches to increasing the coercivity of cobalt ferrite. The first one is to generate the exchange-coupled ferrimagnet–antiferromagnet magnetic composite based on $CoFe_2O_4$–CoO nanoparticles.[221] At 5 K, this material has a very high coercivity equal to 2228 kA m^{-1} (28 kOe), whereas cobalt ferrite particles without the antiferromagnetic component have H_c of only 1432 kA m^{-1} (18 kOe) at this temperature. In addition, the coercivity of the composite material is significantly higher also at higher temperatures. Indeed, $CoFe_2O_4$–CoO outstrips the H_c value of 1592 kA m^{-1} (20 kOe) even on cooling to 50 K. However, in the vicinity of room temperature, the coercivity of this material becomes < 80 kA m^{-1} (< 1 kOe) (see Fig. 18). Tancredi *et al.*[257] showed that the alignment of $Co_{0.5}Fe_{2.5}O_4$ particles with a 16 nm size in an external magnetic field increases the coercivity by 45%, that is, from 1671 kA m^{-1} (21 kOe) to 2387 kA m^{-1} (30 kOe) at 5 K. The preparation of the oriented sample started with the synthesis of cobalt ferrite nanoparticles by thermal decomposition of cobalt and iron oleates in a solution of octadecene and oleic acid. Then the resulting nanoparticles were washed and dispersed in octadecene. The resulting suspension was placed into a SQUID magnetometer and cooled down in a magnetic field with a strength of 4775 kA m^{-1} (60 kOe) below the octadecene melting point in order to prevent the Brownian relaxation of particles during magnetization reversal. The established coercivity of 2387 kA m^{-1} (30 kOe) is the highest value known for cobalt ferrite from the literature.

Surface features make a great contribution to the magnetic properties of cobalt ferrite; therefore, there are approaches to increase the magnetic hardness of this material by modifying the particle surface. It was shown[237] that cobalt ferrite particles of 20 nm in size coated by oleic acid have a coercivity of ~756 kA m^{-1} (9.5 kOe), which increases with increasing oleic acid concentration.

Doping of cobalt ferrite with ions of other metals is, most often, less efficient for increasing the magnetic hardness. For example, the diamagnetic dilution of cobalt ferrite with aluminium atoms decreases the magnetization of the material, but no increase in the coercivity takes place.[239, 258] Dipesh *et al.*[239] noted that this behaviour may be associated with a strong decrease in the magnetocrystalline anisotropy constant. When a gallium cation is incorporated in the cobalt ferrite structure, the saturation magnetization increases and the coercivity decreases.[259, 260] Doping of $CoFe_2O_4$ with In^{3+} induces an increase in the material coercivity, while the saturation magnetization decreases.[261, 262] The different effects of diamagnetic dilution of cobalt ferrite with aluminium, gallium and indium are attributable to positioning of the diamagnetic cations in different paramagnetic ion sites and to the simultaneous redistribution of Fe^{3+} and Co^{2+} cations between the sublattices.[239, 259–263] The insertion of paramagnetic ions such as Ni^{2+}, Mn^{2+} and Y^{3+} or diamagnetic ions such as Zn^{2+} and Ti^{4+} does not increase the magnetic hardness of cobalt ferrite.[264]

Sharifianjazi *et al.*[264] observed an increase in the coercivity of cobalt ferrite upon the insertion of In^{3+}, Nd^{3+}, Gd^{3+}, Mg^{2+}, Cu^{2+}, Cd^{2+} and Cr^{3+} ions. However, it should be borne in mind that the addition of a dopant results, most often, in a change in the particle size, and this may affect the magnetic properties of the material. To our knowledge, no data on the influence of dopants on the magnetic hardness of cobalt ferrite with invariable particle morphology was reported in the literature, and this is still an open question. A change in the chemical composition of cobalt ferrite may lead to complete or partial transfer of the material particles to the superparamagnetic region; in this case, the magnetic hardness should sharply decrease. In view of this fact, study of the magnetic properties of substituted cobalt ferrite at low temperatures may be promising.

For the preparation of cobalt ferrite with the highest coercivity, it is necessary that the requirements imposed on the ratio of cobalt and iron and the particle size (see above) should be met. Therefore, the possibility of controlling at least two of these parameters must be envisaged in the synthesis. In addition, to attain the highest magnetic properties, it is desirable to obtain single (non-aggregated) particles of high crystal quality with a narrow size distribution. The first successful attempt to obtain cobalt ferrite nanoparticles with giant coercivity was reported by Hutlova *et al.*[244] The authors proposed a method for growing $CoFe_2O_4$ crystallites in a refractory silica matrix. First, an aqueous solution of cobalt(II) and iron(III) nitrates in 1 : 2 molar ratio was prepared. Then a solution containing tetraethoxysilane (TEOS), methanol and formamide was

added. After complete hydrolysis of tetraethoxysilane, the gel was dried. The resulting xerogel was slowly heated to 1000 °C and kept for 2 h to obtain the target phase. Powder X-ray diffraction and transmission electron microscopy studies showed that the cobalt ferrite particles in the sample have a size of ~10–12 nm. According to magnetic measurements, cooling of this material leads to a coercivity increase from 80 kA m^{-1} (1 kOe) at 300 K to 1592 kA m^{-1} (20 kOe) at 2 K.

Methods for the synthesis of metal oxides by decomposition of organometallic precursors in high-boiling solvents gained popularity in the early 2000s.[241,265] These methods make it possible to efficiently control the particle size and shape and the chemical composition of the material.[222] The main benefits of these approaches include the preparation of ensembles of single, well crystallized particles with a narrow size distribution[222,241,251,265] and the synthesis of composite nanoparticles by building-up a second phase (shell).[251,266,267] The organometallic precursors used in these methods are metal acetylacetonates,[241,251,266–268] carboxylates,[265] oleates,[257,265] *etc.*, while high-boiling solvents include dibenzyl and diphenyl ethers,[241,251,266,268] high-carbon alkanes, alkenes,[257,267] alcohols,[251] oleic acid and allylamine.[241,257,265,267,268] Parameters of the particles can be controlled by both chemical (varying of the chemical nature of components in the reaction mixture and precursor concentrations) and physical factors (change in the final temperature[241,251] and heating rate[222,241,251] and duration[241]). For example, it was shown[222] that increase in the heating rate of an acetylacetonate solution in oleic acid from 1 to 20 °C min^{-1} results in a decrease in the size of cobalt ferrite particles from 23 to 7 nm. As the surfactant content increases from 4 to 24 mmol, the particle size increases from 9 to 18 nm, while a decrease in the precursor concentration leads to a decrease in the particle size from 18 to 7 nm.[222]

Thus, cobalt ferrite is an efficient material for the creation of nanoparticle ensembles and thin films with giant coercivity below 10 K. Evidently, the question of further increase in the magnetic hardness of the material could be answered by detailed investigation of cationic substitution.

6.3. ε-Iron oxide

ε-Iron oxide(III), ε-Fe_2O_3, has an orthorhombic crystal structure (space group $Pna2_1$, unit cell parameters: $a = 5.072$, $b = 8.736$, $c = 9.418$ Å, $\alpha = \beta = \gamma = 90°$). The iron atoms in the unit cell are located in four crystallographically non-equivalent sites with a multiplicity of 4, three sites with octahedral environment (Fe_A, Fe_B, Fe_C) and one tetrahedral site (Fe_D) (Fig. 22). The magnetic structure and the type of magnetism of this oxide are still debated in the scientific community.[269] Some researchers consider ε-Fe_2O_3 to be a canted antiferromagnet; however, most often, this material is treated as a collinear ferrimagnet.[269,270] In the latter case, the magnetic structure can be described in the following way. The iron ions in the Fe_B and Fe_C sublattices have a magnetic moment co-directional with the *a* axis, whereas in the two other sublattices (Fe_A, Fe_D), the magnetic moment is directed oppositely to this axis (see Fig. 22). At room temperature, the magnetic moment of iron in the tetrahedral sublattice is much lower than in other sublattices, which gives rise to uncompensated antiferromagnetism.[269,271] According to the neutron diffraction data, the iron ion has a magnetic moment of 0.29 μ_B,

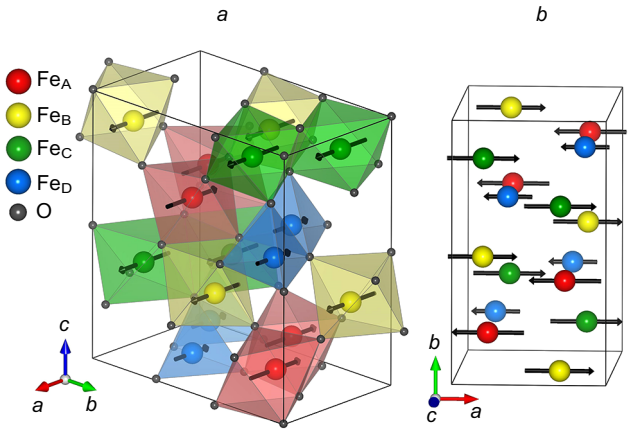


Figure 22. Crystal (*a*) and magnetic (*b*) structures of ε-Fe_2O_3. The arrows mark the directions of the magnetic moments of ions. The figure was created by the authors using data of Ref. 269.

which corresponds to the saturation magnetization $M_s = 20$ A m^2 kg^{-1} (20 emu g^{-1}).[272] The saturation magnetizations of ε-Fe_2O_3 samples determined from the results of magnetic hysteresis measurements in the maximum fields of 4775–7958 kA m^{-1} (60–100 kOe) are in the range of 15–25 A m^2 kg^{-1} (15–25 emu g^{-1}). It should be noted that these values were usually calculated using magnetic data for multiphase samples with allowance for the weight fraction of ε-Fe_2O_3; therefore, these data should be treated with caution.

The field dependences of the magnetization of the α-Fe_2O_3, γ-Fe_2O_3 and ε-Fe_2O_3 polymorphs are depicted in Fig. 23 *a*–*c*. It can be seen that ε-Fe_2O_3 has a very high coercivity [~1592 kA m^{-1} (~20 kOe)], whereas the coercivity of other polymorphs is much lower: for α-Fe_2O_3, $H_c < 477$ kA m^{-1} (6 kOe),[273–275] while for γ-Fe_2O_3, $H_c < 40$ kA m^{-1} (0.5 kOe). The surprisingly high coercivity of ε-Fe_2O_3 is attributed to three factors: relatively low saturation magnetization, high uniaxial magnetocrystalline anisotropy and the single-domain state of particles.[276]

The magnetocrystalline anisotropy constant of ε-Fe_2O_3 is much higher than those of other iron oxide polymorphs:[276,277]

Oxide	α-Fe_2O_3	γ-Fe_2O_3	ε-Fe_2O_3
K, J m^{-3}	~10^4	~10^3	~2–7.7 × 10^5
(erg cm^{-3})	(~10^5)	(~10^4)	(~2–7.7 × 10^6)

The nature of high magnetocrystalline anisotropy of ε-Fe_2O_3 is not entirely clear. It is believed that for ferrites, it is determined by the dipole–dipole interactions of magnetic spins; however, we were unable to find the K value for ε-Fe_2O_3 calculated using an appropriate model. Sakurai *et al.*[278] only compared the magnetocrystalline anisotropy constants of ε-Fe_2O_3 calculated using the single-ion model and the dipole–dipole interaction model. They found that these two values should be approximately equal. The abnormally high constant K for ε-Fe_2O_3 was attributed[219] to strong spin–orbit coupling caused by the presence of an orbital magnetic moment in the iron ion. In turn, the orbital magnetic moment appears due to degeneracy of the iron electron levels caused by the charge transfer from the oxygen 2p orbitals to the iron 3d orbitals and by splitting of the electron orbitals by the crystal field.

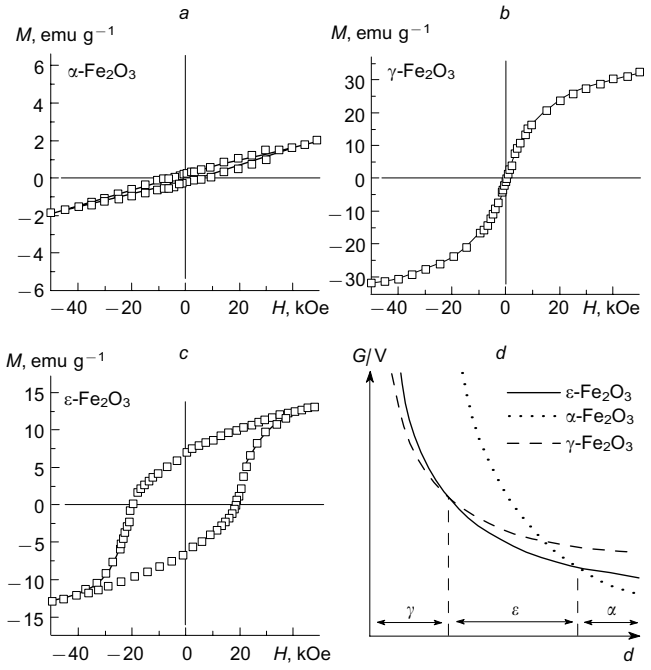


Figure 23. Magnetic hysteresis loops recorded at room temperature for α- (*a*), γ- (*b*) and ε-Fe_2O_3 (*c*) and dependences of the specific free energy for these phases on the particle size (*d*).[298] *a*: the plots are based on the data of Ref. 276. *G* is free energy, *V* is volume, *d* is particle diameter. Published with permission from Wiley and AIP Publishing.

The temperature dependence of the magnetic characteristics of ε-Fe_2O_3 is intricate. It was believed for a long time that at temperatures above 490 K, the material switches from the ferrimagnetic to paramagnetic state.[269] However, recently, it was discovered that this oxide remains ferrimagnetic up to 850 K.[279] Above the indicated temperature, ε-Fe_2O_3 becomes paramagnetic. On cooling down from room temperature, the coercivity first increases by ~10% to reach a maximum value at 200 K [272, 278] and then monotonically decreases. In the 100–150 K range, ε-Fe_2O_3 undergoes a series of magnetic transitions,[270, 278] which are accompanied by a sharp decrease in the spontaneous magnetization and the coercivity (see Fig. 18).

Since ε-Fe_2O_3 is a metastable polymorph, its synthesis is more complicated than the synthesis of more prevalent α-Fe_2O_3 and γ-Fe_2O_3 polymorphs. According to the current paradigm, iron oxide nanoparticles can be stabilized as ε-Fe_2O_3 only in a limited range of particle size as a result of lower free energy of this phase compared to α- and γ-phases (Fig. 23 *d*). Therefore, ε-Fe_2O_3 samples normally contain impurity phases and, hence, ε-Fe_2O_3 nanoparticles are synthesized, most often, using stabilizing components. The most popular approach is to obtain ε-Fe_2O_3 in a silica matrix.[276, 279–286] The high-melting medium restricts the particle growth and is chemically inert towards iron oxide. The variation of parameters such as concentration of iron oxide in the matrix, temperature and annealing time make it possible to select the optimal conditions to obtain ε-Fe_2O_3 in more than 90% yield;[280, 283, 286] to attain 100% yield by phase stabilization, it is efficient to add alkaline earth metal cations (Ba^{2+}, Sr^{2+}, Ca^{2+}).[276, 287]

Methods for the synthesis of ε-Fe_2O_3 nanoparticles have been actively developed in recent years, because this is the only nano-sized oxide magnet with a giant coercivity at room temperature that contains no noble elements, which motivates its use. In the general case, nanoparticles are synthesized by hydrolysis of TEOS, precursor of silica, either in the presence of iron oxide salts and modifying additives (metal salts) or in the presence of ε-Fe_2O_3 precursor nanoparticles. Another existing approach consists in impregnation of a ready mesoporous SiO_2 matrix with an iron nitrate solution.[288] The resulting gel is dried and heat-treated at temperatures ranging from 900 °C to 1200 °C for 3–4 h. The iron oxide particles are separated from the non-magnetic matrix by dissolving the matrix in concentrated aqueous NaOH.

In addition, a number of studies describe the formation of ε-Fe_2O_3 in the absence of a SiO_2 matrix. The stabilization can take place, for example, upon the epitaxial growth of thin films of ε-Fe_2O_3 on a substrate [289–292] or on crystallites with a related crystal structure.[293, 294] Examples of the preparation of nanoparticles of this oxide by hydrothermal synthesis,[295] plasma dynamic method [296] and high-frequency discharge method [297] were reported. However, the obtained samples had a low coercivity.

Thus, particular attention is deserved by the methods of synthesis of ε-Fe_2O_3 particles in SiO_2 matrices either containing alkaline earth metal cations or without them. Without additives, the ε-Fe_2O_3 phase is formed as spherical nanoparticles, while in the presence of additives, anisotropic crystals (nanorods and nanothreads) are formed, with ε-Fe_2O_3 yield reaching 100%.

The coercivity of ε-Fe_2O_3 can be increased by three methods: by varying the chemical composition, changing the morphology of crystallites and magnetic alignment. The first approach was demonstrated only by doping ε-Fe_2O_3 with rhodium or ruthenium cations.[284, 285, 288] The Rh^{3+} electron configuration is $4d^6$, and in the medium-strength octahedral field (oxygen environment), this ion occurs in the low-spin state ($t_{2g}^6e_g^0$) with zero spin and orbital moments ($S = 0$, $L = 0$). According to the Rietveld refinement of the structure, rhodium is inserted into the Fe_C octahedral sites with uncompensated magnetic moment.[285, 288] If one assumes that the constant of magnetocrystalline anisotropy changes insignificantly, the insertion of rhodium into the ε-Fe_2O_3 structure is expected to decrease the magnetization and increase the coercivity of the material, since $H_c \propto M_s^{-1}$. For example, it was shown [285, 288] that the increase in the rhodium content in ε-$Rh_xFe_{2-x}O_3$ from $x = 0$ to 0.19 leads to an increase in the coercivity from 1592 kA m^{-1} (20 kOe) to 2236 kA m^{-1} (28.1 kOe) and a concomitant decrease in the saturation magnetization from 15 A m^2 kg^{-1} (15 emu g^{-1}) to 6 A m^2 kg^{-1} (6 emu g^{-1}).

When ε-Fe_2O_3 is doped with ruthenium, a different mechanism of coercivity increase is implemented. The Ru^{3+} ion has a $4d^5$ electronic configuration; hence, in the low-spin state in both octahedral ($t_{2g}^5e_g^0$) and tetrahedral ($t_{2g}^4e^1$) oxygen environments, the ion has a non-zero orbital moment. This gives rise to spin–orbit coupling and, as a consequence, to a pronounced change in the magnetocrystalline anisotropy.[299] Using the general chemical considerations and quantum chemical calculations, Namai and Ohkoshi [284] suggested that the Ru^{3+} cation is inserted into the Fe_C octahedral site with uncompensated magnetic moment. This increases the coercivity by 15%: from 1409 kA m^{-1} (17.7 kOe) for pure ε-Fe_2O_3 to 1623 kA m^{-1} (20.4 kOe) for ε-$Ru_{0.014}Fe_{1.986}O_3$. Appa-

rently, the increase in the coercivity is caused by particularly the spin–orbit coupling induced by the appearance of the cation with a non-zero orbital moment. This hypothesis is supported by the fact that the particle size and shape in the series ε-Fe_2O_3, ε-$Ru_{0.005}Fe_{1.995}O_3$, ε-$Ru_{0.014}Fe_{1.986}O_3$ are approximately the same.

Thus, one should not expect different coercivities due to different particle morphology. The insignificant decrease in the saturation magnetization in the indicated series of compositions should not affect the coercivity increase either, because the presence of up to 5.7 mass % weakly magnetic α-Fe_2O_3 impurity phase should decrease the magnetization, which should, conversely, decrease the coercivity. However, the expediency of doping ε-Fe_2O_3 with even minor amounts of expensive ruthenium to increase the coercivity is still an open question. Indeed, Popovici *et al.*[280] obtained undoped ε-Fe_2O_3 samples with an equally high coercivity [1592 kA m^{-1} (20 kOe)] for the same particle size of 20 nm.

It should be noted that the addition of rhodium and, probably, ruthenium cations narrows down the range of particle size in which ε-Fe_2O_3 is the most stable polymorph. As a consequence, these systems contain considerable amounts of impurity phases.[284,285,288] When ε-Fe_2O_3 is doped with other cations (Ga^{3+}, Al^{3+}, In^{3+}, Cr^{3+}, Co^{2+} or Ti^{4+}), the coercivity decreases.[300–303]

The effect of particle morphology of ε-Fe_2O_3 on the magnetic hardness has not yet been adequately addressed in the literature. To our knowledge, there is only one publication[286] devoted to the dependence of ε-Fe_2O_3 coercivity on the particle diameter. Using published data,[276,279,280–286,295] we plotted the coercivity *versus* the particle volume for pristine ε-Fe_2O_3 (Fig. 24). The superparamagnetic limit for this compound corresponds to a spherical particle of 7.5 nm in diameter ($V \approx 220$ nm^3).[286] An increase in the particle volume is accompanied by increasing coercivity, which reaches a plateau when the particle size is ~25 nm ($V = 8200$ nm^3). We were unable to find a critical diameter of the magnetic domain (d_{cr}) of ε-Fe_2O_3 reported in the literature; therefore, we calculated this value by the formula[223]

$$d_{cr} = \frac{9}{2\pi}\frac{\sigma_w}{M_{sv}^2} \qquad (14)$$

where

$$\sigma_w = \left(\frac{2k_B T_C |K_1|}{a}\right)^{1/2}$$

is the energy of domain wall per unit area, k_B is the Boltzmann constant, a is the average distance between the paramagnetic atoms in the structure, M_{sv} is the volume saturation magnetization ($M_{sv} = \rho M_s$, ρ is the material density, M_s is the saturation magnetization in emu g^{-1}). The following values were used in calculations: $K_1 = 3.92 \times 10^5$ kJ m^{-3} (3.92×10^6 erg cm^{-3}),[304] $a = 3$ Å (Ref. 270), $M_{sv} = 100$ kA m^{-1} (100 emu cm^{-3}), $T_C = 500$ K.[270] The calculated diameter was 6 μm, while the critical volume of the magnetic domain of ε-Fe_2O_3 was estimated as $V_{cr} = \pi d_{cr}^3/6 \approx 113$ μm^3. The preparation of ε-Fe_2O_3 particles with sizes comparable with the calculated d_{cr} value was not reported in the literature. The only form of existence of ε-Fe_2O_3 particles of the characteristic size are thin films. The coercivity of ε-Fe_2O_3 thin films is actually much lower than that of nanoparticles and amounts to < 796 kA m^{-1} (< 10 kOe).[289–292]

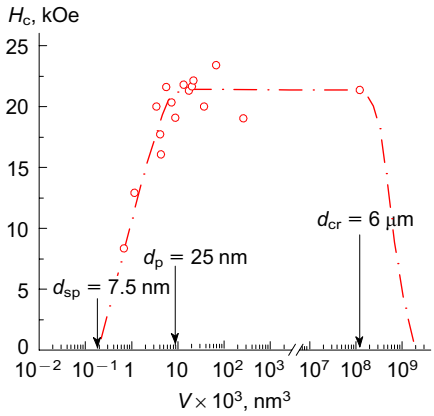


Figure 24. Coercivity of ε-Fe_2O_3 *vs.* particle volume (V). d_{sp} is the critical diameter corresponding to the superparamagnetic limit, d_p is the particle size at which the $H_c(V)$ dependence reaches a plateau, d_{cr} is the estimated critical diameter of the magnetic domain. The figure was created by the authors using published data.[276,279,280–286,295]

Apart from the particle size, an important characteristic affecting the material coercivity is the particle shape. The coercivity of rod-like ε-Fe_2O_3 particles is greater than that of isotropic particles by $\sim 2\pi \times 5$ g $cm^{-3} \times 20$ emu $g^{-1} \approx 630$ Oe (50 kA m^{-1}), which gives a coercivity gain of only 3.2% [for $H_c = 1592$ kA m^{-1} (20 kOe)]. Thus, it can be concluded that the particle shape has little effect on the magnetic hardness of ε-Fe_2O_3.

In addition to particle morphology, other factors that can affect the magnetic hardness of this oxide include the structural quality of crystallites and particle size distribution. For example, the coercivity determined by Nakaya *et al.*[283] for a monodisperse ensemble of 41 nm cubic particles exceeded 1830 kA m^{-1} (23 kOe), which is the highest value known for undoped ε-Fe_2O_3. This value of coercivity could be due to both the narrow particle size distribution and probably high quality of the particle crystal structure formed owing to a greater (compared to other studies) annealing time of 200 h.

One more efficient approach to increasing the coercivity of an ensemble of ε-Fe_2O_3 particles is magnetic field alignment.[220,286,305,306] In the general case. this procedure is performed in the following way.[220] First, polymers, such as polyurethane and polyvinyl chloride, are dissolved in acetylacetone and cyclohexanone; this solution is mixed with a suspension containing ferrite particles, solvents (toluene, butan-2-ol) and zirconia beads. Then the resulting mixture is homogenized, in particular by shaking. The ready solution is deposited on a substrate, which is allowed to dry in a vertical magnetic field of 30 kOe. Measurement of the hysteresis loop along the orientation axis showed a higher coercivity and a higher squareness ratio of the hysteresis loop (M_r/M_s) compared to the non-oriented sample. The coercivity attained for pure ε-Fe_2O_3 using this approach was 2005 kA m^{-1} (25.2 kOe) *versus* 1592 kA m^{-1} (20 kOe) for the non-oriented sample.[271] Ohkoshi *et al.*[220] carried out magnetic alignment of ε-$Rh_{0.14}Fe_{1.86}O_3$ particles with a coercivity of 2149 kA m^{-1} (27 kOe)[288] and thus they were able to increase this value to 2785 kA m^{-1} (35 kOe) (for the hysteresis loop squareness ratio of 0.83). Currently, this

coercivity is the highest one for materials based on ε-Fe_2O_3 at room temperature. Cooling of this sample to 200 K resulted in a coercivity increase to 3581 kA m^{-1} (45 kOe). However, as in the case of the pristine oxide, further cooling induced a sharp decrease in the coercivity of $Rh_{0.14}Fe_{1.86}O_3$ (see Fig. 18).

Apart from very high coercivity, ε-Fe_2O_3 shows a natural ferromagnetic resonance in the subterahertz frequency range (100–300 GHz). The ferromagnetic resonance frequency of pristine oxide particles at room temperature is ~180 GHz. The increase in the coercivity *via* doping with rhodium cations (ε-$Rh_xFe_{2-x}O_3$) is accompanied by increase in this frequency from 182 ($x = 0$) to 222 GHz ($x = 0.19$).[285,288] Currently, this approach is the only one capable of increasing the ferromagnetic resonance frequency of ε-Fe_2O_3.

6.4. Substituted M-type hexaferrites

Hard magnetic properties of hexagonal M type ferrites (hexaferrites) were discovered in the early 1950s.[4] Hexaferrites served as they key materials for the manufacture of permanent magnets up to the 2000s, when magnets based on Nd–Fe–B alloys started to be widely used. Ferrite magnets have much lower magnetizations, coercivities and, hence, $(BH)_{max}$; however, they also possess a number of important advantages. First, the production processes of ferrites are well developed and they contain no rare or expensive elements; therefore, the ferrite-based magnets are much less expensive. Second, hexaferrites are chemically and thermally more stable than metal alloys. Third, they absorb the electromagnetic radiation at frequencies up to 100 GHz, which is not inherent in metal alloys. Owing to their low cost, hexaferrites account for up to 80% of the world production output of permanent magnets and occupy ~30% of the global market. Detailed information about the long-term studies of M-type hexaferrites can be found in the literature.[1,5] In this review, the attention is focused on the ways for attaining ultrahigh coercivity for these compounds.

M-type hexaferrites are solid oxides with the general formula $MFe_{12}O_{19}$ (M = Ba, Sr, Pb); they are isomorphic to magnetoplumbite, a mineral with the approximate composition $Pb_2Fe_{15}Mn_7AlTiO_{38}$ (Refs 1, 5). The crystal structure of magnetoplumbite corresponds to space group $P6_3/mmc$. The crystal lattice can be conceived in the following way. The oxygen ions form a hexagonal close packing, with the succession of layers perpendicular to the [001] direction looking like ABAB... or ACAC.... In every fifth layer, one O^{2-} ion is replaced by M^{2+}, which is possible due to the similarity of their ionic radii.[307] The iron ions, which are markedly smaller, occupy voids between the oxygen ions (Fig. 25). Note that the structure can be represented by a combination of two types of blocks: spinel blocks S (with the [111] axis directed along the *c* axis of the crystal lattice) and hexagonal blocks R containing an M^{2+} ion instead of one oxygen ion. The blocks alternate in the structure according to the SRS*R* pattern, where S* and R* are blocks rotated by 180° relative to the previous blocks. The iron ions in the hexaferrite structure are located in five different crystallographic sites — three octahedral (2a, $4f_2$, 12k), one tetrahedral ($4f_1$) and one trigonal-bipyramidal (2b) ones. The magnetic moments of iron ions in each site are directed along the crystallographic *c* axis, while the relative orientation of the moments is determined by the superexchange interaction involving oxygen ions: they are

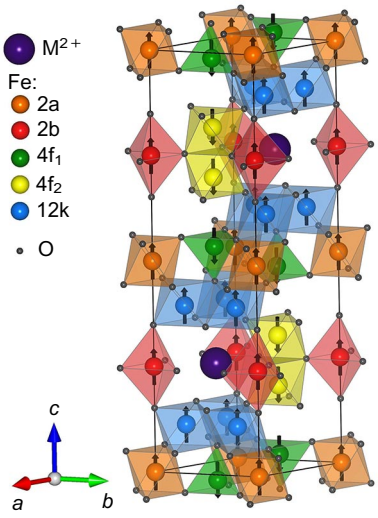


Figure 25. Oxygen polyhedra in the crystal structure of M-type hexaferrite. The arrows mark the directions of the magnetic moments of ions. The figure was created by the authors using data of Refs 1 and 5.

parallel for 2a, 2b and 12k and antiparallel for $4f_1$ and $4f_2$. Thus, M-type hexaferrites are uniaxial ferrimagnets in which the easy magnetization axis coincides with the crystallographic *c* axis.

Barium and strontium hexaferrites have positive magnetocrystalline anisotropy constants $K_1 \approx 3.5 \times 10^5$ J m^{-3} (3.5×10^6 erg cm^{-3}) at room temperature, H_a = 1330–1470 kA m^{-1} (16–19 kOe), $M_s \approx 70$ A m^2 kg^{-1} (70 emu g^{-1}); the Curie temperature is ~750 K.[1] The magnetocrystalline anisotropy of M-type hexaferrites is associated with the dipole–dipole interaction between iron ions and their single-ion anisotropy.[308] The magnetocrystalline anisotropy constant K_1 of M-type hexaferrites calculated by the dipole–dipole interaction model was ~10% lower,[309] while that calculated using the single-ion model was ~4 times lower[310,311] than the experimental value.[1] In all probability, the dipole–dipole interaction makes the highest contribution to the magnetocrystalline anisotropy of hexaferrites. However, detailed consideration of the magnetocrystalline anisotropy and calculation of K_1 for hexaferrites requires, like in the case of ε-Fe_2O_3,[278] that both factors are taken into account. Although the single-ion anisotropy is not a primary factor, this approach makes it possible to determine the contributions of the iron sublattices to the magnetocrystalline anisotropy of hexaferrite, which are needed to consider the replacement of iron ions in the structure. According to the single-ion model of Fe^{3+}, the 2b sublattice has the greatest positive contribution and 12k makes the greatest negative contribution to the magnetocrystalline anisotropy of hexaferrite, whereas the contributions of iron in other sublattices ($4f_1$, $4f_2$, 2a) are insignificant. The constant K_1 and saturation magnetization decrease with increasing temperature, and the H_a and H_c values reach a maximum above the room temperature (Fig. 26).

Like in the case of ε-Fe_2O_3, the highest coercivity values are found for single-domain hexaferrite particles, in which magnetization reversal mainly takes place by the coherent spin rotation mechanism. According to different data, the limiting size of the magnetic domain for undoped compounds is in the range of 500–1000 nm.[1,5,313,314] In the ideal case of coherent spin rotation in the magnetization reversal of a powder with randomly oriented particles, according to the Stoner–Wohlfarth model, the maximum coercivity is $H_c^{max} = 0.48\,H_a = 0.48(2K_1/\mu_0 M_{sv})$, which

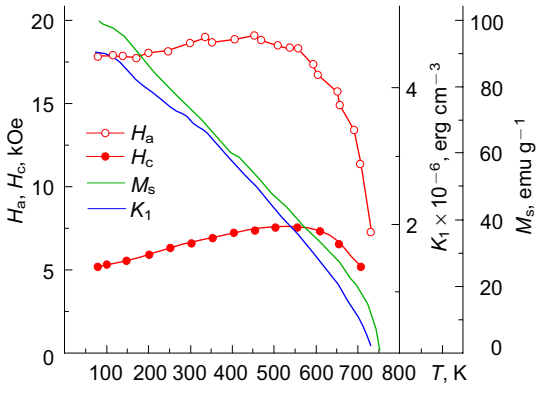


Figure 26. Temperature dependences of M_s, K_1, H_a and H_c (limiting theoretical value) for $SrFe_{12}O_{19}$. The figure was created by the authors using data of Ref. 312.

amounts to ~716 kA m^{-1} (9 kOe) for strontium hexaferrite. However, in reality, such values are not attained because of non-coherent spin rotation, contribution of other types of magnetic anisotropy (mainly the shape anisotropy and the surface anisotropy) and the mutual influence of particles. Typical commercial ceramic samples have a coercivity of 200–360 kA m^{-1} (2.5–4.5 kOe), while the coercivity of materials based on highly dispersed powders can reach 500 kA m^{-1} (6.3 kOe).[315,316] Thus, there are two necessary conditions for obtaining high coercivity of hexaferrites: the formation of single-domain particles and increase in the anisotropy field. The main method for changing the anisotropy field is to replace cations in the hexaferrite structure.

The replacement of Ba^{2+} ions by Sr^{2+} and Pb^{2+} in any ratio does not induce a transformation of the crystal structure. The magnetic properties of the resulting solid solutions smoothly change following the change in composition if identical conditions of synthesis are maintained.[317] Some publications indicate that the hard magnetic properties of hexaferrites are enhanced by replacement of the M^{2+} cation with lanthanide ions, particularly, La^{3+} ions.[318–320] However, the reported effects are insignificant, and the attained coercivity values do not exceed record-high characteristics for pristine phases and can be attributed to more favourable microstructure for this particular method of synthesis. In this regard, attention is attracted by a study of Ueda *et al.*,[321] who demonstrated that lanthanum substitution actually increases the magnetocrystalline anisotropy. The authors obtained single crystals of $Sr_{1-x}La_xFe_{12-x}Co_xO_{19}$ $(0 \leqslant x \leqslant 0.4)$ and $Sr_{1-x}La_xFe_{11.6}Co_{0.4}O_{19}$ $(0.5 \leqslant x \leqslant 1)$ and systematically studied their magnetic properties. Cobalt is added, as a rule, together with lanthanum, to counterbalance the charge; in this case, the increase in the magnetocrystalline anisotropy is attributed to the presence of non-vanishing orbital moment in Co^{2+} ions. The single crystals were grown by zone melting at an oxygen pressure of 10 atm. The anisotropy fields of the obtained samples were determined from the points where $M(H)$ reach saturation for magnetization perpendicular to the c axis of the crystal (Fig. 27). At room temperature, the anisotropy field of a $LaFe_{11.6}Co_{0.4}O_{19}$ sample was 2387 kA m^{-1} (30 kOe), while at 5 K, this value increased to 3342 kA m^{-1} (42 kOe). It is important that increase in H_a following lanthanum substitution is not accompanied by a decrease in the magnet-

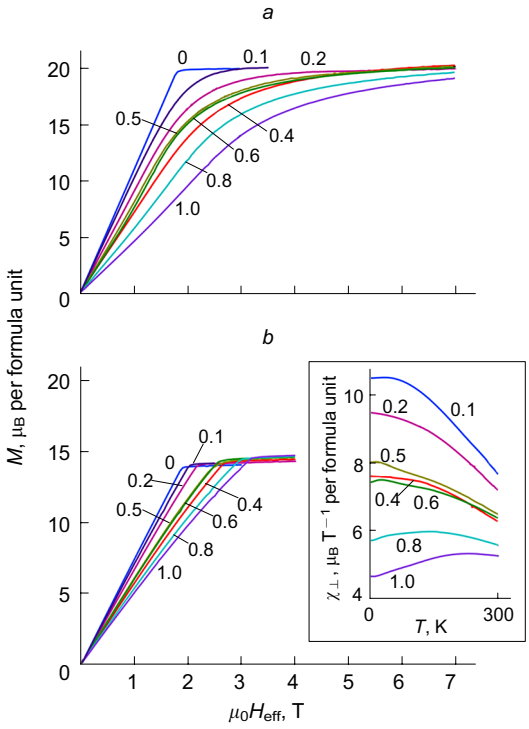


Figure 27. Magnetization curves of the $Sr_{1-x}La_xFe_{12-y}Co_yO_{19}$ single crystals in a magnetic field perpendicular to the easy magnetization axis measured at 5 (*a*) and 300 K (*b*).[321] The inset shows the temperature dependence of the magnetic susceptibility in a 0.1 T field. The numbers at the curves correspond to x. Published with permission from the American Physical Society.

ization. The authors noted that the increase in the magnetocrystalline anisotropy is caused by spin–orbit coupling in not only Co^{2+}, but also Fe^2 ions, which appears in the hexaferrite structure as a result of charge compensation. The synthesis of single-domain hexaferrite particles with such anisotropy fields and retained high magnetization would result in a considerable increase in the coercivity and the energy product $(BH)_{max}$; however, this synthesis has not yet been implemented. The main problem is the difficulty of obtaining hexaferrites with a high lanthanum content. It was shown[322] that $LaFe_{12}O_{19}$ exists only in a narrow temperature range of 1360–1400 °C. Under these conditions, hexaferrite particles rapidly grow, and hence the single-domain limit is exceeded. Choi *et al.*[323] were able to synthesize ~80 nm $(La-Co)_xSr_{1-x}Fe_{12-x}O_{19}$ particles by the sol–gel method. Single-phase samples were formed in the $0 < x < 0.4$ range. It was shown that the magnetocrystalline anisotropy constant K_1 increases to 4.85×10^5 J m^{-3} (4.85×10^6 erg cm^{-3}) at $x = 0.2$, while the coercivity amounts to 599 kA m^{-1} (7.5 kOe). This is markedly higher than the values attained for pristine hexaferrites, but still markedly lower than the data for ε-Fe_2O_3.

The replacement of iron ions in hexaferrites makes it possible to vary their magnetic properties, in particular, to change the anisotropy field H_a. Most of known and well-studied substituting ions (Sc^{3+}, In^{3+}, Ti^{4+}/Co^{2+}, Ti^{4+}/Zn^{2+}, Mn^{2+})[1,5] lead to decreasing H_a. We will consider in detail the ions that can induce an increase in the anisotropy field and coercivity: Al^{3+}, Ga^{3+}, Cr^{3+} and Ru^{3+}.

The paramagnetic Ru^{3+} ion has a non-zero orbital moment; therefore, the mechanism of its effect on the

magnetic properties of hexaferrite differs from the mechanism of influence of other ions. In relation to $PbFe_{12-x}Ru_xO_{19}$ single crystals, Zhai *et al.*[324] demonstrated that the introduction of a minor amount of Ru^{3+} up to $x = 0.05$ leads to increase in K_1 to 27% at 273 K. Simultaneously, H_a increases from ~1154 kA m^{-1} (~14.5 kOe) to 1631 kA m^{-1} (20.5 kOe). Further increase in the Ru^{3+} content induces monotonic decrease in the magnetocrystalline anisotropy. A partial replacement of iron atoms by ruthenium is one of the few methods that lead to increasing anisotropy field of hexaferrite *via* an increase in K_1 rather than a decrease in the magnetization. Furthermore, only a minor amount of the dopant is required to attain the greatest effect; therefore, doping with ruthenium may be a reasonable approach to prepare high-coercivity hexaferrites.

Due to the similar ionic radii and equal charges, Al^{3+}, Ga^{3+} and Cr^{3+} ions, while replacing Fe^{3+} ions in hexaferrites, form continuous series of solid solutions.[1] The substitution results in decreasing saturation magnetization M_s and Curie temperature. The anisotropy field H_a sharply increases when Fe^{3+} is replaced by Al^{3+}, slightly increases upon the replacement by Ga^{3+} and changes non-monotonically upon the introduction of Cr^{3+} (see Fig. 28). The causes for this behaviour are related, first of all, to different distributions of substituting cations among the iron sites in the hexaferrite structure. Since aluminium and gallium ions do not possess magnetic moments, and the magnetic moment of chromium (3 μ_B) is lower than that of iron (5 μ_B), the insertion of these ions into the structure reduces the magnetization of the corresponding sublattices. Aluminium enters mainly 2a and 12k sites,[1,308,325] in which the direction of iron spins coincides with the direction of the overall magnetization of the crystal. This results in a sharp decrease in the saturation magnetization with increasing degree of substitution. The Ga^{3+} ions substitute iron mainly in $4f_1$ and 12k sites;[308] therefore, magnetization decreases more slowly (see Fig. 28). Chromium enters the octahedral 2a, 12k and $4f_2$ sites;[326] therefore, the saturation magnetization decreases more slowly than upon the insertion of aluminium but more rapidly than upon the insertion of gallium. The magnetocrystalline anisotropy constant K_1 (single-ion contribution) is mainly determined by 2b site and, presumably, the substitution of Al^{3+}, Ga^{3+} and Cr^{3+} ions decreases the constant K_1 approximately to the same extent.[308] Finally, the H_a value is mainly determined by the saturation magnetization, which decreases most rapidly upon the insertion of aluminium (see Fig. 28), with K_1 decreasing more slowly (Fig. 29), which thus results in a sharp growth of H_a. For example, the anisotropy field of $SrFe_{12-x}Al_xO_{19}$ reaches 4249 kA m^{-1} (53.4 kOe) at $x = 3.4$ and tends to further increase with increasing x (see Fig. 28).[1,327]

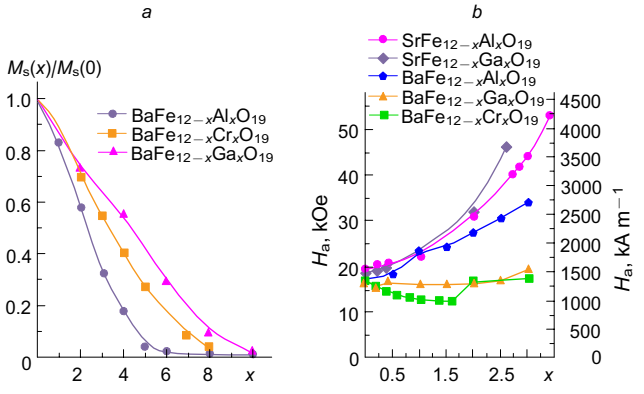


Figure 28. Concentration dependences of the reduced saturation magnetization (*a*) and anisotropy field (*b*) for M-type hexaferrites substituted with Al^{3+}, Ga^{3+} and Cr^{3+} ions; the measurement temperature is 300 K. The figure was created by the authors using published data.[1,327]

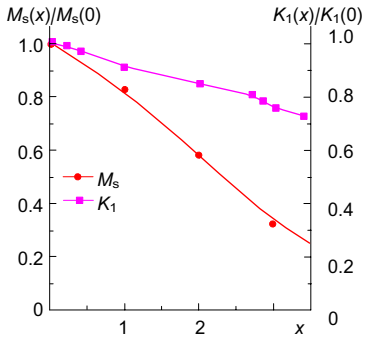


Figure 29. Concentration dependences of the reduced saturation magnetization and the magnetocrystalline anisotropy constant for $SrFe_{12-x}Al_xO_{19}$ at 300 K. The figure was created by the authors using data of Ref. 327.

Thus, the replacement of iron by aluminium is the most promising approach to the preparation of hexaferrites with giant coercivity. However, the insertion of aluminium into the hexaferrite structure requires high temperatures, especially for high degrees of substitution. For example, in most publications, single-phase $MFe_{12-x}Al_xO_{19}$ samples (M = Ba, Sr) were synthesized at temperatures of 1300–1400 °C,[1,325] at which the single-domain limit is certainly exceeded.

Wang *et al.*[328] synthesized the single-domain particles with the composition $BaFe_{10}Al_2O_{19}$. Mechanical activation was used to increase the reactivity of the starting compounds and decrease the temperature of synthesis. The initial mixture was milled in a planetary ball mill for 36 h and then annealed at temperatures of 700–1300 °C for 1 h. The highest coercivity was attained after the annealing at 1100 °C and amounted to 740 kA m^{-1} (9.3 kOe) at a magnetization of 36 A m^2 kg^{-1} (36 emu g^{-1}) and an average particle size of 100 nm. At higher temperatures, the particle size increased and the coercivity decreased. The authors noted that a roughly single-phase sample was obtained only at 1300 °C.

Kazin and co-workers[329–333] used the glass crystallization method to obtain aluminium-substituted strontium hexaferrite. The method is based on the fact that the $MFe_{12}O_{19}$ hexaferrite phase in the $MO-Fe_2O_3-B_2O_3$ systems (M = Ba, Sr) occurs in the thermodynamic equilibrium with the glass-forming MB_2O_4 and $M_2B_2O_5$ borates.[334,335] Heat treatment of glasses in these systems under certain conditions may give single-domain hexaferrite particles.[336,337] The authors demonstrated that crystallization of glasses upon the addition of alumina to the initial $SrO-Fe_2O_3-B_2O_3$ system gives rise to $SrFe_{12-x}Al_xO_{19}$ particles. By heat treatment of the $13\,SrO-5.5\,Fe_2O_3-4.5\,Al_2O_3-4\,B_2O_3$ glass at 950 °C for 24 h, they obtained $SrFe_{10.7}Al_{1.3}O_{19}$ particles with an average size of 350 nm distributed in a non-magnetic matrix ($SrAl_2O_4$ and $Sr_2B_2O_5$).[330] This glass ceramic material had a coercivity of 810 kA m^{-1} (10.18 kOe). After a two-stage heat treatment of glass of the same composition (2 h at 750 °C and 24 h at 970 °C), the coercivity of the material increased to 995 kA m^{-1} (12.5 kOe).[332] The method is primarily of

interest due to the fact that it allows dissolution of matrix phases in dilute HCl and formation of single-phase hexaferrite powders consisting of non-aggregated single-crystalline particles.

Luo *et al.*[314] synthesized $SrFe_{12-x}Al_xO_{19}$ nanoparticles ($0 \leqslant x \leqslant 12$) by auto-combustion of citrate–nitrate mixtures followed by heat treatment of the resulting precursors. The synthesis was carried out with stoichiometric amounts of metal nitrates, which were dissolved in a minor volume of water. Citric acid was added to the solutions, so that the molar ratio of metal ions to citric acid molecules was 1 : 1, then aqueous ammonia was added for neutralization. After that, the solutions were evaporated at 100 °C (or at higher temperature) until auto-combustion took place to form a low-density powder, which was heat-treated at 1100 °C for 12 h. The particles thus formed had sizes below the critical single-domain limit. The coercivity increased from 195 kA m^{-1} (2.4 kOe) for $x = 0.5$ to 589 kA m^{-1} (7.4 kOe) for $x = 2$ and reached a maximum of 1440 kA m^{-1} (18.1 kOe) for $x = 4$, while the M_s values for these samples were 46.7, 36.5 and 9.0 A m^2 kg^{-1} (46.7, 36.5 and 9.0 emu g^{-1}), respectively. At $x \geqslant 6$, the samples became paramagnetic. The M_s values proved to be somewhat lower than the expected ones, thus indicating the presence of non-magnetic impurities. Nevertheless, it was confirmed that aluminium-doped hexaferrites can possess very high coercivity. Good prospects of the auto-combustion method for the preparation of single-domain particles were noted.

Analogous results were obtained[338, 339] in the synthesis of $SrFe_{12-x}Al_xO_{19}$ ($0 \leqslant x \leqslant 4$) by a similar procedure using glycine, instead of citric acid, in 1.5 : 1 ratio to metal ions. The powders formed after combustion of the initial mixture were pressed into disks and annealed at 750–1250 °C for 2 h. The highest magnetic characteristics were as follows: for $SrFe_9Al_3O_{19}$ (1200 °C), M_s = 17 A m^2 kg^{-1} (17 emu g^{-1}), H_c = 1372 kA m^{-1} (17.2 kOe); for $SrFe_8Al_4O_{19}$ (1000 °C), M_s = 7.5 A m^2 kg^{-1} (7.5 emu g^{-1}), H_c = 1398 kA m^{-1} (17.6 kOe).

The auto-combustion technique of citrate–nitrate mixtures for the preparation of single-domain $SrFe_{12-x}Al_xO_{19}$ particles was further developed by Trusov *et al.*[277] The authors suggested that the porous structure of the precursor can restrict the diffusion during heat treatment and prevent the intense particle growth. This would allow annealing at higher temperature, with the particle size remaining in the single-domain region. The temperature rise is important for completion of the solid-state reaction and efficient insertion of aluminium into the hexaferrite. The porous precursor was synthesized using mixtures with 3 : 1 molar ratio of citric acid molecules to metal ions. The obtained precursor was heated at a rate of 10 °C min^{-1} to 1200 °C and kept at this temperature for 24 h, which resulted in the formation of single-phase $SrFe_{12-x}Al_xO_{19}$ powders ($0 \leqslant x \leqslant 4$) with an average particle size of ~500 nm. The coercivity increased with increasing degree of substitution and reached 1472 kA m^{-1} (18.5 kOe) for $SrFe_8Al_4O_{19}$ at the saturation magnetization of 12.9 A m^2 kg^{-1} (12.9 emu g^{-1}). In addition, it was shown that the simultaneous replacement of strontium by calcium leads to further increase in H_c. For example, the coercivity of $Sr_{0.67}Ca_{0.33}Fe_8Al_4O_{19}$ increased to 1695 kA m^{-1} (21.3 kOe), with the saturation magnetization being 12.7 A m^2 kg^{-1} (12.7 emu g^{-1}). The authors suggested that this is associated with additional compression of the crystal cell upon replacement of strontium ions

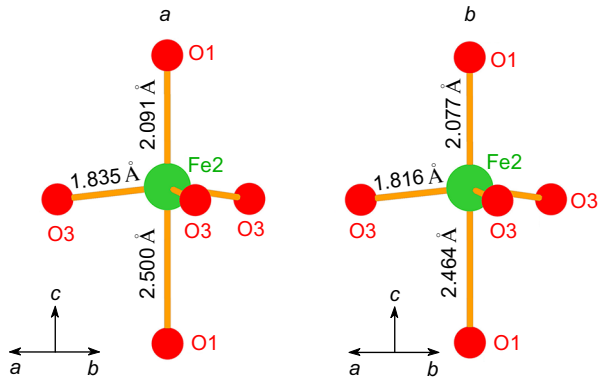


Figure 30. Oxygen environment of the Fe^{3+} ion in the 2b sublattice of M-type hexaferrite for $SrFe_8Al_4O_{19}$ (*a*) and $Sr_{0.67}Ca_{0.33}Fe_8Al_4O_{19}$ (*b*).[277] Published with permission from the Royal Society of Chemistry.

(r^{XII} = 1.44 Å) by smaller calcium ions (r^{XII} = 1.34 Å).[307] It was found that calcium substitution leads to compression of the oxygen environment of iron in the 2b site (Fig. 30), which makes a great contribution to the formation of the magnetocrystalline anisotropy of hexaferrites. The compression increases the crystal field strength at this site and the magnetocrystalline anisotropy. Thus, a material based on M-type hexaferrite with better characteristics compared to ε-Fe_2O_3 was obtained. This was done using a facile and scalable method, which can be easily integrated into the existing production processes of ferrite materials.

Gorbachev *et al.*[223] studied hexaferrites with even higher degrees of Ca–Al double substitution. They obtained

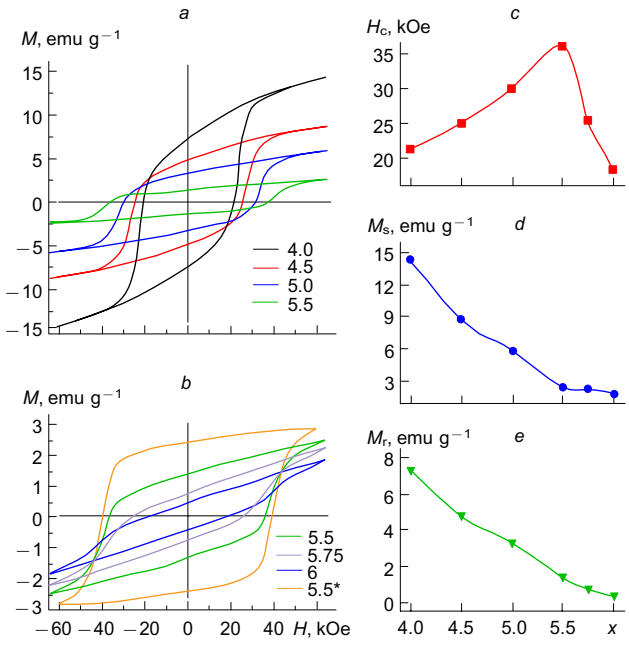


Figure 31. Magnetic hysteresis loop at 300 K for the single-domain particles of oriented samples of hexaferrites $Sr_{1-x/12}Ca_{x/12}Fe_{12-x}Al_xO_{19}$ ($4 < x < 6$) (*a*, *b*) and dependences of coercivity, saturation magnetization and remanent magnetization on the aluminium content (*c*–*e*).[223] *a*, *b*: the numbers written at the designations of curves are *x* values; the asterisk marks the oriented sample. Published with permission from Elsevier.

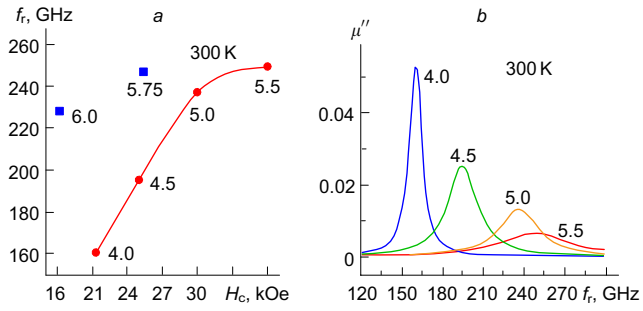


Figure 32. Ferromagnetic resonance frequency f_r *vs.* coercivity for $Sr_{1-x/12}Ca_{x/12}Fe_{12-x}Al_xO_{19}$ ($4 \leqslant x \leqslant 5.5$) (*a*) and imaginary part of the magnetic permittivity (μ'') *vs.* microwave frequency (*b*). Adapted from Ref. 223. The numbers written at the points and the curves are *x* values. Published with permission from Elsevier.

single-domain particles of the $Sr_{1-x/12}Ca_{x/12}Fe_{12-x}Al_xO_{19}$ phases ($4 \leqslant x \leqslant 6$) and showed that the coercivity increased up to $x = 5.5$ to reach 2865 kA m^{-1} (36 kOe) (Fig. 31 *a*). This value exceeds the highest coercivity for both disordered and crystallographically oriented ε-$Rh_{0.14}Fe_{1.86}O_3$ particles.[220,288] The magnetic alignment of particles with $x = 5.5$ afforded a material with a coercivity of 3183 kA m^{-1} (40 kOe) (Fig. 31 *b*).

The increase in the anisotropy field H_a upon the aluminium substitution considerably increased the ferromagnetic resonance frequency. The obtained samples showed resonance electromagnetic absorption at 160 ($x = 4$), 195 ($x = 4.5$), 237 ($x = 5$), 250 ($x = 5.5$), 247 ($x = 5.75$) and 228 GHz ($x = 6$) (Fig. 32). The values >230 GHz are the highest among the frequencies for known materials (*e.g.*, for ε-$Rh_{0.14}Fe_{1.86}O_3$, the ferromagnetic resonance frequency is 222 GHz).[285] Thus, single-domain particles of aluminium-substituted hexaferrites are now a promising base for the design of ultrareliable magnets and subterahertz electronic devices. The major advantage of ε-Fe_2O_3 is still very small size of high-coercivity particles, while hexaferrites are characterized by facile synthesis, low cost and ready availability of the raw material.

7. Other non-metal compounds

Apart from the known high-coercivity materials described above, there are exotic compounds such as $Sr_5Ru_{4.1}O_{15}$, $La_2Ni_{1.19}Os_{0.81}O_6$, Lu_2NiIrO_6 and Fe_3Se_4, which also have high magnetic hardness. The magnetic properties of these materials are mainly of interest for fundamental research.

In 2010, $Sr_5Ru_{4.1}O_{15}$, a new compound exhibiting giant coercivity in the low temperature range, was obtained.[340] A single crystal of the indicated composition was grown by cooling the melt in the $SrO-RuO_2-KCl-O_2$ system at an oxygen pressure of 4 GPa. It was shown that $Sr_5Ru_{4.1}O_{15}$ has a hexagonal crystal lattice (space group $P6_3/mmc$, unit cell parameters: $a = 5.56$, $c = 22.83$ Å). Tetra- and pentavalent ruthenium ions are located in three octahedral sublattices and have an average oxidation state of +4.87. At room temperature, $Sr_5Ru_{4.1}O_{15}$ is paramagnetic, while below 160 K it is converted to a weakly ferromagnetic state. It was assumed [340] that the ferromagnetic ordering is due to the superexchange interaction between the ruthenium ions located in face-sharing octahedra. Lowering the temperature of this oxide is accompanied by an extremely high increase in the coercivity, which is ~1592 kA m^{-1} (~20 kOe) at 50 K and reaches 9549 kA m^{-1} (120 kOe) at 1.7 K. However, the saturation magnetization of $Sr_5Ru_{4.1}O_{15}$ is very low. Indeed, at 3.6 K, the magnetic moment per ruthenium atom is only 0.07 μ_B. Exactly this weak ferromagnetism in combination with high magnetocrystalline anisotropy (caused by the non-zero orbital moment of ruthenium ions) account for the very high coercivity of this material.

One more material with a relatively high magnetic hardness is iron selenide Fe_3Se_4. This compound has a monoclinic crystal structure (space group $I2/m$, unit cell parameters: $a = 6.208$, $b = 3.541$, $c = 11.281$ Å). Iron selenide is a ferrimagnet with a Néel temperature of ~315 K; therefore, the coercivity of this compound at room temperature is moderate. The ferrimagnetism is due to the presence of vacancies, which are ordered in the $(\bar{1}01)$ plane.[341] A very high coercivity of this material was detected for the first time by Zhang *et al.*[342] The thermal decomposition of iron(III) acetylacetonate in the presence of selenium in an oleylamine solution gave ensembles of 50–500 nm Fe_3Se_4 particles with various morphologies (like nanocacti, nanoplatelets and nanosheets). At room temperature, Fe_3Se_4 particles had a saturation magnetization of ~5 A m^2 kg^{-1} (5 emu g^{-1}) and coercivity of 240–320 kA m^{-1} (3–4 kOe), while on cooling down to 10 K, the coercivity reached 2308 kA m^{-1} (29 kOe) for nanosheets, 2865 kA m^{-1} (36 kOe) for nanocacti and 3183 kA m^{-1} (40 kOe) for nanoplatelets. Simultaneously, M_s increased up to 15 A m^2 kg^{-1} (15 emu g^{-1}). These high coercivity values were attributed to high magnetocrystalline anisotropy of the material [$K_1 \approx 10^6$ J m^{-3} (10^7 erg cm^{-3}) at 10 K], which is a consequence of the low symmetry of the Fe_3Se_4 crystal structure and the presence of Fe^{2+} ions with a non-zero orbital moment. It was shown in a number of studies that the magnetic properties of iron selenide, in particular, the coercivity can be efficiently varied by partial replacement of iron by cobalt,[342] chromium [343] or manganese.[344]

A unique magnetic hardness was also established for compounds with the double perovskite structure containing heavy 5d metals — $La_2Ni_{1.19}Os_{0.81}O_6$ (Ref. 345) and Lu_2NiIrO_6 (Ref. 346). Both compounds were obtained by solid-phase sintering of precursors (La_2O_3, Ni and Os in O_2 atmosphere to prepare the former compound and Lu_2O_3, NiO and IrO_2 at a pressure of 6 GPa to prepare the latter compound). The crystal structures of these two compounds have low symmetry (space group $P2_1/n$). Below the Néel temperature (125 and 207 K, respectively), the materials undergo ferrimagnetic spin ordering because of the antiferromagnetic interaction between Ni^{2+} ions in two sublattices and between Ni^{2+} and 5d metal ions. At 5 K, both compounds have a very high coercivity — 3263 kA m^{-1} (41 kOe) for $La_2Ni_{1.19}Os_{0.81}O_6$ and 3820 kA m^{-1} (48 kOe) for Lu_2NiIrO_6; the magnetic moments are 0.65 and 0.52 μ_B per formula unit, respectively. The giant coercivity of these materials was attributed to the presence of heavy 5d metal (Os and Ir) with a non-zero orbital moment and low crystal lattice symmetry. It was also assumed that the coercivity of these compounds is affected by the crystallographic disorder of 5d metal ions.

8. Low-dimensional magnets

This part of the review addresses vivid examples of magnetic materials with giant magnetic hardness in which the para-

magnetic ions are not connected *via* a continuous three-dimensional network of exchange interactions, but exist in the isolated or quasi-isolated state with different topologies. The first class of these materials are single-ion (SIMs) and single-molecule (SMMs) magnets in which the paramagnetic centres are completely isolated from one another. The second class is formed by single-chain magnets, in which the exchange-coupled paramagnetic ions form chains. One more class of materials is formed by layered magnets in which the exchange-coupled paramagnetic ions are arranged into layers, which are connected by weaker chemical bonds.

8.1. Single-ion and single-molecule magnets

Single-ion and single-molecule magnets differ from other magnetic materials in that their macroscopic magnetization is not due to the exchange interaction, but appears as a result of co-directional magnetization of a group of single magnetic ions not interacting with one another (in the case of SIMs) or magnetically coupled small clusters (in the case of SMMs). As a rule, each of these ions is characterized by an energetically favourable orientation of the magnetic moments arising due to the spin–orbit coupling. Therefore the presence of an ion with a non-zero orbital moment is, almost in all cases, a necessary condition for the formation of SIMs. The magnetization reversal of SIM magnetic centre and demagnetization of the material are hampered by the necessity of overcoming an energy barrier that separates the two most favourable states along the easy magnetization axis. The orbital moment of the 3d transition elements in chemical compounds is usually frozen; however, its contribution can be significant in a highly anisotropic crystal field. A linear environment is optimal. The crystal field generated by this environment may substantially increase the energy barrier for magnetization reversal; this applies to not only magnetic 3d metal ions, but also lanthanide ions, which always have an orbital magnetic moment. In very rare cases and when certain conditions are met, slow magnetization relaxation for paramagnetic compounds containing ions without an orbital moment is possible. There are known gadolinium complexes with zero orbital moment that are able to maintain magnetization for more than a second at helium temperatures, merely because of the very weak interaction of the magnetic ion with the lattice and actual absence of an effective magnetization relaxation mechanism.[347, 348] However, these examples are rather exceptions; temperatures at which magnetization is retained do not exceed 18 K. In the vast majority of cases, the retention of magnetization in SIMs is associated with the orbital moment.

An increase in temperature facilitates overcoming of the energy barrier. As a rule, in SIMs, temperature increase results in an exponential shortening of the characteristic relaxation time (the time during which magnetization in a particular direction is retained), which brings about a narrowing of the hysteresis loop and a decrease in the coercivity. Meanwhile, at low temperatures, there is a possibility of magnetization reversal without overcoming the energy barrier *via* quantum tunnelling, which also decreases the coercivity. The tunnelling efficiency is significantly reduced when even a small magnetic field is applied; therefore, a butterfly-shaped hysteresis loop is often observed for SIMs. In addition, tunnelling can be considerably suppressed by binding magnetic ions into pairs[349] or by diamagnetic dilution of the material, which reduces the dipole–dipole interaction between the magnetic ions.[350] Single-ion magnets show hysteresis in a limited temperature range (currently, the highest temperature is ~80 K).[351] At low temperatures, SIMs can have rather high coercivity, up to 8754 kA m^{-1} (110 kOe).[352]

Thus, for obtaining SIMs, it is necessary to generate an ensemble of isolated paramagnetic ions in a highly anisotropic coordination (preferably linear) and to have a possibility to level-off the effect of side magnetization reversal processes (first of all, tunnelling). There are several approaches to create such conditions.

The most popular method for the fabrication of SIMs is the organometallic pathway: the preparation of complexes of magnetic ions with bulky branched organic ligands, which make it possible to implement a nearly linear coordination and a low coordination number. The two most successful representatives of this group are dysprosocene[351, 353, 354] and pentagonal-bipyramidal complexes of dysprosium with D_{5h} geometry.[355, 356] Dysprosocene is a sandwich complex of dysprosium with two cyclopentadienyl (Cp) rings, which generate a strong axial crystal field. The introduction of bulky substituents into the cyclopentadienyl rings increases the steric repulsion between the coordinating ligands and brings the Cp–Dy–Cp angle closer to 180°. The best complex has an energy barrier for magnetization reversal of 1541 cm^{-1} and shows a hysteresis up to 80 K. When the magnetic field sweep rate† is 15.92 kA m^{-1} s^{-1} (200 Oe s^{-1}), the coercivity is 1592 kA m^{-1} (20 kOe) at 65 K and 3979 kA m^{-1} (50 kOe) at 2 K (Fig. 33).[351]

The introduction of various substituents into the cyclopentadienyl rings not only brings the coordination closer to linear, but also changes the vibrational spectrum of the molecule. It turns out that phonons with definite energies, the presence of which is undesirable, play a considerable role in magnetization reversal.[357, 358] Thus, complexes with similar barriers for magnetization reversal may differ in the coercivity and in the maximum temperature of hysteresis, in view of different roles of side magnetization reversal processes. In the above example, the absence of protons bound

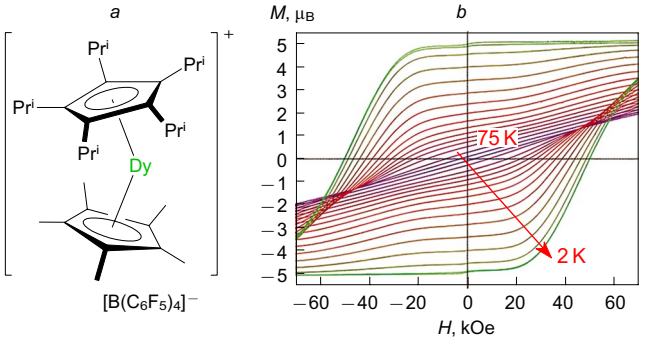


Figure 33. Structural formula of dysprosocene [(Cp^{5Pri})Dy(Cp^{5Me})][B(C$_6$F$_5$)$_4$] (*a*) and magnetization *vs.* field dependences for this complex at $T = 2–75$ K and at sweep rate of 200 Oe s^{-1} (*b*).[351] Published with permission from the American Association for the Advancement of Science.

† Note that due to the relatively short relaxation times of the magnetic moments in the low-dimensional magnets, the measured coercivity values are, most often, considerably depend on the magnetic field sweep rate. Therefore, whenever possible, the coercivity values are given together with the sweep rate.

to the cyclopentadienyl rings (that could have generated undesirable vibrations) was, apparently, very important. It was shown [359] that the replacement of the cyclopentadienyl rings by cyclobutadienyl ones results in an even stronger crystal field, and other currently record-high magnetic characteristics could be improved; however, the sandwich complex of dysprosium with cyclobutadienyl has not yet been obtained.

Lanthanide dimers ferromagnetically and chemically coupled *via* the N_2^{3-} radical group can be used to create SIMs for which the role of tunnelling is minimized.[360] These systems may give rise to very wide hysteresis loops with giant coercivity for moderate energy barriers. For example, for a compound of this class containing a $Tb_2(\mu\text{-}N_2)$ moiety, the field dependence of magnetization shows a hysteresis up to 20 K, with the spin reversal barrier being 276 cm^{-1}. At 10 K, the coercivity of this compound is 6287 kA m^{-1} (79 kOe) [the sweep rate is 7.96 kA m^{-1} s^{-1} (100 Oe s^{-1})].

Using organometallic synthesis, it is possible to obtain SIMs based on not only lanthanides, but also 3d transition metals. The most 'outstanding' SIMs based on 3d transition metals are linear iron [361] and cobalt [362] complexes like $M(C\{Si(CH_3)_3\}_3)_2$. The cobalt(II) complex has a spin reversal barrier of 450 cm^{-1} and hysteresis up to 5 K. The coercivity of this complex is moderate due to tunnelling; however, by diamagnetic dilution, it can be increased to ~1 kOe (~80 kA m^{-1}) [field sweep rate of 2.55 kA m^{-1} s^{-1} (32 Oe s^{-1})]. Iron(I) complex has a spin reversal barrier of 226 cm^{-1} and shows hysteresis up to 4.5 K (though also with significant tunnelling and, hence, low coercivity).

One more method for isolating magnetic ions and forming a linear environment for them is to use endofullerenes with lanthanide ions (Fig. 34).[363] Both lanthanide ions themselves and more complex groups such as Dy_2O, Dy_2S, Dy_2C_2 and Dy_3N can be incorporated into fullerene molecules. The use of different fullerenes makes it possible to change the M–X–M angle and thus to bring the coordination closer to the linear geometry. For example, the use of fullerene C_{74} instead of C_{72} (Ref. 364) increased the Dy–O–Dy angle from 138 to 172°; therefore, the temperature at which hysteresis was observed increased from 8 to 14 K. A good illustration for the possibility of affecting the tunnelling efficiency is the endofullerene with an embedded M_3N moiety.[365] In the case of $DySc_2N@C_{80}$-I_h with one paramagnetic ion per formula unit, the role of tunnelling was significant, which gave rise to a wide butterfly-shaped hysteresis loop and a nearly zero coercivity. However, in the case of two dysprosium atoms ($Dy_2ScN@C_{80}$-I_h), the tunnelling effect was virtually suppressed and a hysteresis loop with a coercivity of ~796 kA m^{-1} (10 kOe) was obtained at a sweep rate of 8 Oe s^{-1} (see Fig. 34). Currently, the highest temperature at which hysteresis can be observed for endofullerenes is ~20 K.[366]

One more approach to obtain SIMs is to use an inorganic crystal as a matrix for embedding isolated magnetic ions with non-zero orbital moments.[367] The most extensive group obtained by this approach are SIMs with the apatite structure (Fig. 35). Both linear (or nearly linear) transition metal oxo anions (O–M–O) and lanthanide ions, which form LnO^+ oxo cations with a strong axial crystal field in the lattice, can be embedded into an apatite structure. For example, apatite type barium phosphates containing angular $[OCoO]^{2-}$ anions have a considerable barrier for magnetization reversal (up to 387 cm^{-1}) and a

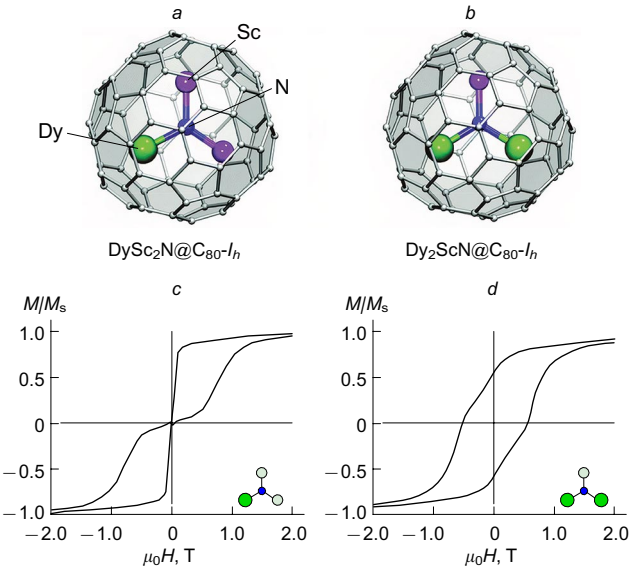


Figure 34. Structure of endofullerenes $M_3N@C_{80}$-I_h (*a*, *b*) and magnetization *vs.* field dependences for endofullerenes containing one (*c*) and two dysprosium atoms (*d*).[363,365] The measurement temperature is 2 K and the sweep rate is 8 Oe s^{-1}. M/M_s is the magnetization of the compound normalized to the saturation magnetization. Published with permission from the Royal Society of Chemistry and the American Physical Society.

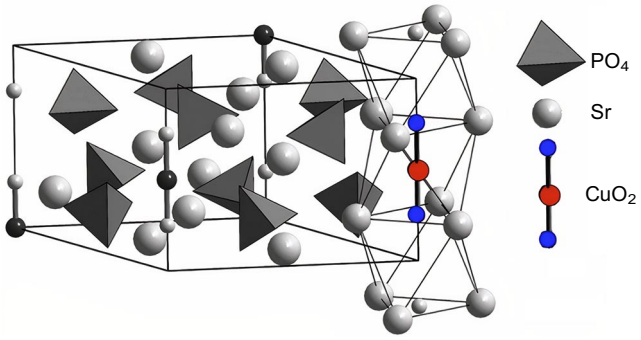


Figure 35. Structure of the apatite with incorporated O–Cu–O group.[367] Published with permission from Wiley.

narrow hysteresis loop in the magnetization curve.[368] Dysprosium-doped strontium phosphates demonstrate a barrier for magnetization reversal of up to 1043 cm^{-1} and a broad hysteresis loop.[369] However, due to the significant contribution of tunnelling, the hysteresis loop for all apatite type compounds has a butterfly shape, *i.e.*, the coercivity proves to be moderate. Nevertheless, in view of rather high energy barriers for magnetization reversal, typical of these compounds, which in some cases exceed 1000 cm^{-1}, and the possibility of increasing the coercivity by suppression of tunnelling (like in other SIMs), one can hope that high coercivity values would be attained for them.

One more convenient inorganic matrix for incorporation of 3d transition metal ions into a linear environment is lithium nitride. When iron ions are incorporated into the lithium sites, they get in a linear coordination by nitrogen atoms (Fig. 36), which gives rise to a strong axial crystal field and a considerable orbital moment.[352] As a result, a SIM with a butterfly-shaped hysteresis loop recorded up to 10 K can be obtained for $Li_{2.9968}Fe_{0.0032}N$ with a low degree

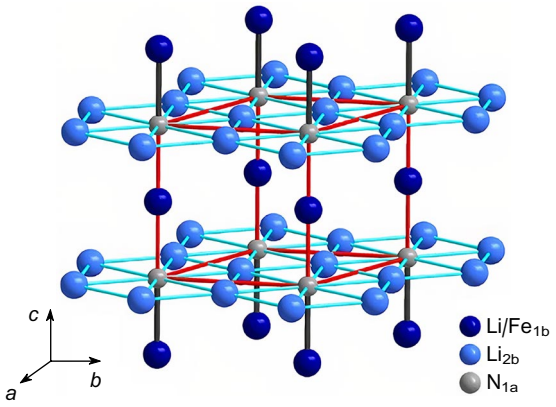


Figure 36. Structure of $Li_{3-x}Fe_xN$.[352] Published with permission from Springer Nature.

of substitution. Despite the fact that a strong decrease in the magnetization takes place in a zero field, the loop does not completely collapse, and the sample has a coercivity of up to 3183 kA m^{-1} (40 kOe) at 8 K [for a sweep rate of 0.12 kA m^{-1} s^{-1} (1.5 Oe s^{-1})]. An increase in the iron concentration results, apparently, in exchange interaction between the iron atoms; simultaneously, the steps in the hysteresis loop disappear and the loop acquires a conventional smooth shape. The strong axial crystal field and high orbital moment bring about a very high magnetic anisotropy field — 175 MA m^{-1} (2200 kOe). As a result, a coercivity of 9231 kA m^{-1} (116 kOe) is observed at 2 K and at a sweep rate of 0.12 kA m^{-1} s^{-1} (1.5 Oe s^{-1}). The hysteresis exists up to ~50 K. Cobalt in $LiSr_2[CoN_2]$ with a similar linear coordination is also characterized by ferromagnetic ordering at temperatures below 44 K, with the coercivity being ~239 kA m^{-1} (3 kOe) at 2 K.[370]

Logically, the idea of generation of an ideal axial crystal field and increasing the orbital moment can culminate in so-called single-atom magnets — single magnetic atoms deposited on a non-magnetic substrate. For example, single atoms of cobalt[371] and holmium[372] on MgO substrate were obtained and studied. The holmium-based sample showed a coercivity of ~796 kA m^{-1} (~10 kOe) at 2 K and even demonstrated the possibility of writing and erasing information on single atoms.[373] However, the use of such systems is limited due to the substantial mobility of the atoms at higher (> 50 K) temperature.

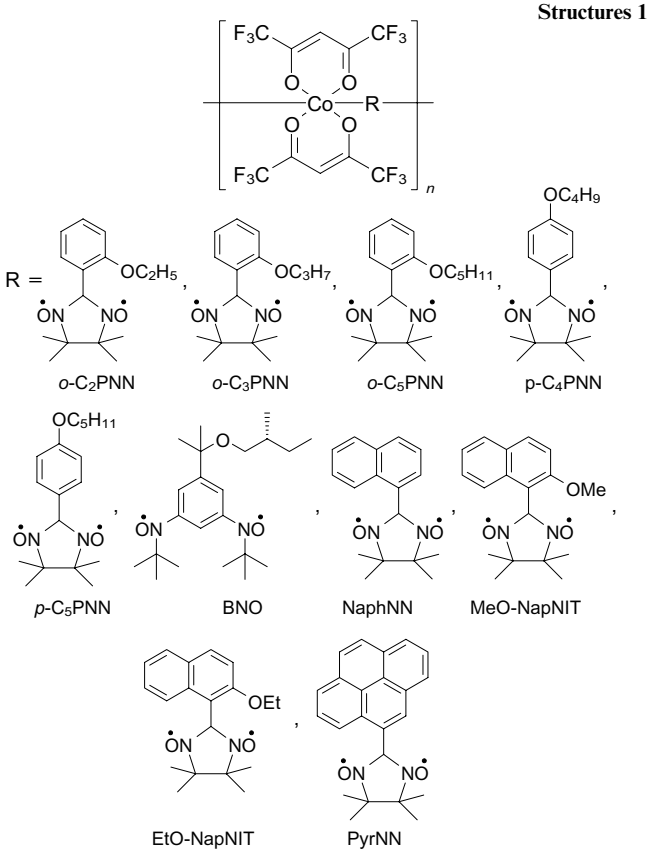
8.2. Single-chain magnets

Unlike SIMs and SMMs described above, single-chain and layered magnets are characterized by both conventional (ferro- and ferrimagnetism, collinear and canted antiferromagnetism) and exotic (spin liquid, spin glass or spin ice) types of ordering of the magnetic subsystem. A specific feature of such magnets is the clear-cut short-range correlations between the directions of magnetic moments that may be manifested at temperatures substantially exceeding the magnetic ordering temperature. These correlations, together with other intrinsic factors (crystal field, single-ion anisotropy, dipole–dipole interaction), particle morphology and domain structure of the material[374] may give rise to high magnetic anisotropy and coercivity (several tens of kOe).[375]

Compounds [Mn^{III}(Porph)][TCNE] (where Porph is porphyrin, TCNE is tetracyanoethylene) are the first representatives of single-chain magnets with a giant coercivity.[376] In these materials, Mn^{3+} ions are located in octahedra, each being formed by four nitrogen atoms of porphyrin molecules and two nitrogen atoms of tetracyanoethylene molecules. These octahedra, connected by tetracyanoethylene molecules, form a chain. Compounds of this group, being canted antiferromagnets, exhibit spontaneous magnetization below the Néel temperature $T_N \approx 10$ K. Under the action of an external magnetic field slightly lower than the coercivity, this material is transformed into the metamagnetic state. Giant coercivity values ranging from 1592 kA m^{-1} (20 kOe) to 2149 kA m^{-1} (27 kOe) were detected for these compounds at 2 K. The Mn^{3+} single-ion anisotropy and dipole–dipole interaction are considered to be responsible for high H_c values.

Numata *et al.*[377] proposed for the first time the organometallic cobalt precursor Co^{II}(hfac)$_2 \cdot 2H_2O$, where hfac is 1,1,1,5,5,5-hexafluoroacetylacetone, to prepare molecular single-chain magnets with an extremely high magnetic hardness. A soluble precursor of so-called radical ligand, the function of which is to cross-link the Co(hfac)$_2$ moieties to form a chain, was added to a solution of Co(hfac)$_2 \cdot 2H_2O$. As this was done, the crystals of the final product precipitated from the solution. This approach proved to be fairly efficient; subsequently, about a dozen of single-chain magnets [Co^{II}(hfac)$_2$(R)]$_n$ were prepared using various radical ligands (structures **1**, the unit complexes are connected at the oxygen radical). The coercivities of these products exceeded 1592 kA m^{-1} (20 kOe).[378–383] The chains were formed by CoO_6 octahedra connected by the radical ligands. These chains were packed into a three-dimensional low-symmetry crystal structure. The nature of the radical ligand determines the bond angle between the ligand and the paramagnetic ion. This angle affects the long- and short-

Structures 1



range magnetic structure and the magnetic anisotropy of the compound.

Depending on the temperature and the external magnetic field strength, these compounds can be in a paramagnetic, antiferromagnetic, canted antiferromagnetic or ferrimagnetic state. Figure 37 shows an example of the magnetic order within the chains and between them for $[Co^{II}(hfac)_2(PyrNN)]_n$. The magnetic moments of Co^{2+} ions are ferromagnetically ordered within the chains. The chains themselves are ferromagnetically ordered in one direction and antiferromagnetically ordered in the perpendicular direction, with an easy magnetization axis being formed along the ⟨101⟩ direction. At temperatures below 10 K, compounds $[Co^{II}(hfac)_2(R)]_n$ have very high coercivity, which increases depending on the nature of the substituent R (Table 2).

Liu *et al.*[383] obtained two new hard magnetic compounds $[Co(hfac)_2(R\text{-}NapNIT)]_n$, where R′ = MeO or EtO. According to X-ray diffraction data, both compounds corresponded to the orthorhombic system (space group $P2_12_12_1$). At 7 K and a magnetic field sweep rate of 15.92 kA m^{-1} s^{-1} (200 Oe s^{-1}), they showed giant coercivity of 4934 kA m^{-1} (62 kOe) and 5173 kA m^{-1} (65 kOe), respectively. In the case of

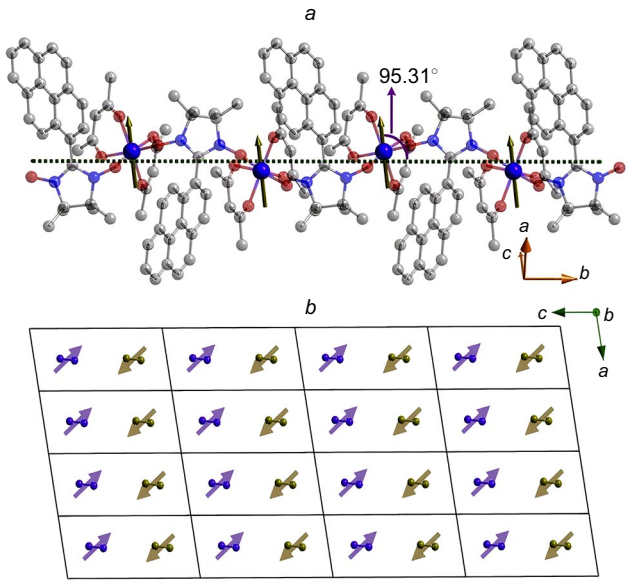


Figure 37. Magnetic ordering of spins within the chains (*a*) and between the chains (*b*) in $[Co^{II}(hfac)_2(PyrNN)]_n$.[383] Published with permission from Wiley.

Table 2. Variation of the coercivity of $[Co^{II}(hfac)_2(R)]$ as a function of the nature of substituent at 2–8 K and at sweep rate of 1.43 kA m^{-1} s^{-1} (18 Oe s^{-1}).

R	H_c, kA m^{-1} (kOe)	Ref.
BNO	1990 (25)	377
PyrNN	2546 (32)	381
NaphNN	3899 (49)	379
o-C_5PNN	3979 (50)	382
o-C_3PNN	4058 (51)	382
p-C_5PNN	4058 (51)	397
p-C_4PNN	4138 (52)	378, 382
o-C_2PNN	4297 (54)	380, 382

$[Co(hfac)_2(EtO\text{-}NapNIT)]_n$, measurement of the hysteresis loop in a pulsed field at 2 K showed a coercivity of 8117 kA m^{-1} (102 kOe) (Fig. 38); currently, it is the record-high value for molecular low-dimensional magnets. The key conclusion drawn by the authors[383] was that the three-dimensional magnetic ordering is not at all a necessary condition for attaining a high coercivity of $[Co^{II}(hfac)_2(R)]_n$: for example, $[Co(hfac)_2(MeO\text{-}NapNIT)]_n$ is ordered, while $[Co(hfac)_2(EtO\text{-}NapNIT)]_n$ is not. The exceptionally high magnetic hardness of both materials was attributed to the effect of ligand crystal field on the direction of the cobalt magnetic moments: the exchange interaction within the chains is ferromagnetic and collinear, but the chains are directed ferro- or antiferromagnetically relative to one another at an angle to the crystallographic axes of the crystals. The magnetic field induces a series of reorientation magnetic transitions, which account for the appearance of a spontaneous magnetic moment and ferrimagnetism, while the strong crystal field generates high energy barriers for these transitions, giving rise to record-high coercivity.

One more class of one-dimensional magnets are materials in which the magnetic chains are formed by metal–oxygen polyhedra and are separated by organic molecules. Guo *et al.*[374] used the solvothermal treatment of an aqueous methanol solution of $Co(NO_3)_2 \cdot 6H_2O$ and $BTPH_2$ [BTP is 4-(3-bromothienyl)phosphonate anion] to obtain ensembles of $[Co_3(\mu_3\text{-}OH)_2(BTP)_2]$ particles. This compound crystallizes in the monoclinic system (space group $P2_1/c$). Below T_N = 30 K, the ferrimagnetic state of the material is caused by antiferromagnetic Co–O–Co interaction in the chains formed by the $(Co1)O_6$ octahedra and the $(Co2)O_4$ tetrahedra along the *c* axis and separated by the $(BTP)^{2-}$ anions (Fig. 39). The authors noted a critical effect of the domain structure on the coercivity of the compound. A decrease in the average particle size from several tens of micrometres to hundreds of nanometres, which is accompanied by the transfer of material from the multi- to single-domain region, leads to coercivity increase from 398 kA m^{-1} (5 kOe) to 1910 kA m^{-1} (24 kOe) at 5 K.

Fully inorganic compounds in which metal–oxide or metal–hydroxide chains are isolated from one another by inorganic ions or molecules can be assigned to a separate class of single-chain magnets. Vilminot *et al.*[384] obtained crystals of $K_2Co_3^{II}(OH)_2(SO_4)_3(H_2O)_2$ by hydrothermal treatment of a solution of $Co(SO_4)_3 \cdot 7H_2O$, K_2SO_4 and KOH. According to X-ray diffraction data, this compound crystallizes in the orthorhombic system (space group *Cmc*2, unit cell parameters: *a* = 17.8638, *b* = 7.5480,

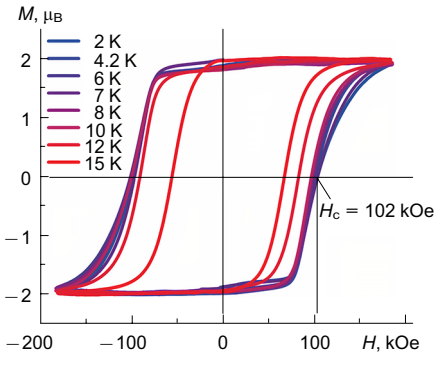


Figure 38. Magnetic hysteresis loops for $[Co(hfac)_2(EtO\text{-}NapNIT)]_n$ measured in the pulsed magnetic field at 2–15 K at a field sweep rate of 344.57 kA m^{-1} s^{-1} (4330 kOe s^{-1}).[383] Published with permission from Wiley.

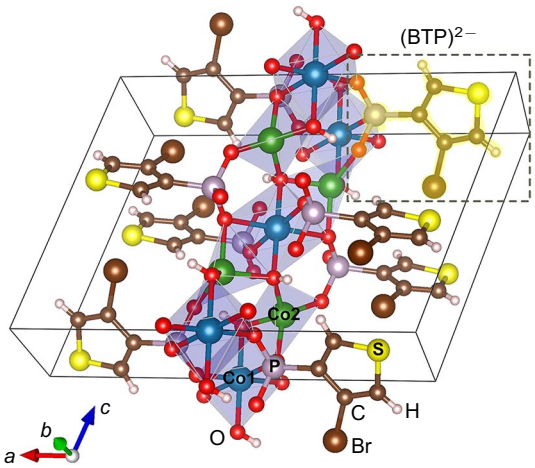


Figure 39. Unit cell of the one-dimensional magnet $[Co_3(\mu_3\text{-}OH)_2(BTP)_2]$. The figure was created by the authors using data of Ref. 374.

c = 9.7506 Å). The cobalt ions are located in two CoO_6 octahedra, which form zigzag type chains along the c axis (Fig. 40 *a*). Below 30 K, this material switches from the paramagnetic to ferrimagnetic state. This is due to the antiferromagnetic interaction between the cobalt ion in the chains (see Fig. 40 *b*). For a polycrystalline sample of $K_2Co_3^{II}(OH)_2(SO_4)_3(H_2O)_2$, the coercivity reaches 2546 kA m^{-1} (32 kOe) at 2 K. In the case of a single crystal at 1.8 K, the material magnetization along the easy (a axis) and intermediate (b axis) axes corresponds to the coercivity of 2387 kA m^{-1} (30 kOe) and 3740 kA m^{-1} (47 kOe), respectively. Magnetization along the hard axis (c axis) does not lead to saturation even at 5570 kA m^{-1} (70 kOe), which attests to a higher anisotropy field of this compound.

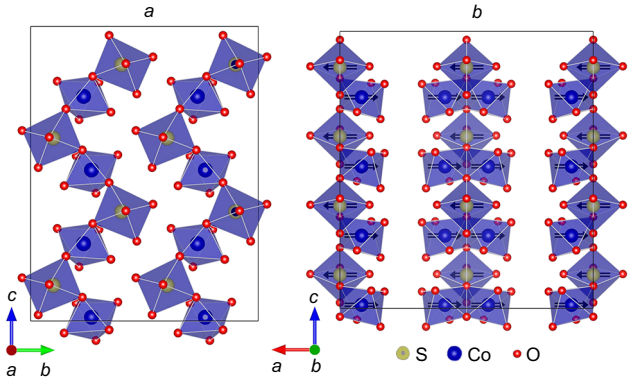


Figure 40. Ordering of the CoO_6 octahedra into chains in $K_2Co_3^{II}(OH)_2(SO_4)_3(H_2O)_2$ (*a*) and magnetic structure of this compound (*b*). The figure was created by the authors using data of Ref. 384.

8.3. Layered magnets

The crystal structure of layered magnets is represented by layers of connected coordination polyhedra of the paramagnetic metal ion separated by molecules or polyatomic ions (Fig. 41). Compounds of this class are few in number. The first layered magnet with a giant coercivity was obtained by Kurmoo.[385] Heating and subsequent evaporation of an aqueous ethanol solution of cobalt nitrate, terephthalic acid and ammonium hydroxide afforded the

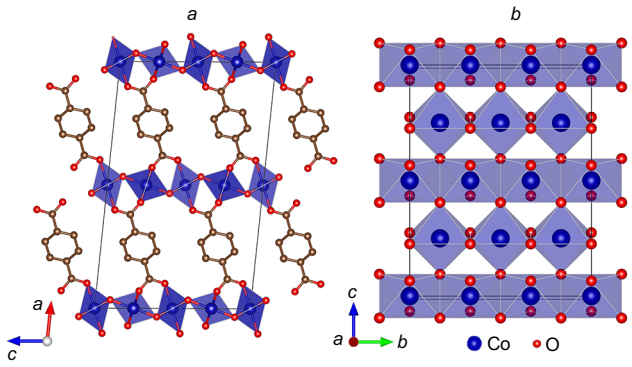


Figure 41. Crystal structure of layered magnets exemplified by cobalt(II) hydroxy terephthalate. (*a*) packing of $Co(OH)_2$ layers with terephthalate anions (side view), (*b*) fragment of one $Co(OH)_2$ layer (top view). The figure was created by the authors using data of Ref. 387.

compound $Co_4(OH)_2(C_8H_4O_4)_3(NH_3)_{1.5}(H_2O)_{2.5}$. Analysis of X-ray diffraction data provided the hypothesis that the crystal structure of this product is, most likely, similar to either the monoclinic structure of $Zn_5(OH)_8(H_2O)_2(NO_3)_2$ or the hexagonal structure of $Zn_5(OH)_8Cl_2 \cdot H_2O$. In all probability, the cobalt ions in $Co_4(OH)_2(C_8H_4O_4)_3(NH_3)_{1.5}(H_2O)_{2.5}$ occur in the CoO_6 octahedra, which form chains. The chains are, in turn, combined into layers separated by terephthalate anions. Below 38 K, the material switches from the paramagnetic to ferrimagnetic state. The coercivity of this compound at 2 K is more than 3979 kA m^{-1} (50 kOe).

Kurmoo *et al.*[386] obtained the layered magnet $Co_2(OH)_2(C_8H_4O_4)$ (where $C_8H_4O_4^{2-}$ is the terephthalate anion). An X-ray diffraction study demonstrated that this compound crystallizes in the monoclinic system (space group $C2/m$, unit cell parameters: a = 19.952, b = 3.286, c = 6.295 Å, β = 95.84°). The crystal structure is represented by two types of chains composed of edge-sharing CoO_6 octahedra. The chains are connected into layers through the oxygen atoms of the OH groups, while the layers, in turn, form a three-dimensional structure *via* terephthalate anions (see Fig. 41 *a*). At temperatures below 48 K, the material is converted from a paramagnet to a collinear antiferromagnet, while on cooling below 44 K, the compound starts to exhibit weak spontaneous magnetization. It was noted[387] that the magnetic subsystem of $Co_2(OH)_2(C_8H_4O_4)$ can exist in three states: plain antiferromagnetic (45–48 K), weakly canted antiferromagnetic (0–45 K) and strongly canted antiferromagnetic (0–45 K; upon the application of a magnetic field), which was also confirmed by neutron diffraction.[388] As the temperature decreases, the hysteresis loop is broadened. According to Huang *et al.*,[387] this is due to a decrease in the occupancy of the excited terms of the electron subsystem of the Co^{2+} ion, which has a large single-ion anisotropy in the ground state; this in turn results in a high magnetocrystalline anisotropy of the material. Due to the high magnetocrystalline anisotropy, $Co_2(OH)_2(C_8H_4O_4)$ shows giant coercivity values — 3979 kA m^{-1} (50 kOe) at 2 K (Ref. 386) and 4695 kA m^{-1} (59 kOe) at 4.2 K.[387]

Kurmoo *et al.*[389] reported the growth of single crystals of the layered magnet $Co_5(OH)_8(chdc) \cdot 4H_2O$ (chdc is *trans*-cyclohexane-1,4-dicarboxylate anion). A solution of a solution of $Co(NO_3)_2 \cdot 6H_2O$ was added to a solution

containing a mixture of *cis*- and *trans*-cyclohexane-1,4-dicarboxylic, barbituric acid and NaOH until a blue amorphous precipitate formed. The final suspension was subjected to hydrothermal treatment. The obtained product crystallized, most likely, in the orthorhombic system (space group *Imma*). The structure of this compound is formed by layers composed of connected octahedra and tetrahedra — $Co_3^{(окт)}Co_2^{(тетр)}(OH)_8$. The layers are linked by chdc anions. At temperatures below 60 K, this material switches from the paramagnetic to ferrimagnetic state. The magnetic moment of the cobalt ions in the octahedral sublattice is directed oppositely to that of the cobalt ions in the tetrahedral sublattice; both magnetic moments are parallel to the plane of the layer. Measurement of the magnetic hysteresis of the oriented crystallites along the easy magnetization axis (parallel to the plane of the layers) showed that the coercivity of this compound at 2 K amounts to 1751 kA m^{-1} (22 kOe).

9. Conclusion

Great progress has been achieved in recent years in the studies of compounds and materials in which no magnetization reversal takes place in exceptionally strong magnetic fields. The progress concerned both advancement of conventional materials for permanent magnets and development of new classes of high-coercivity magnets. In addition to the desired magnetic characteristics, other aspects are also important for practical use, *e.g.*, the cost and availability of the starting materials, scalability of the manufacturing process, chemical and thermal stability, electrical and optical properties and the possibility of obtaining material as nanoparticles, thin films, nanocomposites or dense bulk products.

In the foreseeable future, rare earth metal compounds would apparently play the key role in the production of high-energy permanent magnets needed for the manufacture of powerful electric motors and electric generators. Rare earth-based magnets show high $(BH)_{max}$ both at room temperature (Nd–Fe–B) and at elevated temperatures (Sm–Co). Currently, understanding of the mechanisms of chemical and physical processes in rare earth metal magnets has reached a high level; however, the potential for in-depth studies has not yet been exhausted. Further enhancement of the magnetic characteristics of these materials would require more efficient nanostructuring methods. High cost of lanthanides (especially Dy and Tb) necessitates the development of materials with lower lanthanide contents, optimization of lanthanide distribution in the magnet bulk; in addition, recycling processes deserve attention.

This accounts for the interest in other intermetallics containing no rare earth metal compounds. Regarding the $(BH)_{max}$ values, they are still considerably inferior to rare earth metal compounds, but, in return, they can be obtained as monodisperse nanoparticles (FePt) or thin films (FePt and MnGa) with giant coercivity. The characteristics attained for promising low-cost MnAl and MnBi are still markedly lower than the theoretical characteristics, but in the future, they may become competitive with the rare earth metal-based magnets.

Ferrites with giant coercivity are characterized by low magnetization, but they instead possess high chemical stability and show a specific absorption of radiation in the subterahertz frequency range (100–250 GHz), which may be promising for next-generation 5G and 6G wireless technologies. An ultrahigh magnetic hardness with very small particle size was found for ε-Fe_2O_3; however, the industrial implementation of this material is hampered by the absence of scalable process of synthesis. Recently, giant coercivity was discovered for substituted hexaferrites, which makes them more promising, since there are already simple methods for their synthesis in the form of dense ceramics and nano-sized particles.

Studies of low-dimensional magnets as simpler models and hard magnetic materials based on 5d metals provides a better understanding of the nature of magnetic anisotropy, which would help, in the future, to develop new magnetic materials with unprecedented and unique properties. The use of single molecules of low-dimensional magnets in the bottom-up chemical assembly techniques would allow the design of miniature magnetic devices promising for new generation spintronics.

This review was written with the financial support of the Russian Foundation for Basic Research (Project No. 19-13-50430).

10. List of acronyms and designations

B — magnetic induction,
B_r — residual induction,
B_s — saturation induction,
$(BH)_{max}$ — maximum energy product,
E_a — anisotropy energy,
H — magnetic field strength,
H_a — anisotropy field,
H_c — coercivity,
H_d — demagnetizing field,
K_1 — uniaxial magnetocrystalline anisotropy constant,
M — magnetization,
M_r — remanent magnetization,
M_v — volume magnetization,
M_s — mass saturation magnetization,
M_{sv} — volume saturation magnetization,
μ — magnetic moment,
N — demagnetization factor,
T_C — Curie temperature,
T_N — Néel temperature,
T_s — deposition temperature,
MCA — magnetocrystalline anisotropy,
SMM — single-molecule magnet,
SIM — single-ion magnet,
ρ — density of the material.

References

1. K.Kojima. *Handbook Magn. Mater.*, **3**, 305 (1982)
2. K.M.Krishnan. *Fundamentals and Applications of Magnetic Materials*. (Oxford: Oxford University Press, 2016)
3. J.Smit, H.P.J.Wijn. *Ferrites*. (Eindhoven; Philips Technical Library, 1959)
4. J.J.Went, G.W.Rathenau, E.W.Gorter, G.W.van Oosterhout. *Philips Techn. Rev.*, **13**, 194 (1952)
5. R.C.Pullar. *Prog. Mater. Sci.*, **57**, 1191 (2012)
6. H.Li, J.M.D.Coey. *Handbook Magn. Mater.*, **28**, 87 (2019)
7. J.M.D.Coey. *Scr. Mater.*, **67**, 524 (2012)
8. J.M.D.Coey. *Engineering*, **6**, 119 (2020)
9. J.M.D.Coey. *Magnetism and Magnetic Materials*. (Cambridge: Cambridge University Press, 2009)

10. U.Enz. In *Ferromagnetic Materials. Vol. 3*. (Ed. E.P.Wohlfarth). (Amsterdam: North-Holland Publishing Company, 1982). P. 1
11. S.Blundell. *Magnetism in Condensed Matter (Oxford Master Series in Condensed Matter Physics)*. (Oxford: OUP, 2001)
12. R.Skomski, D.J.Sellmyer. *J. Rare Earths*, **27**, 675 (2009)
13. Yu.V.Rakitin, V.T.Kalinnikov. *Covremennaya Magnetokhimiya (Modern Magnetochemistry)*. (St-Pitersburg: Nauka, 1994)
14. M.Getzlaff. *Fundamentals of Magnetism*. (Berlin: Springer, 2008)
15. G.Bertotti. *Hysteresis in Magnetism: for Physicists, Materials Scientists, and Engineers*. (San Diego, CA: Academic Press, 1998)
16. H.Kronmüller, S.Parkin. *Handbook of Magnetism and Advanced Magnetic Materials*. (New York: Wiley, 2007)
17. M.D.Kuz'min, A.M.Tishin. *Handbook Magn. Mater*., **17**, 149 (2007)
18. L.D.Landau, E.M.Lifshitz. *Course of Theoretical Physics. Statistical Physics*. Vol. 9 (Moscow: Nauka, 1978)
19. V.I.Marchenko. *Zh. Eksp. Teoret. Fiz*., **72**, 2324 (1977)
20. S.O.Gladkov, S.B.Bogdanova. *Phys. Solid State*, **57**, 929 (2015)
21. W.F.Brown. *Rev. Mod. Phys*., **17**, 15 (1945)
22. M.Yamanouchi, A.Jander, P.Dhagat, S.Ikeda, H.Ohno. *IEEE Magn. Lett*., **2**, 3000304 (2011)
23. L.Půst, G.Bertotti, I.Tomáš, G.Vértesy. *Phys. Rev. B*, **54**, 262 (1996)
24. S.Hirosawa, K.Tokuhara, Y.Matsuura, H.Yamamoto, S.Fujimura, M.Sagawa. *J. Magn. Magn. Mater*., **61**, 363 (1986)
25. E.C.Stoner, E.P.Wohlfarth. *Philos. Trans. R. Soc. London, Ser. A*, **240**, 599 (1948)
26. H.Pfeiffer. *Phys. Status Solidi*, **118**, 295 (1990)
27. G.Martinek, H.Kronmuller. *J. Magn. Magn. Mater*., **86**, 177 (1990)
28. T.Schrefl, H.F.Schmidts, J.Fidler, H.Kronmiiller. *J. Magn. Magn. Mater*., **124**, 251 (1993)
29. P.Déjardin. *J. Appl. Phys*., **110**, 113921 (2011)
30. Q.Gong, M.Yi, R.F.L.Evans, O.Gutfleisch, B.Xu. *Mater. Res. Lett*., **8**, 89 (2020)
31. V.I.Petinov. *Zh. Tekhn. Fiz*. **84**, 8 (2014)
32. H.Moriya, H.Tsuchiura, A.Sakuma. *J. Appl. Phys*., **105**, 07A740 (2009)
33. D.I.Paul, A.Cresswell. *Phys. Rev. B*, **48**, 3803 (1993)
34. M.E.Schabes. *J. Appl. Phys*., **69**, 67 (1991)
35. W.Scholz, D.Suess, T.Schrefl, J.Fidler, W.Scholz, D.Suess, T.Schrefl, J.Fidler. *J. Appl. Phys*., **95**, 6807 (2004)
36. S.P.Gubin, Y.A.Koksharov, G.B.Khomutov, G.Y.Yurkov. *Russ. Chem. Rev*., **74**, 489 (2005)
37. A.P.Guimarães. *Principles of Nanomagnetism*. (Berlin, Heidelberg: Springer, 2009)
38. G.Zhao, X.Zhang, F.Morvan. *Rev. Nanosci. Nanotechnol*., **4**, 1 (2015)
39. G.P.Zhao, L.Zhao, L.C.Shen, J.Zou, L.Qiu. *Chin. Phys. B*, **28**, 077505 (2019)
40. R.Fischer, T.Leineweber, H.Kronmu. *Phys. Rev. B*, **57**, 10723 (1998)
41. H.Kronmuller, K.-D.Durst, M.Sagawa. *J. Magn. Magn. Mater*., **74**, 291 (1988)
42. D.Chen, J.A.Brug, R.B.Goldfarb, S. Member. *IEEE Trans. Magn*., **27**, 3601 (1991)
43. R.Skomski, J.M.D.Coey. *Permanent Magnetism*. (London: Institute of Physics Publishing, 1999)
44. F.Ott, I.Panagiotopoulos, E.Anagnostopoulou, M.Pousthomis, L.-M.Lacroix, G.Viau, J.-Y.Piquemal. In *Magnetic Nano- and Microwires: Design, Synthesis, Properties and Applications (Woodhead Publishing Series in Electronic and Optical Materials)*. (Ed. M.Vazquez). (Cambridge: Woodhead Publishing, 2015). P. 629
45. R.Skomski, J.M.D.Coey. *Scr. Mater*., **112**, 3 (2016)
46. H.Sepehri-Àmin, S.Hirosawa, K.Hono. *Handbook Magn. Mater*., **27**, 269 (2018)
47. H.Sepehri-Amin, T.Ohkubo, T.Shima, K.Hono. *Acta Mater*., **60**, 819 (2012)
48. Y.Matsuura. *J. Magn. Magn. Mater*., **303**, 344 (2006)
49. M.D.Kuz, D.Givord, V.Skumryev. *J. Appl. Phys*., **107**, 4 (2015)
50. M.D.Kuz'min. *Phys. Rev. B*, **51**, 8904 (1995)
51. D.Haskel, J.C.Lang, Z.Islam, A.Cady, G.Srajer, M.Van Veenendaal, P.C.Canfield. *Phys. Rev. Lett*., **95**, 217207 (2005)
52. P.Chen, C.Yang, S.Chang, M.Lee, N.Tang, S.Yen, Y.Tseng. *J. Magn. Magn. Mater*., **370**, 45 (2014)
53. N.V.Mushnikov, P.B.Terent'ev, E.V.Rozenfel'd. *Phys Met Metallogr*., **103**, 39 (2007)
54. P.Wolfers, M.Bacmann, D.Fruchart. *J. Alloys Compd*., **317** – **318**, 39 (2001)
55. W.Yang, D.Liang, X.Kong. *Rare Met*., **39**, 13 (2020)
56. J.F.Herbst, J.J.Croat, W.B.Yelon, J.F.Herbst. *J. Appl. Phys*., **57**, 4086 (1985)
57. J.Sugiyama, K.Miwa, H.Nozaki, Y.Kaneko, B.Hitti, D.Arseneau, G.D.Morris, E.J. Ansaldo, J.H.Brewer. *Phys. Rev. Mater*., **3**, 101401 (2019)
58. R.Coehoorn. In *Supermagnets, Hard Magnetic Materials*. (Dordrecht: Springer-Verlag, 1991). P. 133
59. J.Fidler, T.Schrefl, S.Hoefinger, M.Hajduga. *J. Phys.: Condens. Matter*, **16**, S455 (2004)
60. W.F.Li, T.Ohkubo, K.Hono. *Acta Mater*., **57**, 1337 (2009)
61. P.G.Min, V.E.Fadeev, V.P.Piskorskii, V.V.Kramer. *Trudy VIAM*, **1**, 3 (2016)
62. T.T.Sasaki, T.Ohkubo, K.Hono. *Acta Mater*., **115**, 269 (2016)
63. R.K.Mishra, J.K.Chen, G.Thomas. *J. Appl. Phys*., **59**, 19 (1986)
64. W.Szmaja. *J. Magn. Magn. Mater*., **301**, 546 (2006)
65. K.Hono. *Scr. Mater*., **67**, 530 (2012)
66. H.Kato, T.Miyazaki, M.Sagawa, K.Koyama. *Appl. Phys. Lett*., **84**, 2012 (2004)
67. J.Li, X.Tang, H.Sepehri-Amin, T.T.Sasaki, T.Ohkubo, K.Hono. *Acta Mater*., **187**, 66 (2020)
68. J.Fidler, T.Schrefl, J.Fidler, T.Schrefl. *J. Appl. Phys*., **79**, 5029 (1996)
69. M.Tang, X.Bao, Y.Zhou, K.Lu, J.Li, X.Gao. *J. Magn. Magn. Mater*., **505**, 166749 (2020)
70. X.Liu, Y.Zhang, P.Zhang, T.Ma, M.Yan, L.Zhao, L.Li. *J. Magn. Magn. Mater*., **486**, 165260 (2019)
71. Z.Wang, J.Ju, J.Wang, W.Yin, R.Chen, M.Li, C.Jin, X.Tang, D.Lee, A.Yan. *Sci. Rep*., **6**, 38335 (2016)
72. K.Hirota, H.Nakamura, T.Minowa, M.Honshima. *IEEE Trans. Magn*., **42**, 2909 (2006)
73. N.Watanabe, H.Umemoto, M.Ishimaru, M.Itakura, M.Nishida, K.Machida. *J. Microscop*., **236**, 104 (2009)
74. K.Skotnicova, P.A.Prokofev, N.B.Kolchugina, G.S.Burkhanov, A.A.Lukin, Y.S.Koshkid, T.Cegan, H.Drulis, T.Romanova, N.A.Dormidontov. *Materials (Basel)*, **12**, 1 (2019)

75. M.W.Lee, J.K.Lee, T.S.Jang. *Arch. Met. Mater.*, **64**, 597 (2019)
76. G.A.Politova, I.S.Tereshina, T.P.Kaminskaya, A.A.Viryus, M.A.Paukov, A.A.Lukin, A.V.Andreev. *J. Phys. Conf. Ser.*, **1236**, 012016 (2019)
77. C.D.Fuerst, E.G.Brewer. *J. Appl. Phys.*, **70**, 6444 (1991)
78. T.Kim, T.T.Sasaki, T.Ohkubo, Y.Takada, A.Kato, Y.Kaneko, K.Hono. *Acta Mater.*, **172**, 139 (2019)
79. K.J.Strnat, R.M.W.Strnat. *J. Magn. Magn. Mater.*, **100**, 38 (1991)
80. T.Akiya, J.Liu, H.Sepehri-amin, T.Ohkubo, K.Hioki, A.Hattori. *Scr. Mater.*, **81**, 48 (2014)
81. K.Tokuhara, H.Yamamoto, S.Fujimura, M.Sagawa. *J. Appl. Phys.*, **61**, 3571 (1987)
82. D.Wu, M.Yue, W.Liu, J.Chen, X.Yi. *Mater. Res. Lett.*, **6**, 255 (2018)
83. G.Ding, S.Liao, J.Di, B.Zheng, S.Guo, R.Chen, A.Yan. *Acta Mater.*, **194**, 547 (2020)
84. A.K.Pathak, M.Khan, K.A.G.Jr, R.W.McCallum, L.Zhou, K.Sun, K.W.Dennis, C.Zhou, F.E.Pinkerton, M.J.Kramer, V.K.Pecharsky. *Adv. Mater.*, **27**, 2663 (2015)
85. E.Girt, K.M.Krishnan, G.Thomas, Z.Altounian. *Appl. Phys. Lett.*, **76**, 1746 (2000)
86. N.G.Akdogan, G.C.Hadjipanayis, D.J.Sellmyer. *Nanotechnology*, **21**, 295705 (2010)
87. V.Swaminathan, P.K.Deheri, S.D.Bhame, R.V.Ramanujan. *Nanoscale*, **5**, 2718 (2013)
88. A.S.Volegov, S.V.Andreev, N.V.Selezneva, I.A.Ryzhikhin, N.V.Kudrevatykh, L.Mädler, I.V.Okulov. *Acta Mater.*, **188**, 733 (2020)
89. J.Fidler, T.Schrefl, S.Hoefinger. *J. Phys. D: Appl. Phys.*, **44**, 44064001 (2011)
90. P.Kerschl, A.Handstein, K.Khlopkov, O.Gutfleisch, D.Eckert, R.Gro, K.Mu. *J. Magn. Magn. Mater.*, **290** – **291**, 420 (2005)
91. E.Lectard, C.H.Allibert, R.Ballou. *J. Appl. Phys.*, **75**, 6277 (1994)
92. S. Zhang, D. Zhao. *Advances in Magnetic Materials: Processing, Properties, and Performance*. (Boca Raton, FL: CRC Press, 2017)
93. H.W.Chang, H.Y.Wang, Y.I.Lee, Y.M. Guo, W.C.Chang, C.C.Shaw. *J. Phys. Chem. Solids*, **136**, 109197 (2020)
94. W.B.Ali, Q.Wu, Z.Ma, L.Cong, M.Yue. *J. Magn. Magn. Mater.*, **499**, 166205 (2020)
95. N.Coroian, V.Klosek, O.Isnard. *J. Alloys Compd.*, **427**, 5 (2007)
96. E.M.T.Velu, R.T.Obermyer, S.G.Sankar, W.E.Wallace. *J. Less-Common Met.*, **148**, 67 (1989)
97. M.F.de Campos, S.A.Romero, F.J.G.Landgraf, F.P.Missell. *J. Phys. Conf. Ser.*, **303**, 1 (2011)
98. H.Chen, Y.Wang, Y.Yao, J.Qu, F.Yun, Y.Li, P.Simon. *Acta Mater.*, **164**, 196 (2019)
99. N.Yu, W.Gao, M.Pan, H.Yang, Q.Wu, P.Zhang. *J. Alloys Compd.*, **818**, 012049 (2020)
100. X.Song, X.Zhou, T.Yuan, J.Wang, M.Yue, T.Ma. *J. Alloys Compd.*, **816**, 152620 (2020)
101. M.Musa, X.Song, X.Zhou, W.Jia, T.Yuan, T.Ma, X.Ren. *J. Alloys Compd.*, **853**, 156974 (2021)
102. H.Tang, M.A.H.Mamakhel, M.Christensen. *J. Mater. Chem. C*, **8**, 10 (2020)
103. N.Poudyal, J.P.Liu. *J. Phys. D: Appl. Phys.*, **46**, 1 (2013)
104. B.Das, R.Choudhary, R.Skomski, B.Balasubramanian, A.K.Pathak, D.Paudyal, D.J.Sellmyer. *Phys. Rev. B*, **100**, 0244419 (2019)
105. *Supermagnets, Hard Magnetic Materials*. (Eds G.J.Long, F.Grandjean). (Amsterdam: Springer-Verlag, 1991)
106. S.Yehia. *AIP Conf. Proc.*, **888**, 8 (2007)
107. D.H.Kim, Y.Zhang, G.C.Hadjipanayis. *J. Magn. Magn. Mater.*, **190**, 302 (1998)
108. T.Saito, D.Nishio-hamane. *Intermetallics*, **107**, 6 (2019)
109. H.Ido, K.Konno, H.Ogata. *J. Appl. Phys.*, **70**, 6128 (1991)
110. C.J.Yang, W.Y.Lee, S.D.Choi. *J. Appl. Phys.*, **75**, 6274 (1994)
111. O.Gutfleisch, K.Mu, K.Khlopkov, M.Wolf, A.Yan, T.Gemming, L.Schultz. *Acta Mater.*, **54**, 997 (2006)
112. J.Fan, Q.Zheng, R.Bao, J.Yi, J.Du. *J. Mater. Sci. Technol.*, **37**, 181 (2020)
113. S.Liu, J.Yang, G.Doyle, G.Potts, G.E.Kuhl. *J. Appl. Phys.*, **87**, 6728 (2000)
114. V.P.Menushenkov. *Gorn. Inform.-analit. Bull.*, (S1), 163 (2007)
115. V.P.Menushenkov, T.A.Sviridova, E.V.Shelekhov, L.M.Belova, A.P.Menushenkov, R.V.Chernikov, V.V.Sidorov, O.V.Grishina. *Solid State Phenomena*, **190**, 204 (2012)
116. O.Gutfleisch, M.Kubis, A.Handstein, K.Müller, L.Schultz. *Appl. Phys. Lett.*, **73**, 3001 (1998)
117. W.A.Wagner. *Master Sci. Thesis*. University Nebraska, 2010; https://lib.ugent.be/catalog/ebk01:4330000001231482 (last access 2.10.2021)
118. M.Kopte, C.Mickel, L.Schultz. *IEEE Trans. Magn.*, **48**, 3599 (2012)
119. S.Co, F.Core, S.Nanomagnets, J.Lim, H.Cho, J.Kim, Y.Cho. *ACS Appl. Mater. Interfaces*, **11**, 26222 (2019)
120. Z.Zhang, X.Song, Y.Qiao, W.Xu, J.Zhang, M.Seyring, M.Rettenmayr. *Nanoscale*, **5**, 2279 (2013)
121. Y.Hirayama, Y.K.Takahashi, S.Hirosawa, K.Hono. *Scr. Mater.*, **138**, 62 (2017)
122. M.Yue, H.Liu, Z.Yin, K.Wei, H.Guan, H.Lin, M.Shen, S.An, Q.Wu, S.Sun. *J. Am. Chem. Soc.*, **142**, 8440 (2020)
123. Y.Dong, T.Zhang, Z.Xia, H.Wang, Z.Ma, X.Liu, W.Xia, J.Michael, D.Coey, C.Jiang. *Nanoscale*, **11**, 16962 (2019)
124. C.H.Chen, S.J.Knutson, Y.Shen, R.A.Wheeler, J.C.Horwath, P.N.Barnes. *Appl. Phys. Lett.*, **99**, 12504 (2011)
125. Y.Ma, Z.Yue, M.Wu, Q.Li, C.Yu. *Nanoscale*, **10**, 10377 (2018)
126. M.Yue, C.Li, Q.Wu, Z.Ma, H.Xu, S.Palaka. *Chem. Eng. J.*, **343**, 1 (2018)
127. J.Lee, T.Hwang, M.K.Kang, H.Cho, J.Kim, N.V.Myung, Y.Choa. *Front. Chem.*, **6**, 00018 (2018)
128. X.Xu, Y.Li, Z.Ma, M.Yue, D.Zhang. *Scr. Mater.*, **178**, 34 (2020)
129. Y.Liu, Y.Yan, M.Zhang, Y.Liang, J.Qu, D.Ji, Y.Xue, X.Jing, W.Han. *Electrochim. Acta*, **249**, 278 (2017)
130. C.Li, Q.Wu, Z.Ma, H.Xu, L.Cong, M.Yue. *J. Mater. Chem. C*, **31**, 8522 (2018)
131. H.Tang, Z.Wang, M.A.H.Mamakhel, M.Dong, M.Christensen. *J. Alloys Compd.*, **816**, 152527 (2019)
132. Z.Ma, T.Zhang, H.Wang. *Rare Met.*, **37**, 1021 (2018)
133. J.Lee, T.Hwang, H.Cho, J.Kim, Y.Choa. *Sci. Rep.*, **8**, 15656 (2018)
134. Z.Ma, J.Liang, W.Ma, L.Cong, Q.Wu, M.Yue. *Nanoscale*, **11**, 12484 (2019)
135. K.Otogawa, T.Asahi. *J. Korean Phys. Soc.*, **72**, 716 (2018)

136. S.Okada, E.Node, K.Takagi, Y.Fujikawa, Y.Enokido. *J. Alloys Compd.*, **804**, 237 (2019)
137. A.Teresiak, M.Kubis, N.Mattern, M.Wolf, W.Gruner, K.-H.Miller. *J. Alloys Compd.*, **292**, 212 (1999)
138. T.Saito. *J. Magn. Magn. Mater.*, **369**, 184 (2014)
139. T.Saito, H.Kitazima. *J. Appl. Phys.*, **111**, 07A716 (2012)
140. M.Katter, J.Wecker, C.Kuhrt, L.Schultz. *J. Magn. Magn. Mater.*, **117**, 419 (1992)
141. K.Takagi, R.Soda, M.Jinno, W.Yamaguchi. *J. Magn. Magn. Mater.*, **506**, 166811 (2020)
142. N.Imaoka, E.Kakimoto, K.Takagi, K.Ozaki, M.Tada, T.Nakagawa, M.Abe. *J. Magn. Magn. Mater.*, **476**, 613 (2019)
143. J.Coey, H.Sun. *J. Magn. Magn. Mater.*, **87**, 251 (1990)
144. K.Kobayashi, T.Iriyama, T.Yamaguchi, H.Kato, Y.Nakagawa. *J. Alloys Compd.*, **193**, 235 (1993)
145. A.A.Popovich, N.G.Razumov, T.A.Popovich. *Scientific and Technical Statements of the St. Petersburg State Polytechnic University*, **3**, 206 (2013)
146. T.Saito, H.Kitazima. *J. Magn. Magn. Mater.*, **323**, 2154 (2011)
147. C.Lu, X.Hong, X.Bao, X.Gao, J.Zhu. *J. Alloys Compd.*, **784**, 980 (2019)
148. K.Takagi, H.Nakayama, K.Ozaki. *J. Magn. Magn. Mater.*, **324**, 2336 (2012)
149. W.Yamaguchi, R.Soda, K.Takagi. *Mater. Trans.*, **60**, 479 (2019)
150. K.Kobayashi, A.Saito, M.Nakamura. *Electr. Eng. Jpn.*, **154**, 863 (2006)
151. Patent US 6334908 B1 (2002)
152. R.Soda, K.Takagi, M.Jinno, W.Yamaguchi, K.Ozaki. *AIP Adv.*, **6**, 115108 (2016)
153. M.Onoue, R.Kobayashi, Y.Mitsui, R.Y.Umetsu, Y.Uwatoko, K.Koyama. *J. Alloys Compd.*, **835**, 155193 (2020)
154. K.Xu, Z.Liu, H.Yu, X.Zhong, H.Zhang. *J. Magn. Magn. Mater.*, **500**, 166383 (2020)
155. H.Chen, J.Zheng, L.Qiao, Y.Ying, L.Jiang, S.Che. *Rare Met.*, **37**, 989 (2018)
156. K.Ohmori, T.Ishikawa. *J. Iron Steel Res. Int.*, **13**, 221 (2006)
157. J.Zheng, S.Tian, K.Liu, W.Cai, Y.Tang, L.Qiao, Y.Ying, W.Li, J.Yu, Y.Liu, S.Che. *AIP Adv.*, **10**, 055119 (2020)
158. X.C.Kou, W.J.Qiang, H.Kronmüller, L.Schultz. *J. Appl. Phys.*, **74**, 6791 (1993)
159. J.Xu, J.Zheng, H.Chen, L.Qiao, Y.Ying, W.Cai, W.Li, J.Yu, M.Lin, S.Che. *J. Rare Earths*, **38**, 1060 (2020)
160. C.Lu, X.Hong, Z.Ding, J.Shi, X.Bao, X.Gao. *J. Magn. Magn. Mater.*, **456**, 6 (2018)
161. M.Matsuura, K.Yamamoto, N.Tezuka, S.Sugimoto. *J. Magn. Magn. Mater.*, **510**, 166943 (2020)
162. W.Yamaguchi, R.Soda, K.Takagi. *J. Magn. Magn. Mater.*, **498**, 166101 (2020)
163. M.Matsuura, T.Shiraiwa, N.Tezuka, S.Sugimoto, T.Shoji, N.Sakuma, K.Haga. *J. Magn. Magn. Mater.*, **452**, 243 (2018)
164. M.Ito, H.Tsunemi. *J. Magn. Magn. Mater.*, **490**, 165471 (2019)
165. S.Okada, K.Takagi, K.Ozaki. *J. Alloys Compd.*, **663**, 872 (2016)
166. Y.B.Yang, J.Z.Wei, X.L.Peng, Y.H.Xia, X.G Chen, R.Wu, H.L.Du, J.Z.Han, C.S.Wang, Y.C.Yang, J.B.Yang. *J. Appl. Phys.*, **115**, 17A721 (2014)
167. J.A.Johnson. *Science*, **363**, 474 (2019)
168. O.Gutfleisch, M.A.Willard, E.Brück, C.H.Chen. *Adv. Mater.*, **23**, 821 (2011)
169. X.Yin, M.Yue, Q.Lu, M.Liu, F.Wang, Y.Qiu, X.Yin, M.Yue, Q.Lu, M.Liu, F.Wang. *Engineering*, **6**, 165 (2020)
170. M.Ali, R.Önal, S.Dewilde, B.Saje, S.Riaño, A.Walton. *Green Chem.*, **22**, 2821 (2020)
171. M.Orefice, K.Binnemans. *Sep. Purif. Technol.*, **258**, 117800 (2021)
172. *Critical and Rare Earth Elements: Recovery from Secondary*. (Ed. A.A.Abhilash). (London, New York: CRC Press, 2019)
173. T.Klemmer, D.Hoydick, H.Okumura, B.Zhang, W.A.Soffa. *Scr. Metall. Mater.*, **33**, 1793 (1995)
174. S.Sun. *Adv. Mater.*, **18**, 393 (2006)
175. L.Zhu, S.Nie, K.Meng, D.Pan, J.Zhao, H.Zheng. *Adv. Mater.*, **24**, 4547 (2012)
176. O.Gutfleisch, J.Lyubina, K.-H.Müller, L.Schultz. *Adv. Eng. Mater.*, **7**, 208 (2005)
177. B.Zhang, W.A.Soffa. *Phys. Status Solidi*, **131**, 707 (1992)
178. N.H.Hai, N.M.Dempsey, M.Veron, M.Verdier, D.Givord. *J. Magn. Magn. Mater.*, **257**, 139 (2003)
179. J.Lyubina, O.Gutfleisch, K.-H.Müller, L.Schultz, N.M.Dempsey. *J. Appl. Phys.*, **95**, 7474 (2004)
180. S.Chen, P.Andre. *Int. J. Nanotechnol.*, **9**, 39 (2012)
181. Y.K.Takahashi, T.O.Seki, K.Hono, T.Shima, K.Takanashi. *J. Appl. Phys.*, **96**, 475 (2004)
182. T.Shima, K.Takanashi, G.Q.Li, S.Ishio. *Mater. Trans.*, **44**, 1508 (2003)
183. R.A.Ristau, K.Barmak, L.H.Lewis, K.R.Coffey, J.K.Howard. CRC Press, *J. Appl. Phys.*, **86**, 4527 (1999)
184. S.Sun. *Science*, **287**, 1989 (2000)
185. K.Elkins, D.Li, N.Poudyal, V.Nandwana, Z.Jin, K.Chen, J.P.Liu. *J. Phys. D: Appl. Phys.*, **38**, 2306 (2005)
186. C.B.Rong, D.Li, V.Nandwana, N.Poudyal, Y.Ding, Z.L.Wang, H.Zeng, J.P.Liu. *Adv. Mater.*, **18**, 2984 (2006)
187. Y.Ide, T.Goto, K.Kikuchi, K.Watanabe, J.Onagawa, H.Yoshida, J.M.Cadogan. *J. Magn. Magn. Mater.*, **177** – **181**, 1245 (1998)
188. T.Shima, K.Takanashi, Y.K.Takahashi, K.Hono. *Appl. Phys. Lett.*, **81**, 1050 (2002)
189. S.Okamoto, O.Kitakami, N.Kikuchi, T.Miyazaki, Y.Shimada, Y.K.Takahashi. *Phys. Rev. B*, **67**, 094422 (2003)
190. T.Shima, K.Takanashi, Y.K.Takahashi, K.Hono. *Appl. Phys. Lett.*, **85**, 2571 (2004)
191. K.Son, G.Ryu, H.Jeong, L.Fink, M.Merz, P.Nagel, S.Schuppler, G.Richter, E.Goering, G.Schütz. *Small*, **15**, 1902353 (2019)
192. F.Wang, X.Xu, Y.Liang, J.Zhang, H.Wu. *Appl. Phys. Lett.*, **95**, 022516 (2009)
193. X.Sun, Z.Y.Jia, Y.H.Huang, J.W.Harrell, D.E.Nikles, K.Sun, L.M.Wang. *J. Appl. Phys.*, **95**, 6747 (2004)
194. J.H.Kim, J.Kim, N.Oh, Y.-H.Kim, C.K.Kim, C.S.Yoon, S.Jin. *Appl. Phys. Lett.*, **90**, 023117 (2007)
195. S.H.Liou, S.Huang, E.Klimek, R.D.Kirby, Y.D.Yao. *J. Appl. Phys.*, **85**, 4334 (1999)
196. J.A.Christodoulides, Y.Huang, Y.Zhang, G.C.Hadjipanayis, I.Panagiotopoulos, D.Niarchos. *J. Appl. Phys.*, **87**, 6938 (2000)
197. R.K.Rakshit, S.K.Bose, R.Sharma, R.C.Budhani. *Appl. Phys. Lett.*, **89**, 202511 (2006)
198. H.Köno. *J. Phys. Soc. Jpn.*, **13**, 1444 (1958)
199. Q.Zeng, I.Baker, J.B.Cui, Z.C.Yan. *J. Magn. Magn. Mater.*, **308**, 214 (2007)

200. J.Z.Wei, Z.G. Song, Y.B.Yang, S.Q.Liu, H.L.Du, J.Z.Han, D.Zhou, C.S.Wang, Y.C.Yang, A.Franz, D.Többens, J.B.Yang. *AIP Adv.*, **4**, 127113 (2014)
201. K.Patel, J.Zhang, S.Ren. *Nanoscale*, **10**, 11701 (2018)
202. T.J.Nummy, S.P.Bennett, T.Cardinal, D.Heiman. *Appl. Phys. Lett.*, **99**, 252506 (2011)
203. C.L.Zha, R.K.Dumas, J.W.Lau, S.M.Mohseni, S.R.Sani, I.V.Golosovsky, Å.F.Monsen, J.Nogués, J.Åkerman. *J. Appl. Phys.*, **110**, 093902 (2011)
204. R.M.Gutiérrez-Pérez, J.T.Holguín-Momaca, J.T.Elizalde-Galindo, F.Espinosa-Magaña, S.F.Olive-Méndez. *J. Appl. Phys.*, **117**, 123902 (2015)
205. T.Saito, D.Nishio-Hamane. *AIP Adv.*, **6**, 075004 (2016)
206. R.W.McCallum, L.Lewis, R.Skomski, M.J.Kramer, I.E.Anderson. *Annu. Rev. Mater. Res.*, **44**, 451 (2014)
207. Y.B.Yang, X.G.Chen, S.Guo, A.R.Yan, Q.Z.Huang, M.M.Wu, D.F.Chen, Y.C.Yang, J.B.Yang. *J. Magn. Magn. Mater.*, **330**, 106 (2013)
208. T.Chen, W.Stutius. *IEEE Trans. Magn.*, **10**, 581 (1974)
209. X.Guo, X.Chen, Z.Altounian, J.O.Ström-Olsen. *Phys. Rev. B*, **46**, 14578 (1992)
210. J.B.Yang, Y.B.Yang, X.G.Chen, X.B.Ma, J.Z.Han, Y.C.Yang, S.Guo, A.R.Yan, Q.Z.Huang, M.M.Wu, D.F.Chen. *Appl. Phys. Lett.*, **99**, 082505 (2011)
211. N.V.Rama Rao, A.M.Gabay, G.C.Hadjipanayis. *J. Phys. D: Appl. Phys.*, **46**, 062001 (2013)
212. K.Kanari, C.Sarafidis, M.Gjoka, D.Niarchos, O.Kalogirou. *J. Magn. Magn. Mater.*, **426**, 691 (2017)
213. N.V.Rama Rao, A.M.Gabay, W.F.Li, G.C.Hadjipanayis. *J. Phys. D: Appl. Phys.*, **46**, 265001 (2013)
214. D.Zhou, Y.-F.Zhang, X.-B.Ma, S.-Q.Liu, J.-Z.Han, M.-G.Zhu, C.-S.Wang, J.-B.Yang. *Chin. Phys. Lett.*, **32**, 127502 (2015)
215. P.Kharel, V.R.Shah, X.Z.Li, W.Y.Zhang, R.Skomski, J.E.Shield, D.J.Sellmyer. *J. Phys. D: Appl. Phys.*, **46**, 095003 (2013)
216. S.V.Vonsovskii. *Fizicheskaya Entsiklopediya. (Physical Encyclopedia)*. (Moscow: Great Russian Encyclopedia, 1988)
217. C.Kitte. *Phys. Rev.*, **73**, 155 (1948)
218. W.Wu, V.Kiryukhin, H.J.Noh, K.T.Ko, J.H.Park, W.Ratcliff, P.A.Sharma, N.Harrison, Y.J.Choi, Y.Horibe, S.Lee, S.Park, H.T.Yi, C.L.Zhang, S.W.Cheong. *Phys. Rev. Lett.*, **101**, 137203 (2008)
219. Y.C.Tseng, N.M.Souza-Neto, D.Haskel, M.Gich, C.Frontera, A.Roig, M.Van Veenendaal, J.Nogués. *Phys. Rev. B: Condens. Matter Mater. Phys.*, **79**, 094404-1 (2009)
220. S.I.Ohkoshi, K.Imoto, A.Namai, S.Anan, M.Yoshikiyo, H.Tokoro. *J. Am. Chem. Soc.*, **139**, 13268 (2017)
221. E.Lima, E.L.Winkler, D.Tobia, H.E.Troiani, R.D.Zysler, E.Agostinelli, D.Fiorani. *Chem. Mater.*, **24**, 512 (2012)
222. H.Sh.Dehsari, K.Asadi. *J. Phys. Chem. C*, **122**, 29106 (2018)
223. E.A.Gorbachev, L.A.Trusov, A.E.Sleptsova, E.S.Kozlyakova, L.N.Alyabyeva, S.R.Yegiyan, A.S.Prokhorov, V.A.Lebedev, I.V.Roslyakov, A.V.Vasiliev, P.E.Kazin. *Mater. Today*, **32**, 13 (2020)
224. J.Iida, M.Tanaka. *J. Phys. Soc. Jpn.*, **62**, 1723 (1993)
225. K.-T.Ko, H.-J.Noh, J.-Y.Kim, B.-G.Park, J.-H.Park, A.Tanaka, S.B.Kim, C. L.Zhang, S.-W. Cheong. *Phys. Rev. Lett.*, **103**, 207202 (2009)
226. J.Iida, S.Takekawa, N.Kimizuka. *J. Cryst. Growth*, **102**, 398 (1990)
227. A.D.Christianson, M.D.Lumsden, M.Angst, Z.Yamani, W.Tian, R.Jin, E.A.Payzant, S.E.Nagler, B.C.Sales, D.Mandrus. *Phys. Rev. Lett.*, **100**, 107601 (2008)
228. M.H.Phan, N.A.Frey, M.Angst, J.de Groot, B.C.Sales, D.G.Mandrus, H.Srikanth. *Solid State Commun.*, **150**, 341 (2010)
229. Y.Qin, X.Q.Liu, Y.J.Wu, X.M.Chen. *J. Am. Ceram. Soc.*, **96**, 2506 (2013)
230. D.S.F.Viana, R.A.M.Gotardo, L.F.Ctica, I.A.Santos, M.Olzon-Dionysio, S.D.Souza, D.Garcia, J.A.Eiras, A.A.Coelho. *J. Appl. Phys.*, **110**, 034108 (2011)
231. C.M.Brooks, R.Misra, J.A.Mundy, L.A.Zhang, B.S.Holinsworth, K.R.O'Neal, T.Heeg, W.Zander, J.Schubert, J.L.Musfeldt, Z.-K.Liu, D.A.Muller, P.Schiffer, D.G.Schlom. *Appl. Phys. Lett.*, **101**, 132907 (2012)
232. X.L.Wen, Z.Chen, E.H.Liu, X.Lin. *Appl. Surf. Sci.*, **357**, 1212 (2015)
233. Y.J.Kim, S.Konishi, Y.Hayasaka, I.Kakeya, K.Tanaka. *CrystEngComm*, **22**, 1096 (2020)
234. C.Schmitz-Antoniak, D.Schmitz, P.Borisov, F.M.F.De Groot, S.Stienen, A.Warland, B.Krumme, R.Feyerherm, E.Dudzik, W.Kleemann, H.Wende. *Nat. Commun.*, **4**, 2051 (2013)
235. E.Fantechi, G.Campo, D.Carta, A.Corrias, C.De Julián Fernández, D.Gatteschi, C.Innocenti, F.Pineider, F.Rugi, C.Sangregorio. *J. Phys. Chem. C*, **116**, 8261 (2012)
236. G.Muscas, N.Yaacoub, G.Concas, F.Sayed, R.Sayed Hassan, J.M.Greneche, C.Cannas, A.Musinu, V.Foglietti, S.Casciardi, C.Sangregorio, D.Peddis. *Nanoscale*, **7**, 13576 (2015)
237. M.V.Limaye, S.B.Singh, S.K.Date, D.Kothari, V.R.Reddy, A.Gupta, V.Sathe, R.J.Choudhary, S.K.Kulkarni. *J. Phys. Chem. B*, **113**, 9070 (2009)
238. S.E.Shirsath, X.Liu, Y.Yasukawa, S.Li, A.Morisako. *Sci. Rep.*, **6**, 30074 (2016)
239. D.N.Dipesh, L.Wang, H.Adhikari, J.Alam, S.R.Mishra. *J. Alloys Compd.*, **688**, 413 (2016)
240. D.Li, H.Yun, B.T.Diroll, V.V.T.Doan-Nguyen, J.M.Kikkawa, C.B.Murray. *Chem. Mater.*, **28**, 480 (2016)
241. A.López-Ortega, E.Lottini, C.D.J.Fernández, C.Sangregorio. *Chem. Mater.*, **27**, 4048 (2015)
242. S.T.Xu, Y.Q.Ma, G.H.Zheng, Z.X.Dai. *Nanoscale*, **7**, 6520 (2015)
243. R.S.Turtelli, M.Kriegisch, M.Atif, R.Grössinger. *IOP Conf. Ser. Mater. Sci. Eng.*, **60**, 012020 (2014)
244. A.Hutlova, D.Niznansky, J.L.Rehspringer, C.Estournès, M.Kurmoo. *Adv. Mater.*, **15**, 1622 (2003)
245. G.Pourroy, S.Läkamp, M.Multigner, A.Hernando, J.-L.Dormann, R.Valenzuela-Monjaras. *J. Phys. IV*, **7**, C1-238 (1997)
246. B.H.Liu, J.Ding, Z.L.Dong, C.B.Boothroyd, J.H.Yin, J.B.Yi. *Phys. Rev. B: Condens. Matter Mater. Phys.*, **74**, 184427 (2006)
247. Y.Cedeño-Mattei, O.Perales-Perez, M.S.Tomar, F.Roman, P.M.Voyles, W.G.Stratton. *J. Appl. Phys.*, **103**, 07E512 (2008)
248. C.N.Chinnasamy, B.Jeyadevan, K.Shinoda, K.Tohji, D.J.Djayaprawira, M.Takahashi, R.J.Joseyphus, A.Narayanasamy. *Appl. Phys. Lett.*, **83**, 2862 (2003)
249. A.E.Berkowitz, W.J.Schuele. *J. Appl. Phys.*, **30**, S134 (1959)

250. K.M.Krishnan, A.B.Pakhomov, Y.Bao, P.Blomqvist, Y.Chun, M.Gonzales, K.Griffin, X.Ji, B.K.Roberts. *J. Mater. Sci.*, **41**, 793 (2006)
251. Q.Song, Z.J.Zhang. *J. Am. Chem. Soc.*, **126**, 6164 (2004)
252. N.Bao, L.Shen, W.An, P.Padhan, C.H.Turner, A.Gupta. *Chem. Mater.*, **21**, 3458 (2009)
253. M.Tachiki. *Prog. Theor. Phys.*, **23**, 1055 (1960)
254. J.C.Slonczewski. *Phys. Rev.*, **110**, 1341 (1958)
255. G.Salazar-Alvarez, J.Qin, V.Šepelák, I.Bergmann, M.Vasilakaki, K.N.Trohidou, J.D.Ardisson, W.A.A.Macedo, M.Mikhaylova, M.Muhammed, M.D.Baró, J.Nogués. *J. Am. Chem. Soc.*, **130**, 13234 (2008)
256. D.Peddis, C.Cannas, A.Musinu, A.Ardu, F.Orrui, D.Fiorani, S.Laureti, D.Rinaldi, G.Muscas, G.Concas, G.Piccaluga. *Chem. Mater.*, **25**, 2005 (2013)
257. P.Tancredi, P.C.Rivas-Rojas, O.Moscoso-Londoño, D.Muraca, M.Knobel, L.M.Socolovsky. *Appl. Phys. Lett.*, **115**, 263104 (2019)
258. L.Kumar, M.Kar. *J. Magn. Magn. Mater.*, **323**, 2042 (2011)
259. M.B.Mohamed, M.Yehia. *J. Alloys Compd.*, **615**, 181 (2014)
260. M.Sumalatha, S.Sh.K.Reddy, M.S.Reddy, S.Sripada, M.M.Raja, C.G.Reddy, P.Y.Reddy, V.R.Reddy. *J. Alloys Compd.*, **837**, 155478 (2020)
261. R.Pandit, K.K.Sharma, P.Kaur, V.R.Reddy, R.Kumar, J.Shah. *J. Alloys Compd.*, **596**, 39 (2014)
262. R.Nongjai, S.Khan, K.Asokan, H.Ahmed, I.Khan. *J. Appl. Phys.*, **112**, 084321 (2012)
263. K.Krieble, M.Devlin, S.J.Lee, S.T.Aldini, J.E.Snyder. *J. Appl. Phys.*, **103**, 07E508 (2008)
264. F.Sharifianjazi, M.Moradi, N.Parvin, A.Nemati, A.Jafari Rad, N.Sheysi, A.Abouchenari, A.Mohammadi, S.Karbasi, Z.Ahmadi, A.Esmaeilkhanian, M.Irani, A.Pakseresht, S.Sahmani, M.Shahedi Asl. *Ceram. Int.*, **46**, 18391 (2020)
265. T.Hyeon, S.S.Lee, J.Park, Y.Chung, H.B.Na. *J. Am. Chem. Soc.*, **123**, 12798 (2001)
266. S.H.Moon, S.H.Noh, J.H.Lee, T.H.Shin, Y.Lim, J.Cheon. *Nano Lett.*, **17**, 800 (2017)
267. J.H.Lee, J.T.Jang, J.S.Choi, S.H.Moon, S.H.Noh, J.W.Kim, J.G.Kim, I.S.Kim, K.I.Park, J. Cheon. *Nat. Nanotechnol.*, **6**, 418 (2011)
268. S.Sun, H.Zeng. *J. Am. Chem. Soc.*, **124**, 8204 (2002)
269. J.Tuček, R.Zbořil, A.Namai, S.I.Ohkoshi. *Chem. Mater.*, **22**, 6483 (2010)
270. M.Kurmoo, J.L.Rehspringer, A.Hutlova, C.D'Orléans, S.Vilminot, C.Estournès, D.Niznansky. *Chem. Mater.*, **17**, 1106 (2005)
271. S.I.Ohkoshi, H.Tokoro. *Bull. Chem. Soc. Jpn.*, **86**, 897 (2013)
272. M.Gich, C.Frontera, A.Roig, E.Taboada, E.Molins, H.R.Rechenberg, J.D.Ardisson, W.A.A.Macedo, C.Ritter, V.Hardy, J.Sort, V.Skumryev, J.Nogués. *Chem. Mater.*, **18**, 3889 (2006)
273. C.Rath, K.K.Sahu, S.D.Kulkarni, S.Anand, S.K.Date, R.P.Das, N.C.Mishra. *Appl. Phys. Lett.*, **75**, 4171 (1999)
274. L.Lu, L.Li, X.Wang, G.Li. *J. Phys. Chem. B*, **109**, 17151 (2005)
275. R.Yao, C.Cao. *RSC Adv.*, **2**, 1979 (2012)
276. J.Jin, S.I.Ohkoshi, K.Hashimoto. *Adv. Mater.*, **16**, 48 (2004)
277. L.A.Trusov, E.A.Gorbachev, V.A.Lebedev, A.E.Sleptsova, I.V.Roslyakov, E.S.Kozlyakova, A.V.Vasiliev, R.E.Dinnebier, M.Jansen, P.E.Kazin. *Chem. Commun.*, **54**, 479 (2018)
278. S.Sakurai, J.Jin, K.Hashimoto, S.I.Ohkoshi. *J. Phys. Soc. Jpn.*, **74**, 1946 (2005)
279. J.L.García-Muñoz, A.Romaguera, F.Fauth, J.Nogués, M.Gich. *Chem. Mater.*, **29**, 9705 (2017)
280. M.Popovici, M.Gich, D.Nižanský, A.Roig, C.Savii, L.Casas, E.Molins, K.Zaveta, C.Enache, J.Sort, S.De Brion, G.Chouteau, J.Nogués. *Chem. Mater.*, **16**, 5542 (2004)
281. J.Ma, Y.Wang, K.Chen. *Adv. Powder Technol.*, **30**, 3021 (2019)
282. D.Kubániová, P.Brázda, K.Závěta, T.Kmječ, M.Klementová, J.Kohout. *J. Magn. Magn. Mater.*, **472**, 96 (2019)
283. M.Nakaya, R.Nishida, N.Hosoda, A.Muramatsu. *Cryst. Res. Technol.*, **52** (11), 2 (2017)
284. A.Namai, S.Ohkoshi. *Chem. – Eur. J.*, **24**, 11880 (2018)
285. A.Namai, M.Yoshikiyo, S.Umeda, T.Yoshida, T.Miyazaki, M.Nakajima, K.Yamaguchi, T.Suemoto, S.I.Ohkoshi. *J. Mater. Chem. C*, **1**, 5200 (2013)
286. S.I.Ohkoshi, A.Namai, K.Imoto, M.Yoshikiyo, W.Tarora, K.Nakagawa, M.Komine, Y.Miyamoto, T.Nasu, S.Oka, H.Tokoro. *Sci. Rep.*, **5**, 14414 (2015)
287. S.Sakurai, K.Tomita, K.Hashimoto, H.Yashiro, S.I.Ohkoshi. *J. Phys. Chem. C*, **112**, 20212 (2008)
288. A.Namai, M.Yoshikiyo, K.Yamada, S.Sakurai, T.Goto, T.Yoshida, T.Miyazaki, M.Nakajima, T.Suemoto, H.Tokoro, S.I.Ohkoshi. *Nat. Commun.*, **3**, 1035 (2012)
289. M.Gich, J.Gazquez, A.Roig, A.Crespi, J.Fontcuberta, J.C.Idrobo, S.J.Pennycook, M.Varela, V.Skumryev. *Appl. Phys. Lett.*, **96**, 8 (2010)
290. L.Corbellini, C.Lacroix, C.Harnagea, A.Korinek, G.A.Botton, D.Ménard, A.Pignolet. *Sci. Rep.*, **7**, 3712 (2017)
291. M.Gich, I.Fina, A.Morelli, F.Sánchez, M.Alexe, J.Gàzquez, J.Fontcuberta, A.Roig. *Adv. Mater.*, **26**, 4645 (2014)
292. T.Katayama, S.Yasui, Y.Hamasaki, T.Osakabe, M.Itoh. *J. Mater. Chem. C*, **5**, 12597 (2017)
293. Y.Ding, J.R.Morber, R.L.Snyder, Z.L.Wang. *Adv. Funct. Mater.*, **17**, 1172 (2007)
294. Y.Kusano, T.Fujii, J.Takada, M.Fukuhara, K.Yamaguchi, K.Takabatake, A.Doi, Y.Iked, M.Takano, Y.Kusano, T.Fujii, J.Takada, M.Fukuhara, A.Doi, Y.Ikeda, M.Takano. *Chem. Mater.*, **20**, 151 (2008)
295. J.Ma, K.Chen. *Ceram. Int.*, **44**, 19338 (2018)
296. A.Sivkov, E.Naiden, A.Ivashutenko, I.Shanenkov. *J. Magn. Magn. Mater.*, **405**, 158 (2016)
297. B.David, N.Pizúrová, P.Synek, V.Kudrle, O.Jašek, O.Schneeweiss. *Mater. Lett.*, **116**, 370 (2014)
298. S.Ohkoshi, S.Sakurai, J.Jin, K.Hashimoto. *J. Appl. Phys.*, **97**, 10K312 (2005)
299. G.F.Dionne. *Magnetic Oxides*. (New York: Springer, 2009)
300. K.Matsuno, T.Goto, T.Ide, M.Yoshikiyo, O.Inoue, K.Tamazaki, M.Goto, T.Yoshida, A.Namai, K.Masada, T.Miyazaki, K.Imoto, S.Ohkoshi. *Angew. Chem., Int. Ed.*, **55**, 11403 (2016)
301. S.I.Ohkoshi, S.Kuroki, S.Sakurai, K.Matsumoto, K.Sato, S.Sasaki. *Angew. Chem., Int. Ed.*, **46**, 8392 (2007)
302. S.Sakurai, S.Kuroki, H.Tokoro, K.Hashimoto, S.Ohkoshi. *Adv. Funct. Mater.*, **17**, 2278 (2007)

303. Y.Zhao, G.Wen. *J. Magn. Magn. Mater.*, **512**, 167039 (2020)
304. I.Ahamed, R.Pathak, R.Skomski, A.Kashyap. *AIP Adv.*, **8**, 055815 (2018)
305. M.Yoshikiyo, A.Namai, K.Imoto, H.Tokoro, S.Ohkoshi. *Eur. J. Inorg. Chem.*, 847 (2018)
306. S.I.Ohkoshi, A.Namai, T.Yamaoka, M.Yoshikiyo, K.Imoto, T.Nasu, S.Anan, Y.Umeta, K.Nakagawa, H.Tokoro. *Sci. Rep.*, **6**, 27212 (2016)
307. R.D.Shannon. *Acta Crystallogr., Sect. A*, **32**, 751 (1976)
308. G.Albanese, A.Deriu. *Ceramurg. Int.*, **5**, 3 (1979)
309. A.Isalgué, X.Obradors, J.Tejada. *J. Phys. Colloq.*, **46**, 345 (1985)
310. Y.Xu, G.L.Yang, D.P.Chu, H.R.Zhai. *Phys. Status Solidi*, **157**, 685 (1990)
311. N.Fuchikami. *J. Phys. Soc. Jpn.*, **20**, 760 (1965)
312. B.T.Shirk, W.R.Buessem. *J. Appl. Phys.*, **40**, 1294 (1969)
313. T.Koutzarova, S.Kolev, C.Ghelev, K.Grigorov, I.Nedkov. *Adv. Nanoscale Magn.*, 183 (2009)
314. H.Luo, B.K.Rai, S.R.Mishra, V.V.Nguyen, J.P.Liu. *J. Magn. Magn. Mater.*, **324**, 2602 (2012)
315. D.D.Zaitsev, S.E.Kushnir, P.E.Kazin, Y.D.Tretyakov, M.Jansen. *J. Magn. Magn. Mater.*, **301**, 489 (2006)
316. S.W.Lee, S.Y.An, S.J.Kim, I.-B.Shim, C.S.Kim. *IEEE Trans. Magn.*, **39**, 2899 (2003)
317. S.Y.An, S.W.Lee, S.W.Lee, C.S.Kim. *J. Magn. Magn. Mater.*, **242 – 245**, 413 (2002)
318. F.K.Lotgering. *J. Phys. Chem. Solids*, **35**, 1633 (1974)
319. K.Iida, Y.Minachi, K.Masuzawa, M.Kawakami, H.Nishio, H.Taguchi. *J. Magn. Soc. Jpn.*, **23**, 1093 (1999)
320. F.Kools, A.Morel, R.Grössinger, J.Le Breton, P.Tenaud. *J. Magn. Magn. Mater.*, **242 – 245**, 1270 (2002)
321. H.Ueda, Y.Tanioku, C.Michioka, K.Yoshimura. *Phys. Rev. B*, **95**, 224421 (2017)
322. D.Seifert, J.Töpfer, F.Langenhorst, J.-M.Le Breton, H.Chiron, L.Lechevallier. *J. Magn. Magn. Mater.*, **321**, 4045 (2009)
323. D.H.Choi, S.W.Lee, I.-B.Shim, C.S.Kim. *J. Magn. Magn. Mater.*, **304**, e243 (2006)
324. H.R.Zhai, J.Z.Liu, M.Lu. *J. Appl. Phys.*, **52**, 2323 (1981)
325. F.Sandiumenge, S.Gali, J.Rodriguez. *Mater. Res. Bull.*, **23**, 685 (1988)
326. X.Obradors, A.Isalgue, A.Collomb, M.Pernet, J.Pannetier, J.Roctriguez, J.Tejada, J.C.Joubert. *IEEE Trans. Magn.*, **20**, 1636 (1984)
327. D.J.De Bitetto. *J. Appl. Phys.*, **35**, 3482 (1964)
328. S.Wang, J.Ding, Y.Shi, Y.Chen. *J. Magn. Magn. Mater.*, **219**, 206 (2000)
329. D.D.Zaitsev, P.E.Kazin, L.A.Trusov, D.A.Vishnyakov, Y.D.Tretyakov, M.Jansen. *J. Magn. Magn. Mater.*, **300**, e473 (2006)
330. P.E.Kazin, L.A.Trusov, D.D.Zaitsev, Y.D.Tretyakov, M.Jansen. *J. Magn. Magn. Mater.*, **320**, 1068 (2008)
331. P.E.Kazin, L.A.Trusov, D.D.Zaitsev, Y.D.Tret'yakov. *Russ. J. Inorg. Chem.*, **54**, 2081 (2009)
332. E.Kazin, A.Trusov, S.E.Kushnir, N.V.Yaroshinskaya, N.A.Petrov, M.Jansen. *J. Phys. Conf. Ser.*, **200**, 072048 (2010)
333. E.A.Gorbachev, L.A.Trusov, A.E.Sleptsova, E.O.Anokhin, D.D.Zaitsev, A.V.Vasiliev, A.A.Eliseev, P.E.Kazin. *Mendeleev Commun.*, **28**, 401 (2018)
334. H.Sato. *Mater. Trans. JIM*, **38**, 858 (1997)
335. H.Sato. *Mater. Trans. JIM*, **37**, 1672 (1996)
336. B.T.Shirr, W.R.Buessrm. *J. Am. Ceram. Soc.*, **53**, 192 (1970)
337. D.D.Zaitsev, P.E.Kazin, E.A.Gravchikova, L.A.Trusov, S.E.Kushnir, Y.D.Tretyakov, M.Jansen. *Mendeleev Commun.*, **14**, 171 (2004)
338. H.Z.Wang, B.Yao, Y.Xu, Q.He, G.H.Wen, S.W.Long, J.Fan, G.D.Li, L.Shan, B.Liu, L.N.Jiang, L.L.Gao. *J. Alloys Compd.*, **537**, 43 (2012)
339. H.Z.Wang, Y.N.Hai, B.Yao, Y.Xu, L.Shan, L.Xu, J.L.Tang, Q.H.Wang. *J. Magn. Magn. Mater.*, **422**, 204 (2017)
340. A.Yamamoto, D.Hashizume, H.A.Katori, T.Sasaki, E.Ohmichi, T.Nishizaki, N.Kobayashi, H.Takagi. *Chem. Mater.*, **22**, 5712 (2010)
341. C.-R.Lin, Y.-J.Siao, S.-Z.Lu, C.Gau. *IEEE Trans. Magn.*, **45**, 4275 (2009)
342. H.Zhang, G.Long, D.Li, R.Sabirianov, H.Zeng. *Chem. Mater.*, **23**, 3769 (2011)
343. S.Li, D.Li, W.Liu, Z.Zhang. *Nanoscale*, **7**, 5395 (2015)
344. M.Sen Bishwas, R.Das, P.Poddar. *J. Phys. Chem. C*, **118**, 4016 (2014)
345. H.L.Feng, M.Reehuis, P.Adler, Z.Hu, M.Nicklas, A.Hoser, S.-C.Weng, C.Felser, M.Jansen. *Phys. Rev. B*, **97**, 184407 (2018)
346. H.L.Feng, Z.Deng, M.Wu, M.Croft, S.H.Lapidus, S.Liu, T.A.Tyson, B.D.Ravel, N.F.Quackenbush, C.E.Frank, C.Jin, M.-R.Li, D.Walker, M.Greenblatt. *Inorg. Chem.*, **58**, 397 (2019)
347. R.J.Holmberg, L.T.A.Ho, L.Ungur, I.Korobkov, L.F.Chibotaru, M.Murugesu. *Dalton Trans.*, **44**, 20321 (2015)
348. T.T.da Cunha, V.M.M.Barbosa, W.X.C.Oliveira, C.B.Pinheiro, E.F.Pedroso, W.C.Nunes, C.L.M.Pereira. *Polyhedron*, **169**, 102 (2019)
349. U.Albold, H.Bamberger, P.P.Hallmen, J.van Slageren, B.Sarkar. *Angew. Chem., Int. Ed.*, **58**, 9802 (2019)
350. J.M.Zadrozny, J.R.Long. *J. Am. Chem. Soc.*, **133**, 20732 (2011)
351. F.S.Guo, B.M.Day, Y.C.Chen, M.L.Tong, A.Mansikkamäki, R.A.Layfield. *Science*, **362**, 1400 (2018)
352. A.Jesche, R.W.McCallum, S.Thimmaiah, J.L.Jacobs, V.Taufour, A.Kreyssig, R.S.Houk, S.L.Bud'ko, P.C.Canfield. *Nat. Commun.*, **5**, 3333 (2014)
353. C.A.P.Goodwin, F.Ortu, D.Reta, N.F.Chilton, D.P.Mills. *Nature (London)*, **548**, 439 (2017)
354. F.S.Guo, B.M.Day, Y.C.Chen, M.L.Tong, A.Mansikkamäki, R.A.Layfield. *Angew. Chem., Int. Ed.*, **56**, 11445 (2017)
355. J.Liu, Y.C.Chen, J.L.Liu, V.Vieru, L.Ungur, J.H.Jia, L.F.Chibotaru, Y.Lan, W.Wernsdorfer, S.Gao, X.M.Chen, M.L.Tong. *J. Am. Chem. Soc.*, **138**, 5441 (2016)
356. Y.S.Ding, N.F.Chilton, R.E.P.Winpenny, Y.Z.Zheng. *Angew. Chem., Int. Ed.*, **55**, 16071 (2016)
357. Y.S.Ding, K.X.Yu, D.Reta, F.Ortu, R.E.P.Winpenny, Y.Z.Zheng, N.F.Chilton. *Nat. Commun.*, **9**, 3134 (2018)
358. K.R.McClain, C.A.Gould, K.Chakarawet, S.J.Teat, T.J.Groshens, J.R.Long, B.G.Harvey. *Chem. Sci.*, **9**, 8492 (2018)
359. J.P.Durrant, J.Tang, A.Mansikkamäki, R.A.Layfield. *Chem. Commun.*, **56**, 4708 (2020)
360. S.Demir, I.R.Jeon, J.R.Long, T.D.Harris. *Coord. Chem. Rev.*, **289 – 290**, 149 (2015)
361. J.M.Zadrozny, D.J.Xiao, M.Atanasov, G.J.Long, F.Grandjean, F.Neese, J.R.Long. *Nat. Chem.*, **5**, 577 (2013)

362. P.C.Bunting, M.Atanasov, E.Damgaard-Møller, M.Perfetti, I.Crassee, M.Orlita, J.Overgaard, J.Van Slageren, F.Neese, J.R.Long. *Science*, **362**, 1 (2018)
363. L.Spree, A.A.Popov. *Dalton Trans.*, **48**, 2861 (2019)
364. G.Velkos, W.Yang, Y.R.Yao, S.M.Sudarkova, X.Liu, B.Büchner, S.M.Avdoshenko, N.Chen, A.A.Popov. *Chem. Sci.*, **11**, 4766 (2020)
365. R.Westerström, J.Dreiser, C.Piamonteze, M.Muntwiler, S.Weyeneth, K.Krämer, S.X.Liu, S.Decurtins, A.Popov, S.Yang, L.Dunsch, T.Greber. *Phys. Rev. B: Condens. Matter Mater. Phys.*, **89**, 3 (2014)
366. F.Liu, D.S.Krylov, L.Spree, S.M.Avdoshenko, N.A.Samoylova, M.Rosenkranz, A.Kostanyan, T.Greber, A.U.B.Wolter, B.Büchner, A.A.Popov. *Nat. Commun.*, **8**, 16098 (2017)
367. M.A.Zykin, P.E.Kazin, M.Jansen. *Chem. – Eur. J.*, **26**, 8834 (2020)
368. P.E.Kazin, M.A.Zykin, L.A.Trusov, A.A.Eliseev, O.V.Magdysyuk, R.E.Dinnebier, R.K.Kremer, C.Felser, M.Jansen. *Chem. Commun.*, **53**, 5416 (2017)
369. P.E.Kazin, M.A.Zykin, V.V.Utochnikova, O.V.Magdysyuk, A.V.Vasiliev, Y.V.Zubavichus, W.Schnelle, C.Felser, M.Jansen. *Angew. Chem., Int. Ed.*, **56**, 13416 (2017)
370. T.J.Ballé, Z.Zangeneh, L.Hozoi, A.Jesche, P.Höhn. *Phys. Rev. B*, **99**, 1 (2019)
371. I.G.Rau, S.Baumann, S.Rusponi, F.Donati, S.Stepanow, L.Gragnaniello, J.Dreiser, C.Piamonteze, F.Nolting, S.Gangopadhyay, O.R.Albertini, R.M.Macfarlane, C.P.Lutz, B.A.Jones, P.Gambardella, A.J.Heinrich, H.Brune. *Science*, **344**, 988 (2014)
372. F.Donati, S.Rusponi, S.Stepanow, C.Wäckerlin, A.Singha, L.Persichetti, R.Baltic, K.Diller, F.Patthey, E.Fernandes, J.Dreiser, Šljivančanin, K.Kummer, C.Nistor, P.Gambardella, H.Brune. *Science*, **352**, 318 (2016)
373. F.D.Natterer, K.Yang, W.Paul, P.Willke, T.Choi, T.Greber, A.J.Heinrich, C.P.Lutz. *Nature (London)*, **543**, 226 (2017)
374. L.-R.Guo, S.-S.Bao, B.Liu, D.Zeng, J.Zhao, J.Du, L.-M.Zheng. *Chem. – Eur. J.*, **18**, 9534 (2012)
375. A.E.Thorarinsdottir, T.D.Harris. *Chem. Rev.*, **120**, 8616 (2020); https://doi.org/10.1021/acs.chemrev.9b00666
376. D.K.Rittenberg, K.I.Sugiura, Y.Sakata, S.Mikami, A.J.Epstein, J.S.Miller. *Adv. Mater.*, **12**, 126 (2000)
377. Y.Numata, K.Inoue, N.Baranov, M.Kurmoo, K.Kikuchi. *J. Am. Chem. Soc.*, **129**, 9902 (2007)
378. N.Ishii, Y.Okamura, S.Chiba, T.Nogami, T.Ishida. *J. Am. Chem. Soc.*, **130**, 24 (2008)
379. R.A.A.Cassaro, S.G.Reis, T.S.Araujo, P.M.Lahti, M.A.Novak, M.G.F.Vaz. *Inorg. Chem.*, **54**, 9381 (2015)
380. Y.Okamura, T.Nogami, T.Ishida. *Chem. Lett.*, **38**, 740 (2009)
381. M.G.F.Vaz, R.A.A.Cassaro, H.Akpinar, J.A.Schlueter, P.M.Lahti, M.A.Novak. *Chem. – Eur. J.*, **20**, 5460 (2014)
382. Y.Okamura, N.Ishii, T.Nogami, T.Ishida. *Bull. Chem. Soc. Jpn.*, **83**, 716 (2010)
383. X.Liu, X.Feng, K.R.Meihaus, X.Meng, Y.Zhang, L.Li, J.Liu, K.S.Pedersen, L.Keller, W.Shi, Y.Zhang, P.Cheng, J.R.Long. *Angew. Chem., Int. Ed.*, **59**, 10610 (2020)
384. S.Vilminot, P.J.Baker, S.J.Blundell, T.Sugano, G.André, M.Kurmoo. *Chem. Mater.*, **22**, 4090 (2010)
385. M.Kurmoo. *Philos. Trans. R. Soc. Ser. A*, **357**, 3041 (1999)
386. M.Kurmoo, H.Kumagai, M.A.Green, B.W.Lovett, S.J.Blundell, A.Ardavan, J.Singleton. *J. Solid State Chem.*, **159**, 343 (2001)
387. Z.-L.Huang, M.Drillon, N.Masciocchi, A.Sironi, J.-T.Zhao, P.Rabu, P.Panissod. *Chem. Mater.*, **12**, 2805 (2000)
388. R.Feyerherm, A.Loose, P.Rabu, M.Drillon. *Solid State Sci.*, **5**, 321 (2003)
389. M.Kurmoo, H.Kumagai, S.M.Hughes, C.J.Kepert. *Inorg. Chem.*, **42**, 6709 (2003)